©2014

Yun Jiang

ALL RIGHTS RESERVED

MOLECULAR DYNAMIC SIMULATIONS OF LA_2O_3 AND LU_2O_3 DOPED SILICATE INTERGRANULAR FILMS IN β-SI_3N_4

by

YUN JIANG

A Dissertation submitted to the

Graduate School-New Brunswick

Rutgers, The State University of New Jersey

in partial fulfillment of the requirements

for the degree of

Doctor of Philosophy

Graduate Program in Materials Science & Engineering

written under the direction of

Stephen H. Garofalini

and approved by

_____

_____

_____

_____

New Brunswick, New Jersey

January, 2014

ABSTRACT OF THE DISSERTATION

Molecular Dynamic Simulations of La_2O_3 and Lu_2O_3 Doped

Silicate Intergranular Films in β-Si_3N_4

By YUN JIANG

Dissertation Director:

Stephen H. Garofalini

Thin, amorphous intergranular films (IGFs) ubiquitously exist at grain boundaries of polycrystalline ceramics. They play an important role in determining the macroscopic properties of high temperature structural ceramics. Silicon nitride ceramics (Si_3N_4) are high temperature structural ceramics due to their outstanding physical and mechanical properties at elevated temperature. The formation of the anisotropic grains of silicon nitride is very sensitive to the dopant cations used as sintering additives. HAADF-STEM images have shown that rare earth (RE) ions take very ordered locations, dependant upon the RE species, along the IGF/Prism interface in Si_3N_4 ceramics. However, such segregation does not explain the differences in morphology resulting from incorporation of the different RE additives. Atomistic details not readily available in experiments need to be collected.

Molecular dynamics computer simulations are used to evaluate the structure, energy and fracture behavior of silicon oxynitride intergranular films (IGFs) containing rare-earth ions (La or Lu) between silicon nitride crystals as a function of IGF thickness,

composition, and crystal orientations (prism, basal, and high index). La adsorption on the prism surface is observed at locations consistent with HAADF-STEM results. La segregation corresponding to N content is discussed. A variation in the local composition would cause some IGFs to show segregation of all La to the interface, leaving little La within the glassy IGF, while other IGFs may show more La remaining in the glassy IGF. Such differences affect strength. Lu does not adsorb onto a fully nitride prism surface. The presence of O at certain surface lattice sites plays a major role in the adsorption of Lu ions onto those sites consistent with HAADF-STEM results but has little effect on La siteing. .Energies of the La or Lu ions as a function of location are calculated to provide an explanation for the segregation behavior as well as consideration of their role in the glassy state of the IGF. Growth along the crystal surface is studied, providing an atomistic mechanism for the experimentally observed anisotropic grain growth of silicon nitride influenced by the different additives. Fracture strengths via stress-strain curves are calculated.

Acknowledgements

First and foremost, I would like to express my deepest gratitude to my advisor, Professor Stephen Garofalini for his greatest help and supervision during the past five years. Many thanks to the immense knowledge he taught me, the insightful ideas and invaluable research experiences he shared with me, the enlightening discussions we made so many times, the continuous funding throughout my graduate study, the opportunities to attend various conferences, to name a few. This thesis would not have been possible without Professor Garofalini's long lasting patience, encouragement, guidance and support.

I also would like to express special thanks to Professor Lisa Klein for offering me the opportunity as a teaching assistant and supporting me in overcoming the difficulties during my graduate life. I am grateful to the other members of my committee, Professor Philip Batson and Professor Frederic Cosandey, for their kindest help and insightful suggestions.

I am deeply indebted to Professor Richard Lehman for organizing the very many successful activities every year. I am grateful to Professor George Sigel for having nice conversations regarding research as well as life. I am deeply thankful to Professor James Harrington for having me the enjoyable teaching assistant experience in his Lab III. I also wish to thank Professor Sophocles J. Orfanidis for his kind understanding and help when working as a teaching assistant in his Matlab course. Besides that, I would like to express my sincere appreciation for having the opportunity to meet Dr. Stephen J. Pennycook and Dr. Juan Carlos Idrobo from the Oak Ridge National Laboratory.

A special thank you goes to John Yaniero for his many visits to facilitate the best help in all needs. A special thank you goes to Claudia Kuchinow for her enduring assistance to guide me through all the documentations every semester. A special thank you goes to Phyllis Cassell and Philip Grill for their generous help whenever needed.

I would like to express my appreciation to Glenn K. Lockwood for his very kind help to use all the facilities in the lab, his invaluable suggestions about doing research, and himself as a model of top graduate students. I also would like to thank Ying Ma for his excellent advice, collaboration, and the stimulating discussions. I especially want to thank Brian Viezbicke for introducing me to the lab, teaching me all the basics, and sharing his knowledge without reservation. I also would like to express my sincere thanks JiHee Kim for her generous help and suggestions, as well as the invaluable discussions we made in the very beginning of my PhD study. Many thanks should be delivered to Alexei Koltenikov and his students offering the strongest backup service and management for all the important computational resources to the entire group.

I wish to thank all of my colleagues who have made my life at Rutgers the most enjoyable journey: Julien Boisse, Steve Bottiglieri, Brenda V. Cortez, Giorgiana Giancola, Jesse Kohl, Qinghua Li, Paul Mark, Steve Mercurio, Weifeng Rao, Mahsa Sina, Doug Slusark, Lin Tang, Wojtek Tutak, Minh Vu, Vishnuvardhanan Vijayakumar, and Yiyun Yang. I wish to thank all my dear friends inside and outside Rutgers for bringing me so many fond memories during my graduate life.

Last but not least, I dedicate this thesis to my husband, Weizong Xu, and my parents for their constant understanding, support, encouragement and love. I love you all dearly.

Table of Contents

ABSTRACT OF THE DISSERTATION ii
Acknowledgements iv
List of Tables ix
List of Illustrations x
Chapter 1 Introduction 1
1.1 Intergranular Films 1
1.2 Silicon Nitride 2
1.3 Rare Earth Sintering Additives 4
1.4 The purpose of the study 8
Chapter 2 Molecular Dynamics Computer Simulation 10
2.1 Molecular Dynamic Computer Simulation 10
2.1.1 The Method 10
2.1.2 Predictor-corrector Algorithm 11
2.2 Study IGF by Molecular Dynamic Simulation 12
2.2.1 Design the Simulation System 12
2.2.2 Melt Quench Process 12
2.2.3 Potential Type and Parameters 13
2.2.4 Output Data 15
Chapter 3 The Locations of La Ions in Lanthanum Silicon Oxy-Nitride Intergranular Films in Silicon Nitride 18
3.1 Introduction 18
3.2 Computational Procedures 19
3.2.1 Interatomic Potentials 19
3.2.2 Simulation System 22
3.3 Results and Discussion 25
3.3.1 La Adsorption Sites and La Segregation 26
3.3.2 The Energy of La Ions 30
3.3.3 Pair Distribution Functions for La-N 33
3.4 Conclusions 36
Chapter 4 La_2O_3-doped Silicate Intergranular Films in Si_3N_4 37

4.1 Introduction 37
4.2 Computational Procedures 38
4.2.1 Ion-ion Interactions 38
4.2.2 Computational System 41
4.3 Results and Discussion 44
4.3.1 La Ordering and Adsorption Sites 44
4.3.2 Compositional Effect 45
4.3.3 Energy of La Ions 50
4.3.4 Pair Distribution Functions and Coordination Number 53
4.3.5 Basal Growth and Partial Basal Growth 55
4.4 Conclusions 57
Chapter 5 Effect of Thickness and Composition on the Structure and Ordering in La-doped Intergranular Films between Si_3N_4 Crystals 59
5.1 Introduction 59
5.2 Computational Procedures 61
5.2.1 Two-body and Three-body Potentials 61
5.2.2 System Design and IGF Compositions 63
5.2.3 Fracture the System 68
5.2.4 La Adsorption Sites 69
5.3 Results and Discussion 70
5.3.1 Thickness Effect 70
5.3.2 La Saturation Percentage 74
5.3.3 Energy of La Ions According To Z 76
5.3.4 Fracture Strength and Stress-Strain Curve 78
5.4 Conclusions 82
Chapter 6 Role of oxygen on the adsorption sites of Lu and La in β-Si_3N_4 84
6.1 Introduction 84
6.2 Computational Procedure 86
6.2.1 System Design with O termination 86
6.2.2 Potential Development 89
6.3 Results and Discussions 93

6.3.1 Density Profiles of Lu for Single Replacement 93
6.3.2 Density Profiles of Lu for Double Replacement 94
6.3.3 Energy Map and Adsorption Energies of Lu ion 95
6.3.4 Density Profiles of Lu in 6 Å IGF 98
6.3.5 Density Profiles of La 100
6.3.6 Density Profiles of Triple Replacement 103
6.4 Conclusions 106
Chapter 7 Different dopant effects of Lu and La in β-Si3N4 108
7.1 Introduction 108
7.2 Computational Procedures 109
7.2.1 Simulation System 109
7.2.2 Interatomic Potential 111
7.3 Results and Discussion 112
7.3.1 Role of Lu and La on grain growth 112
7.3.2 Lu being moved away from prism surface 114
7.3.3 Energy Evolvement of Lu ions 116
Chapter 8 Summary 119
References 122

List of Tables

Table 3.1 Modified BMH Pair Potential Parameters 20
Table 3.2 Lennard-Jones Pair Potential Parameters 21
Table 3.3 Three-Body Potential Parameters 22
Table 3.4 Melt-Quench Process 24
Table 4.1 Parameters for modified BMH and LJ pair potentials 39
Table 4.2 Parameters for three-body potential 40
Table 4.3 Melt-quench process 42
Table 4.4 Compositions of IGFs 43
Table 5.1 Modified BMH and LJ pair potentials parameters 62
Table 5.2 Three-body potential parameters 63
Table 5.3 Melt-quench process 66
Table 5.4 Compositions of ~1.8 nm thick IGFs 67
Table 5.5 Compositions of ~0.6 nm thick IGFs 68
Table 6.1 Melt-quench process 88
Table 6.2 Two-body pair potential parameter sets 90
Table 6.3 Three-body potential parameters 92
Table 6.4 Adsorption energies of Lu ion at Lu1 and Lu2 sites on differently terminated prism surfaces. (Site locations are approximate, but coincide with Figure 6.4.) 98
Table 7.1 Melt-quench process 110
Table 7.2 Two-body pair potential parameter sets 110
Table 7.3 Three-body potential parameters 112

List of Illustrations

Figure 1.1 High angle annular dark field images of La and Lu adsorption sites on the silicon nitride prism surface conducted by three research groups[40]. An undoped silicon nitride prism interface is also shown. 7

Figure 3.1 Schematic drawing of the system. Periodic boundaries are in x, y, and z, although the use of frozen atoms in the upper and lower z directions preclude interactions between atoms in z. 23

Figure 3.2 Side-view snapshots of final configuration after the melt-quench process for four compositions: (a) 0N3La, (b) 0N6La, (c) 30N3La, and (d) 30N6La in a system containing a 1.8~2 nm lanthanum silicon oxy-nitride IGF between a basal β-Si3N4 crystal on the top and a prism β-Si3N4 crystal at the bottom. All bonds are drawn within a 2.0Å cut-off distance. The large white spheres represent La ions. The smaller grey spheres represent Si ions that are in the prism oriented β-Si3N4 crystal. The smallest grey spheres represent N ions that are in the prism oriented β-Si3N4 crystal. 25

Figure 3.3 (a) Drawing of sites from Winkelman et al., (b) HAADF-STEM micrograph from Winkleman *et al*.[22], (c) Our MD simulation results of La locations at IGF/Prism interface where the Prism interface. Arrows show locations of La ions at site 1 and 2 from both experiment and our MD simulations. The small white spheres represent O ions from the IGF 27

Figure 3.4 The saturation percentages of ordered La ions on the IGF/Basal and IGF/Prism interface for various compositions. B/Bmax means the actual La density divide by the La saturated density on the IGF/Basal interface. P/Pmax represents means the actual La density divide by the La saturated density including position 1 and 2 on the IGF/Prism interface. 29

Figure 3.5 The energy of La ions at sites 1 and 2 for the prism and in the interior of the IGF for different compositions. 31

Figure 3.6 HAADF-STEM images for La ions at the nitride prism interface with the IGF showing slight differences in La locations both at the interface and within the IGF (at arrows) (modified from Dwyer et al.[40]). 32

Figure 3.7 Pair distribution functions of La versus N for La ions at site 1 in comparison with La ions at site 2 on the IGF/Prism interface for (a) 0N3La, (b) 0N6La, (c) 30N3La, and (d) 30N6La. 33
Figure 3.8 La-N PDFs of different compositions from various La locations (a) La at position 1, (b) La at position 2, (c) La in the interior IGF. 35
Figure 4.1 Drawing of the simulation system with IGF between basal and prism β-Si_3N_4 crystals. Here, a 3Å gap is left between the IGF and each crystal as a very initial starting configuration before the melt quench process. 42
Figure 4.2 Four specific locations of La ions on the IGF/Prism interface viewed along the [001] direction. (a) Drawing of La sites from Winkelman *et al.*[22]; (b) HAADF-STEM image from Winkelman *et al.*[22]; (c) our MD simulation results. Arrows are used to point out La sites 1, 2, 3, and 4 from experiments and simulations. In (c), big white spheres represent La ions; small white spheres represent O ions; the smallest grey spheres represent N ions; bigger grey spheres represent Si ions. 44
Figure 4.3 Snapshots of final configurations of our MD simulations taken from the y direction for the entire thick system (not a slice of the system), which contains a ~1.8 nm thick IGF in contact with a basal oriented silicon nitride crystal on the top and a prism oriented silicon nitride crystal at the bottom for samples (a) 30N3La, (b) 30N6La. Here, atom types same as listed in Figure 4.2. Bonds between ions are drawn for the entire system with a cutoff distance of 2 Å. 45
Figure 4.4 Snapshots of the final configurations of our MD simulations for samples with same La content, different N content: (a) 0N3La, (b) 15N3La, (c) 30N3La, (d) 50N3La, similar to Figure 4.3. 47
Figure 4.5 Normalized La saturation percentages of sites 1, 2, 3, 4 and basal for (a) 3% La, (b) 6% La, and (c) 9% La, data derived by using the average La density of two systems with different starting configurations divided by the maximum La density of that specific site. Error bars are drawn. Data of sites 3 and 4 for the 50%N/(N+O) cases are marked gradient gray because of the vague La ordering at sites 3 and 4. . 49
Figure 4.6 Energy of La ions at different locations, averaged by two systems with different starting configurations. Error bars are used. 52

Figure 4.7 Average La-N PDFs of systems from two different starting configurations for various N contents at (a) 3%La and (b) 6%La, where the central La ions are from site 1; (c) 3%La and (d) 6%La, where the central La ions are from site 2. 55

Figure 4.8 Snapshots of (a) basal growth (50N3La), and (b) partial basal growth (50N6La). Dashed lines are drawn to distinguish the original basal crystal and the new basal portion. Only bonds are drawn for better view. Bond features are similar to Figure 4.2, Figure 4.3 and Figure 4.4. A bright circle is drawn in (b) to point out the region where basal growth is disrupted..... 57

Figure 5.1 (a) Drawing of the simulation system with IGF between prism oriented and high index oriented β-Si_3N_4 crystals. Before the melt quench, a 3Å gap is left between the IGF and each crystal as a starting configuration. (b) Drawing of the high index oriented β-Si_3N_4 crystal surrounded by glassy nitride. (c) Diagram for site nomenclature of site 1, 2, 3, 4 after Winkelman et al.[22] and sites 5, 6 in this paper. 65

Figure 5.2 Snapshots of the final configuration of our MD simulations, which contains a 30N6La IGF (about 5.2 nm thick in y) in contact with a prism oriented silicon nitride crystal on the top and a basal oriented silicon nitride crystal at the bottom with different thickness (a) ~1.8 nm thick, (b) ~0.6 nm thick. For clean view, only Si (big grey spheres) and N ions (small grey spheres) from the prism and La ions (big white spheres) are shown in spheres here. Bonds are drawn with cutoff distance of 2 Å..... 70

Figure 5.3 Snapshots of the final configuration of our MD simulations, containing an IGF (about 5.2 nm thick in y) between a prism and a high index [31-41] oriented silicon nitride crystal for various thicknesses and compositions (a) ~1.8 nm 30N3La, (b) ~0.6 nm 30N3La, (c) ~1.8 nm 30N6La, (d) ~0.6 nm 30N6La. Here, the drawings of the atoms and bonds are same as listed in Figure 2. 72

Figure 5.4 Comparison of La saturation percentage at various locations (La at site 1, 2, 3, 4 on the prism interface or on the [31-41] high index surface) for (a) ~1.8 nm IGF and (b) ~0.6 nm IGF of various compositions. These charts are derived by using the La density at a specific site or surface for a specific composition to divide the maximum La density at that location among all the compositions..... 75

Figure 5.5 Chart of averaged number of La ions according to La locations in z (areas in black) and energy of La ions according to z (areas in grey) for (a) ~1.8 nm 15N6La, (b) ~0.6 nm 15N6La, (c) ~1.8 nm 30N6La, (d) ~0.6 nm 30N6La IGF. 77
Figure 5.6 Stress-strain curves for 3% La, 6% La and 9% La in (a) ~1.8 nm IGFs at 15% N/(N+O), (b) ~0.6 nm IGFs at 15% N/(N+O), (c) ~1.8 nm IGFs at 30% N/(N+O), (d) ~0.6 nm IGFs at 30% N/(N+O) between prism and [31-41] high index silicon nitride crystals. 78
Figure 5.7 Snapshots after fracture of (a) ~1.8 nm, (b) ~0.6 nm 30N6La IGF between prism and [31-41] high index silicon nitride crystals. 80
Figure 5.8 Density profiles of all species as a function of z, perpendicular to the IGF-crystal interfaces for (a) ~1.8 nm 15N6La, (b) ~0.6 nm 15N6La, (c) ~1.8 nm 30N6La, and (d) ~0.6 nm 30N6La. Only the regions near the IGF are shown. Si and N ions from the crystal are labeled Si-c and N-c, respectively; Si and N ions from the IGF are labeled Si-g and N-g, respectively. 81
Figure 6.1 (a) Top view and (b, c) side view of the Si_3N_4 prism surface (N in blue spheres, Si in larger yellow spheres). Nitrogen sites are respectively labeled as S3, S4, S5, S1, S2, S3 along the x axis. The red dots in (a) indicate possible Lu1 and Lu2 sites. In (b) are shown Lu adsorption sites Lu1, Lu2, Lu1′ and Lu2′ (c) La adsorption sites La1, La2, La3 and La4 on the Si_3N_4 prism surface..... 86
Figure 6.2 Density Profiles of Lu from a 18 Å IGF along the z axis on various prismatic surfaces with one site terminated by O, simulated by (a) Lu potential set A; (b) Lu potential set B; (c) Lu potential set C. S1 means all the S1 sites on the prismatic surface are terminated by O. N means all sites are terminated by N. Here, the empty triangle represents Lu1 site; dark triangle represents Lu2 site; gray diamond represents Lu1’ site; gray triangle represents Lu2’ site. Last Si layer in prism surface is at 20.6Å. 94
Figure 6.3 Density Profiles of Lu from a 18 Å IGF along the z axis on various prismatic surfaces with two sites terminated by O, simulated by (a) Lu potential set A; (b) Lu potential set B; (c) Lu potential set C. Markers same as in figure 2. 95
Figure 6.4 Energy map for Lu on the (a) pure N prism surface and (b) O at the S1 sites. Grey hemisphere at (5.5, 3) is one Lu at site Lu2 that is kept frozen, while a second

Lu samples the rest of the adjacent surface sites. Site Lu1 is at (3.5, 0) and a second Lu2 site at (5.5, -3). Color bar gives Lu energy in eV. See text for further details. . 96
Figure 6.5 Density Profiles of Lu from a 6Å IGF along the z axis on various prismatic surfaces with one site terminated by O, simulated by (a) Lu potential set A; (b) Lu potential set B; (c) Lu potential set C. 100
Figure 6.6 Density Profiles of La from an 18Å IGF along the z axis on various prismatic surfaces with one site terminated by O, simulated by (a) La potential set A; (b) La potential set B; (c) La potential set C. Open triangles are site La1, dark triangles are site La2. 101
Figure 6.7 Density Profiles of La from an 18Å IGF along the z axis on various prismatic surfaces with two sites terminated by O, simulated by (a) La potential set A; (b) La potential set B; (c) La potential set C. 103
Figure 6.8 Density Profiles of RE ions from an 18Å IGF on various triple replacement surfaces for (a) Lu potential set A, (b) La potential set C. 104
Figure 7.1 Growth behavior on the silicon nitride prism surface for Lu_2O_3-doped glassy phase with 90% N/(N+O) and 1% Lu at 7000K for a duration of 10 nm (a) start, (b) end. 113
Figure 7.2 Snapshot of the growth behavior on the silicon nitride prism surface for glassy phase doped by La_2O_3 with 90% N/(N+O) and 1% La at 7000K for a duration of 10 nm (a) start, (b) end. 114
Figure 7.3 Density profiles of species of Si, N, O, and Lu as a function of z location and time f(z,t) for sample of 90% N/(N+O) and 0.2% Lu at 7000K during a 10 ns duration period at (a) start, (b) end. Two dashed lines are marked at same locations for (a) and (b) near 30Å in z. 115
Figure 7.4 The evolution of Lu ions for 90% N/(N+O) and 0.2% Lu sample at (a) start, (b) 2 ns, (3) 5 ns, (4) 10 ns. Locations of the Lu ions are projected on the xoz plane. Energies of the Lu ions are marked by colors. 117
Figure 7.5 The evolution of Lu ions for 70% N/(N+O) and 0.2% Lu sample at (a) start, (b) 2 ns, (3) 5 ns, (4) 10 ns. Locations of the Lu ions are projected on the xoz plane. Energies of the Lu ions are marked by colors. 118

Chapter 1 Introduction

1.1 Intergranular Films

Intergranular glassy films (IGFs) are amorphous nanometer-scale thin films (equilibrium thickness of about 1~4 nm) forming from impurities or sintering additives at many grain boundaries in polycrystalline ceramics[1-5] such as Si_3N_4, SiC, Al_2O_3, $SrTiO_3$, ZnO, etc. The formation of the IGFs could be attributed to the synthetic routes of the ceramics, for instance, liquid phase sintering[6], solid-state sub-eutectic sintering, and crystallization of glass surrounding the ceramic crystal.

IGFs play a significant role in determining the properties of the bulk ceramic as a whole[7,8]. Although IGFs occupy a small volume percent of the bulk ceramic, their unique structure, composition and local chemistry[9-11] can largely influence the macroscopic physical and mechanical properties of the bulk material[5,12-25]. The composition, structure and behavior of the IGFs had been shown to influence densification, phase transformations, anisotropic grain growth[15,26-30], and mechanical properties (such as strength and fracture toughness[5,8,16,31-33]), creep resistance, oxidation resistance and electrical behavior.

The first equilibrium IGF was found and characterized at grain boundaries in polycrystalline Si_3N_4. Due to the thin and amorphous nature of the IGFs, previously there had been a hard time for experimentalists to obtain atomistic details of the IGFs by experiments. The advances of electron microscopies change the situation[34-40]. Various microscopy techniques have been applied to measure the thickness of IGFs[41], determine the composition of IGF, and study the structure of IGFs and the glass-crystal interface. High-resolution transmission electron microscopy (HRTEM) can not only be

applied to image the atomic structure of the grain boundaries by phase-reconstruction methods at sub-angstrom resolution[42], but also be used to measure the thickness of the IGFs at straight grain boundaries[41]. The breakthrough of high-angle annular dark-field scanning transmission electron microscopy (HAADF-STEM) enables direct imaging of the IGF/crystal interfaces at the atomic level, showing the ordering of rare-earth species at the interface[35,36]. Electron energy loss spectroscopy (EELS) and energy-dispersive X-ray spectroscopy (EDS) can provide details of chemical species (or elemental) profiles across the IGF[36]. Other techniques include Fresnel contrast imaging, diffuse dark field imaging, diffraction analysis, electron holography, etc.

However, detailed atomistic structure is not ready by experimental due to the difficulty to fully characterize the IGF sample or any part of it. This makes it quite necessary to include theoretical modes to understand the IGFs better. On one hand, the force balance theory[43,44], diffuse interface model, segregation and wetting approach have been proposed. On the other hand, phase-field model, classical density functional theory, molecular dynamics simulation, monte carlo simulation and first-principle calculations are also employed. These theories and computer simulations provide atomistic details (such as the energetics and the amorphous structure) and mechanisms still not readily available in experiment[43].

1.2 Silicon Nitride

Silicon and other nitrides largely exist in the rocks of the earth's crust. Formed from two of the most readily available elements in the earth's crust, silicon and nitrogen, silicon nitride is relatively inexpensive. Silicon nitride ceramics have been widely studied

for over 50 years. There exists two kinds of crystal structures, α-Si_3N_4 (space group $P3_1c$) and β-Si_3N_4 (space group $P6_3/m$).

Silicon nitride ceramics (Si_3N_4) are promising high temperature structural ceramics due to their outstanding physical and mechanical properties at high temperature. Silicon nitride ceramics not only has low density, friction, thermal expansion coefficient, but also has high hardness, strength, stiffness. They maintain good resistance to oxidation, corrosion, wear, thermal shock and refractoriness. Due to their high decomposition temperature, silicon nitrides maintain very good high temperature stability. However, their intrinsic brittleness is a bottle neck problem. Therefore, efforts are made to introduce whisker-like microstructures to ensure high fracture resistance.

Silicon nitride ceramics have a wide range of applications[45,46]. They are good high-temperature structural engine materials and can be used as turbines and engine parts in the automobile and aerospace industry (e.g. silicon nitride turbocharger rotors). Other than that, silicon nitride ceramics can also be used as high-temperature and unlubricated roller and ball bearings or abrasive application in oil drilling, vacuum pumps, dental drills. Additionally, silicon nitride based cutting tools are also widely used.

Many Si_3N_4 are fabricated through liquid phase sintering[47] or hot-pressing. Sintering additives (MgO, Y_2O_3, rare-earth oxides, CaO, F, Cl [10]) can be added to obtain a fully dense form. The major factor controlling strength can be attributed to the intergranular glass formed from the densification additives. The anisotropic grain morphology is sensitive to the sintering additives[48] (e.g. rare earth and Group III elements) during the liquid phase sintering process; however, its mechanism is still not fully understood.

β-Si_3N_4 can be regarded as a whisker-reinforced structural ceramic, due to its rodlike grains acting as self-reinforcements to toughen the material[49]. These reinforcing microstructures could promote toughness mechanisms[32,50-55], e.g. crack bridging, pull out and crack deflection. However, efforts still need to be made to improve its strength and toughness. Rare earth (RE) elements[56,57] including La, Sm, Gd, Er, Yb, Lu, are found to be able to greatly influence Si_3N_4 α→β phase transformation. RE are doped in silicon nitride ceramics to help improve their creep resistance[58,59], toughness[32,55,60,61] and grains growth behavior[31,48,62]. Adding RE ions into the IGF has been shown to be able to modify the mechanical properties and growth morphology[22,24,59,63-69].

1.3 Rare Earth Sintering Additives

Lanthanide oxide sintering additives have shown a great influence on the grain aspect ratio and grain-size distribution, suggesting an influence on the silicon nitride interfacial energies. The formation of the anisotropic grains of silicon nitride is very sensitive to the dopant cations used as sintering additives[22,48,70]. Dopant atoms can control the anisotropic grain growth, thus forming the whisker-like grain morphology. Therefore, it is important to understand the mechanism of the dopant effects[13,71,72], in order to design high performance silicon nitride ceramics through microstructure optimization[35,73].

It had been found that RE elements preferentially segregate to specific locations at the β-Si_3N_4 prism oriented surface, although different RE elements segregate into different locations along this interface, leading to different interface morphology. Ab-initio calculations provide additional information regarding the interface sites to which

the RE ion adsorbs. The combination of the microscopy data, the ab-initio calculations[74], and the effect of RE additives on mechanical properties imply an important role for the location of the RE ions on properties. This makes it very important to understand both the RE adsorption on the Si_3N_4 prism interface and RE distribution within the glassy portion of the IGFs.

There remain a lot of open questions regarding the topic of RE doped IGFs in β-Si_3N_4, both interesting and significant. Different fracture behavior of IGF, intergranular fracture (La) vs transgranular fracture (Lu), becomes the most interesting research topic. This leads to the study of interfacial ordering induced by β-Si_3N_4 grains. Although ordering of dopants on the crystal surface has been observed by different groups, details regarding how to quantify those sites filling or how the dopants are distributed within the IGF are still lacking. Segregation behavior of La and Lu across the IGF dependent upon composition becomes very important. The energetic and the mechanism of such segregation are interesting. The question of how to describe the role of La and Lu in strengthening or weakening the IGF is still unknown. The dependence of the oxidation behavior and the orientation of silicon nitride ceramics, the IGF thickness could also be relevant. The competition between RE and Si for migrating to the β-Si_3N_4 surface and their bonding characteristics, according to the model of differential binding energy, is needed.

Three research groups from Oxford, Oak Ridge National Laboratory (ORNL) and Lawrence Berkeley National Laboratory (LBNL) conducted high angle annular dark field imaging on rare earth oxides densified silicon nitride ceramics from the same batch of sample[75]. Interfacial ordering and element dependent sites have been observed on the

prism surface of β-Si_3N_4 crystals. The Oxford group observed La ordering as site 1, 2, 3, and 4 on the prism surface; the ORNL group slightly different La sites at the interface; while the LBNL group shows no La ordering on the surface (Figure 1.1). Similar adsorption sites of Lu on the prism surface are observed among three research groups, while with different site saturation (viewed from the image intensity) as shown in Figure 1.1. Semi-crystallization on the prism surface are found in RE doped silicon nitride[39]. The anisotropic grain growth is reported to be related to the strong preferential segregation of RE species to the prismatic planes, retarding the grain growth effectively on the prism planes. The role of La or Lu in changing the fracture behavior (intergranular vs. transgranular) is found to be important.

The presence of oxygen are found to be important in controlling the RE adsorption and site selection on the silicon nitride prism interface[36]. Oxygen-induced change in grain-boundary chemistry and structural transformation has an influence on fracture behavior (intergranular vs. transgranular) and crack propagation[76]. First principle calculation has also been used to study the reconstructions and nonstoichiometry of oxygenated β-Si_3N_4 surfaces[77].

A model called differential binding energy (a first-principle model) has been developed to show the competition between the rare earth ion and the silicon ion to segregate to the prism surface[22]. This theory shows that La has more segregation preference to the crystal surface than Lu. First-principle cluster and surface slab models were used to calculate the energies of rare earth adsorption sites on the prism surface[78,79]. Ching et al.[80] were able to conduct theoretical tensile experiments using *ab initio* methods based on density functional theory (DFT) for the 907-atom

system containing a silicon-oxynitride IGF (about 1.7 nm thick) in two β-Si_3N_4 prism planes. The stress-strain behavior of IGF between prismatic planes is found to be different from that between basal planes.

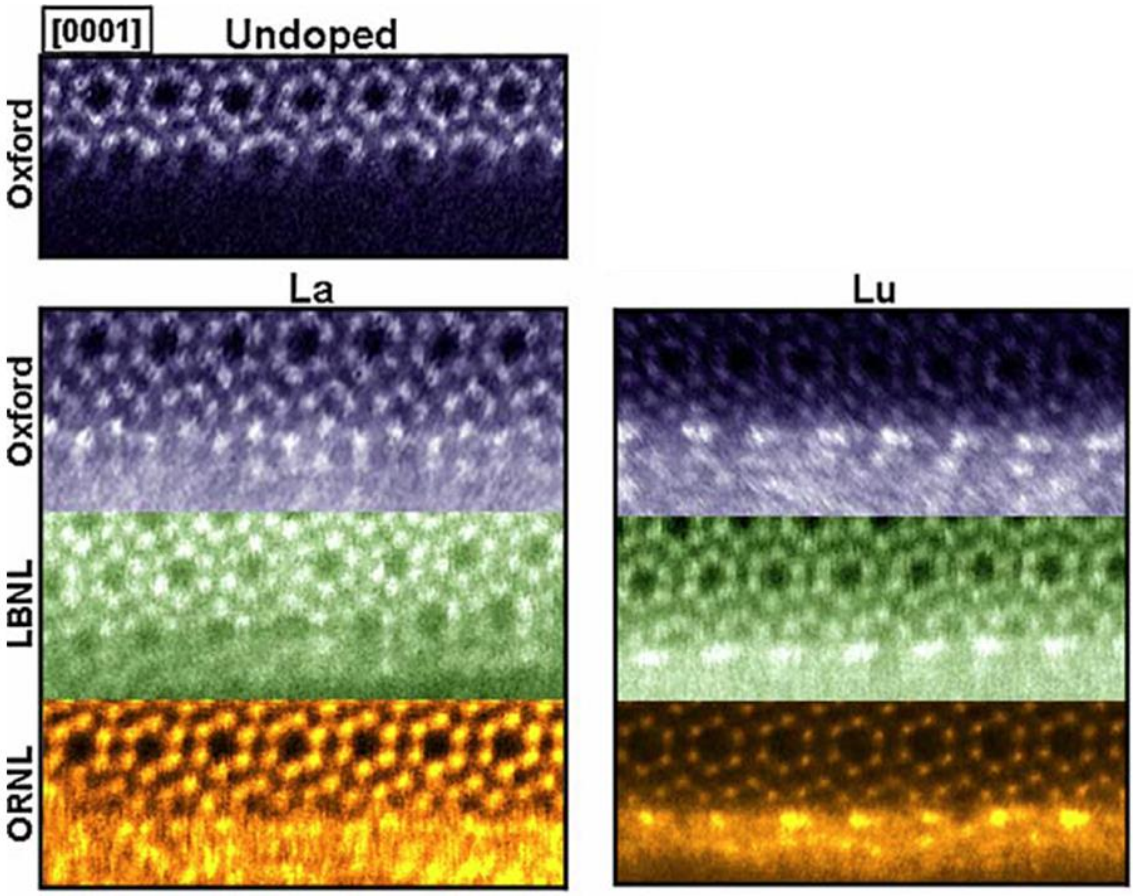

Figure 1.1 High angle annular dark field images of La and Lu adsorption sites on the silicon nitride prism surface conducted by three research groups[75]. An undoped silicon nitride prism interface is also shown.

1.4 The purpose of the study

Previous molecular dynamics (MD) simulations in our group had predicted the presence of density oscillations and ordering in the IGF at the IGF/crystal interface, induced by the crystal structure, extending into the IGF nearly 1nm, with adsorption of modifier cations in the silicate IGFs to specific surface sites. Network modifiers (Na or Ca) had been predicted to preferentially segregate into ordering sites at the IGF/crystal interfaces in alumina and silicon nitride systems, implying similar segregation behavior using RE ions due to their similar role as modifiers in the silicate glass[81].

STEM images[35,36], ab-initio calculations and MD simulations have shown that rare earth ions take very ordered locations, dependant upon the RE species, along the IGF/Prism interface in Si_3N_4 ceramics. However, there still remain interesting questions and unknowns with regard to this topic. The reason for the difference among the experimental STEM images obtained by three research groups for La and Lu interfacial adsorption is unknown and needs to be studied. The atomic columns obtained by experiments are not quantified. The microstructure or the La and Lu distribution in the interior IGF is unknown. The fact that controls the segregation behavior of La or Lu in the IGF needs to be studied. The role of lighter atoms (e.g. N or O) needs to be explored. The mechanism of rare earth dopants on the Si_3N_4 grain morphology is still not fully understood. The mechanism of the effect of La or Lu on intergranular or transgranular fracture is still not clear. Other important features affecting IGF properties are still needed.

This research proposal is designed to study the system of La or Lu oxides doped IGFs in β-Si_3N_4 by means of Molecular Dynamic computer simulations. This proposal

aims to obtain atomistic details not readily available in experiments (e.g. the energetics and site filling properties of the RE ions), develop understanding of the microstructure-property relationships, and gain further insights into the mechanisms controlling the RE segregation behavior and fracture behavior of the IGFs. Handful experimental studies are available for comparison. Important parameters as regard to the study of IGFs, such as thickness, structure, temperature, pressure, chemistry, orientation of the bounding grains, would also be included. All of the above could help to design the microstructure of β-Si_3N_4 ceramics for the next generation.

In this work, we focus on the IGFs in silicon nitride sintered with La and Lu additives in a system of the prism oriented Si_3N_4 surface and a basal or high index Si_3N_4 surface, separated by IGFs with different thickness and compositions.

Chapter 2 Molecular Dynamics Computer Simulation

2.1 Molecular Dynamic Computer Simulation

2.1.1 The Method

Molecular dynamics (MD) is a computer simulation method that calculates the time dependent physical movements of atoms according to Newton's equations[82-87]. The atom mass is m. The atom position is r. The atom velocity is dr/dt. The acceleration is

$$a = \frac{dv}{dt} = \frac{d}{dt}\left(\frac{dr}{dt}\right) = \frac{dr^2}{dt^2} \qquad (2.1)$$

The interatomic potential energy is U. The force is –dU/dr. The Newton's equation of motion is

$$F = -\frac{dU}{dr} = m\left(\frac{dr^2}{dt^2}\right) \qquad (2.2)$$

The total potential energy of the system is

$$E_p = \frac{1}{2}\sum U_{ij} \qquad (2.3)$$

The internal energy is

$$U = \frac{3}{2}NkT + \sum U_{ij} \qquad (2.4)$$

Pressure is

$$p = \frac{NkT}{V} + \frac{1}{3V}\left\langle \sum r_i F_i \right\rangle \qquad (2.5)$$

Average temperature is

$$\frac{3}{2}NkT = \sum \frac{m_i v_i^2}{2}$$
$$T = \frac{\left\langle \sum m_i v_i^2 \right\rangle}{3Nk} \qquad (2.6)$$

Constant volume heat capacity

$$C_v = \frac{3}{2}Nk + \frac{\left\langle U^2 \right\rangle - \left\langle U \right\rangle^2}{kT^2} \qquad (2.7)$$

2.1.2 Predictor-corrector Algorithm

Here, we use the fifth-order Nordsieck predictor-corrector algorithm. The predictor part is calculated as follows.

$$\begin{aligned} r &= r + v + a + r^4 + r^5 + r^6 \\ v &= v + 2a + 3r^4 + 4r^5 + 5r^6 \\ a &= a + 3r^4 + 6r^5 + 10r^6 \\ r^4 &= r^4 + 4r^5 + 10r^6 \end{aligned} \qquad (2.8)$$

The corrector part is calculated as follows.

$$\begin{aligned} \Delta a &= \frac{f}{m} - a \\ r &= r + c_1 \Delta a \\ v &= v + c_2 \Delta a \\ a &= a + c_3 \Delta a \\ r^4 &= r^4 + c_4 \Delta a \\ r^5 &= r^5 + c_5 \Delta a \\ r^6 &= r^6 + c_6 \Delta a \\ r^5 &= r^5 + 5r^6 \end{aligned} \qquad (2.9)$$

where c1=3/16, c2=251/360, c3=1. C4=11/18, c5=1/6, c6=1/60.

2.2 Study IGF by Molecular Dynamic Simulation

2.2.1 Design the Simulation System

Molecular dynamics computational simulations are employed to study the sandwich system, specifically, an amorphous intergranular film containing La_2O_3 or Lu_2O_3 between two β-Si_3N_4 crystals of different orientations. The system size is usually about 53Å×53Å in x and y dimension. Along the z axis, the system could be set as prism, 3Å gap, random glassy atoms, 3Å gap, basal or high index crystal, and a 10Å vacuum on the top. For the high index crystal, a glassy silicon nitride shell is added to the high index oriented β-Si_3N_4 crystal for simplicity to apply periodic boundary conditions in x and y.

Various IGF compositions (3%, 6%, 9% La or Lu, 0%, 15%, 30%, 50% N/(N+O)) are studied, to investigate the atomistic structure of lanthanide silicon oxynitride IGFs and the segregation behavior of the dopants as a function of composition. Thick (about 1.8 nm) and thin (about 0.6 nm) IGFs are also included to explore the effect of thickness on fracture strength. Around 4800 and 1600 randomized atoms will be used to form the thick (1.8 nm) and thin (0.6 nm) IGFs. Periodic boundary is applied in the x and y direction. The time step is 1fs.

2.2.2 Melt Quench Process

The glassy IGF will be made using a melt-quench process to form the grain boundary phase. Generally, IGF ions will be randomly distributed in between two silicon nitride crystals. IGF ions will first be melted to high temperatures such as 10000K, and then quenched down through several intermediate temperatures until room temperature such as 9000K, 8000K, 7000K, 6000K, 5000K, 4000K, 3000K, 2000K, 1000K, 300K.

Pressure in z direction will be added at high temperatures to help form a proper IGF thickness. Pressure in x, y and z will be added at low temperatures to allow the IGF to adjust according to the crystal relaxation.

2.2.3 Potential Type and Parameters

The interatomic pair potentials regarding La and Lu are established, specifically for La-O, La-N, La-La, and Lu-O, Lu-N, Lu-Lu pairs. After initially setting up the La-O, La-N and La-La pair potentials according to the bond length and bond energy from literature (with theoretical and experimental values), these curvature of the pair potential need to be tuned based on the La_2O_3 crystal (trigonal P-3m1) and LaN crystal (Fm-3m) under constant pressure or constant volume at 300K. Just for the purpose of investigating the competence of cations or anions, adjustments of the bond strength (weaker or stronger) may need to be made later on when studying the segregation behavior of the dopants. The Lu-O, Lu-N and Lu-Lu pair potentials will be set up and tuned in the same fashion based on the Lu_2O_3 crystal and LuN crystal.

Multi-body interactions are chosen to describe interactions between ions, similar to previous studies in our group. The interatomic potentials used in this research contain a 2-body and a 3-body part.

$$V = \sum_{i \neq j} V_{ij}^{2-body} + \sum_{i \neq j \neq k} V_{jik}^{3-body} \qquad (2.10)$$

For the 2-body part, the modified Born-Mayer-Huggins (BMH) pair potential will be employed for most ion-ion interactions. The Lennard-Jones (LJ) pair potential might also be added to the 2-body part of RE-O or RE-N interaction for the purpose of flexible comfortable potential curvatures at a certain bond length and strength.

$$V_{ij}^{2-body} = \begin{cases} \sum_{i \neq j} V_{ij}^{BMH} + \sum_{i \neq j} V_{ij}^{LJ} \\ \sum_{i \neq j} V_{ij}^{BMH} \end{cases} \qquad (2.11)$$

The modified Born-Mayer-Huggins (BMH) pair potential is given by

$$V_{ij}^{BMH} = A_{ij} \exp\left(\frac{-r_{ij}}{\rho_{ij}}\right) + \frac{z_i z_j e^2}{r_{ij}} erfc\left(\frac{r_{ij}}{\beta_{ij}}\right) \qquad (2.12)$$

where most parameters are readily in previously published papers.

The Lennard-Jones (LJ) pair potential is given by

$$V_{ij}^{LJ} = 4\varepsilon\left[\left(\frac{\sigma}{r_{ij}}\right)^{12} - \left(\frac{\sigma}{r_{ij}}\right)^{6}\right] \quad \text{or} \quad V_{ij}^{LJ} = \frac{27}{4}\varepsilon\left[\left(\frac{\sigma}{r_{ij}}\right)^{9} - \left(\frac{\sigma}{r_{ij}}\right)^{6}\right] \qquad (2.13)$$

and is added to the BMH form for the ease of tuning the parameters for certain interactions.

The 3-body potential[88] is given by

$$V_{jik}^{3-body} = \lambda_{jik} \exp\left(\frac{\gamma_{ij}}{r_{ij} - r_{ij}^0} + \frac{\gamma_{ik}}{r_{ik} - r_{ik}^0}\right) \Omega_{jik} \qquad (2.14)$$

if $r_{ij} < r_{ij}^0$ and $r_{ik} < r_{ik}^0$; $V_{jik}^{3-body} = 0$ otherwise. The angular term between ions j, i, and k is given as

$$\Omega_{jik} = \left(\cos\theta_{jik} - \cos\theta_{jik}^0\right)^2 \qquad (2.15)$$

r_{ij} is the separation distance between atoms *i* and *j*, *e* the elementary charge, z_i and z_j are the full ionic charges, and *erfc* is the complementary error function. The values of the parameters A_{ij}, β_{ij} and ρ_{ij} for each pair type have been previously presented[89]. The ionic charges for silicon, oxygen, lanthanum, and nitrogen ions are +4, -2, +3, and -3, respectively.

The error function is defined as

$$erf(x) = \frac{2}{\sqrt{\pi}} \int_0^x e^{-t^2} dt \qquad (2.16)$$

The complementary error function is defined as

$$erfc(x) = 1 - erf(x) = \frac{2}{\sqrt{\pi}} \int_x^\infty e^{-t^2} dt \qquad (2.17)$$

where

$$t = \frac{x}{\sqrt{2}\sigma} \qquad (2.18)$$

The numerical approximation of the complementary error function is given as

$$erfc(x) \approx \left(a_1 t + a_2 t^2 + a_3 t^3 + a_4 t^4 + a_5 t^5\right) e^{-x^2} \qquad (2.19)$$

where

$$t = \frac{1}{1 + px} \qquad (2.20)$$

and p=0.3275911, a1=0.254829592, a2=-0.284496736, a3=1.421413741, a4=-1.453152027, a5=1.061405429.

2.2.4 Output Data

The location of RE ions cross the IGF could be reviewed using VMD. Visual Molecular Dynamics (VMD) is an open source molecular visualization software program, which could display, animate and analyze three dimensional computational systems into graphics and movies. Images of the final configuration of the computational system will be produced with atoms and bonds marked by different colors.

Pair distribution function (PDF) and radial distribution function (RDF) of the cation-anion interactions could be calculated to obtain bonding characteristics at different

portion of the IGF. The first and the second peaks of the cation-anion bond can tell the atomistic structure in comparison with experimental data. Features such as short-range ordering or long-range ordering could also be obtained from PDF or RDF. Besides that, the coordination number of the anion around the cation is also needed for details regarding the number of neighbors around a central atom, indicating an influence of the energetic.

The simulation system will be pulled apart in z to conduct a fracture test. Stress-strain curve will be plotted. Fracture strength can be found from the stress-strain curve. The location where fracture occurs could be obtained. Details about fracture mechanism will be discussed based on composition and thickness.

The compositional effect of RE segregation in the IGF, and its consequential influence on the strength and fracture behavior are important and need to be discussed. Different thickness of the IGF could also result in different fracture strength. The effect of the opposing crystal orientation might also have an effect. To investigate the effect of the above controlling factors, the location and energies of RE ions in the IGF between the β-Si_3N_4 crystals will be determined and analyzed based on various compositions and thickness.

The location of RE ions on the prism surface could be compared to the experimental HAADF-STEM images directly. The number of RE adsorbed at a particular site and the number of sites available on the surface can be quantified. RE segregation to the various surface adsorption sites available (as site saturation rate) could be calculated as a normalized RE saturation percentage at each site. Histograms of RE segregation behavior across the IGF will be plotted. Preferential segregation to different crystal

surface needs to be compared and discussed. Energies of RE ions across the IGF could be calculated for the driving force for RE segregation. Energetic could also indicate the location where fracture would occur. Besides that, due to the importance of the compositional effect, density profiles of different species across the IGF could be calculated, providing very useful structural information of the composition effect.

It is important to study the growth behavior of β-Si_3N_4 crystals along the prism, basal or high index surface. The role of La or Lu, prohibiting or helping the crystal growth, will be discussed. The mechanism of the anisotropic grain growth behavior will be explored.

Chapter 3 The Locations of La Ions in Lanthanum Silicon Oxy-Nitride Intergranular Films in Silicon Nitride

3.1 Introduction

Intergranular films (IGFs) are glassy amorphous nanoscale thin films forming from impurities or sintering additives in polycrystalline ceramics. It has been found that the IGF, with its structure and concentration often dramatically different from those in bulk[12-14], occupy only a small volume percentage of the bulk, but can greatly influence the macroscopic mechanical, thermal, chemical, optical and electrical properties of the bulk ceramics[5,14-16,19-25,48].

Silicon nitride ceramics (Si_3N_4) have a wide range of applications as structural and electronic ceramics because of their outstanding mechanical properties at high temperature. However, efforts still need to be made to improve its strength and toughness. Rare earth (RE) elements including La, Sm, Gd, Er, Yb, Lu, are found to be able to greatly influence Si_3N_4 $\alpha \rightarrow \beta$ phase transformation[65,66]. RE are doped in silicon nitride ceramics to help improve their creep resistance, toughness and grains growth behavior[24,59,63]. Adding RE ions into the IGF has been shown to be able to modify the mechanical properties and growth morphology[22,24]. Recent high-angle annular dark field scanning transmission electron microscopy (HAADF-STEM) has provided atomistic detail of the interface between the IGF and the crystal. Results show that RE elements preferentially segregate to specific locations at the Si_3N_4 prism oriented surface, although different RE elements segregate into different locations along this interface, leading to different interface morphology[35-37,75]. Ab-initio calculations provide additional information regarding the interface sites to which the RE ion adsorbs [78,90].

The combination of the microscopy data, the ab-initio calculations, and the effect of RE additives on mechanical properties imply an important role for the location of the RE ions on properties. This makes it very important to understand both the RE adsorption on the Si_3N_4 prism interface and RE distribution within the glassy portion of the IGFs. Previous molecular dynamics (MD) simulations showed preferential segregation of network modifying species (alkali and alkaline earths) in silicate IGFs to the interface of specific crystallographic orientations of alumina and silicon nitride systems[81,91,92], implying segregation behavior that would be consistent with the studies using RE ions. However, RE ions had not been studied in these MD simulations and is the thrust of work presented here that could be directly compared to the HAADF-STEM results.

3.2 Computational Procedures

3.2.1 Interatomic Potentials

Molecular dynamics simulations are employed. We use interatomic potentials with multi-body interactions to describe interactions between ions. This contains a 2-body and a 3-body part.

$$V = \sum_{i \neq j} V_{ij}^{2-body} + \sum_{i \neq j \neq k} V_{jik}^{3-body} \qquad (3.1)$$

For La-N interaction, we use a combination of modified Born-Mayer-Huggins (BMH) pair potential and Lennard-Jones (LJ) pair potential for the 2-body part. While for all the other ion-ion interactions, we only employ the modified Born-Mayer-Huggins (BMH) pair potential as the 2-body part.

$$V_{ij}^{2-body} = \begin{cases} \sum_{i \neq j} V_{ij}^{BMH} + \sum_{i \neq j} V_{ij}^{LJ} & \text{for La-N bond} \\ \sum_{i \neq j} V_{ij}^{BMH} & \text{for non La-N bond} \end{cases} \qquad (3.2)$$

The modified Born-Mayer-Huggins (BMH) pair potential is given by

$$V_{ij}^{BMH} = A_{ij}\exp\left(\frac{-r_{ij}}{\rho_{ij}}\right) + \frac{z_i z_j e^2}{r_{ij}} erfc\left(\frac{r_{ij}}{\beta_{ij}}\right) \qquad (3.3)$$

where the parameters are given in Table 3.1 and have been previously discussed.

The Lennard-Jones (LJ) pair potential is given by

$$V_{ij}^{LJ} = 4\varepsilon\left[\left(\frac{\sigma}{r_{ij}}\right)^{12} - \left(\frac{\sigma}{r_{ij}}\right)^{6}\right] \qquad (3.4)$$

and is added to the BMH form for the La-N interactions.

Table 3.1 Modified BMH Pair Potential Parameters

Atom pair	A_{ij} (fJ)	β_{ij} (pm)	ρ_{ij} (pm)
O-O	0.0725	234	29
N-N	0.07241	220	29
Si-Si	0.1877	230	29
La-La	0.3975	230	45.1
N-O	0.1350	221	29
Si-La	0.3000	230	32
Si-O	0.2962	234	29
Si-N	0.7500	220	26.1
La-O	0.7377	270	31.75
La-N	3.9700	200	33.2

Table 3.2 Lennard-Jones Pair Potential Parameters

Atom pair	ε (fJ)	σ (pm)
La-N	0.00395	195.6

The 3-body potential is given by

$$V_{jik}^{3-body} = \lambda_{jik} \exp\left(\frac{\gamma_{ij}}{r_{ij} - r_{ij}^{0}} + \frac{\gamma_{ik}}{r_{ik} - r_{ik}^{0}} \right) \Omega_{jik} \qquad (3.5)$$

if $r_{ij} < r_{ij}^{0}$ and $r_{ik} < r_{ik}^{0}$; $V_{jik}^{3-body} = 0$ otherwise. The angular term between ions j, i, and k is given as

$$\Omega_{jik} = \left(\cos\theta_{jik} - \cos\theta_{jik}^{0} \right)^{2} \qquad (3.6)$$

r_{ij} is the separation distance between atoms *i* and *j*, *e* the elementary charge, z_i and z_j are the full ionic charges, and *erfc* is the complementary error function. The values of the parameters A_{ij}, β_{ij} and ρ_{ij} for each pair type have been previously presented[89]. The ionic charges for silicon, oxygen, lanthanum, and nitrogen ions are +4, -2, +3, and -3, respectively.

The La-O, La-N, La-La potentials are developed according to a 54.57Å×59.07Å×55.22Å La_2O_3 crystal (trigonal P-3m1). The xl, yl, zl value change about 2%, 2%, and 6% for the constant pressure tests.

Table 3.3 Three-Body Potential Parameters

Atom triplet	λ_{ij} (fJ)	γ_{ij} (pm)	r^0_{ij} (pm)	θ^0_{jik} (deg)
Si-O-Si	0.001	200	260	109.5
Si-N-Si	0.035	260	280	120
O/N-Si-O/N	0.024	280	300	109.5

3.2.2 Simulation System

Our simulated system is composed of two perfect β-Si3N4 crystals and an IGF in between. Along the z axis, our computational system is set as prism (7056 atoms, 53.25Å×52.40Å×26.35Å), 3Å gap, random glass atoms(30Å thickness), 3Å gap, and basal (7056 atoms, 53.25Å×52.70Å×26.20Å), as shown in Figure 3.1. We adjust the crystal sizes in x and y slightly so that they would be periodic and have the system of 53.25Å×52.70Å×88.55Å size.

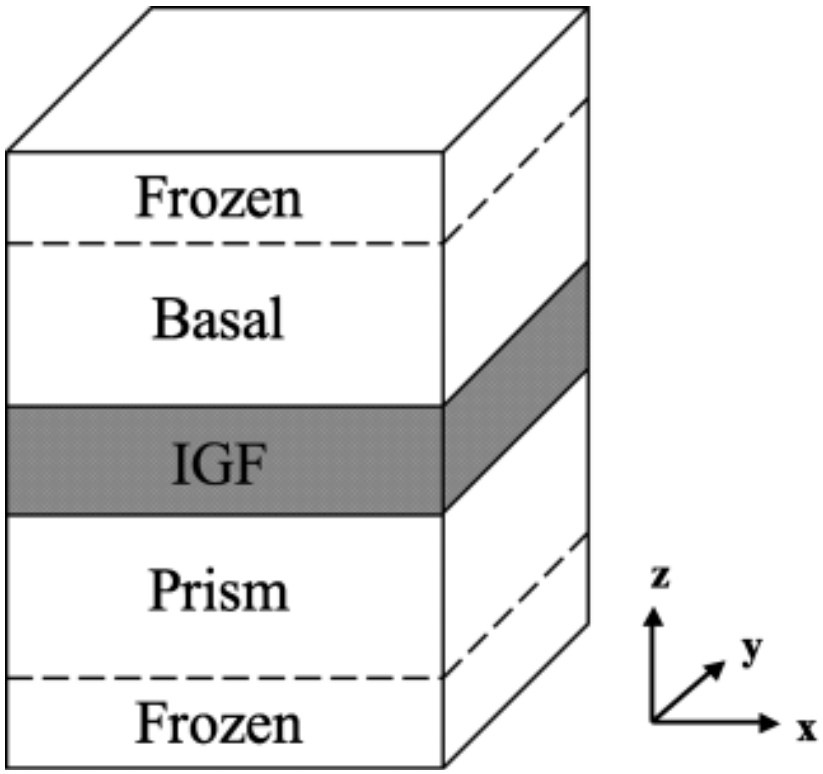

Figure 3.1 Schematic drawing of the system. Periodic boundaries are in x, y, and z, although the use of frozen atoms in the upper and lower z directions preclude interactions between atoms in z.

The glassy IGF is made using a melt-quench process in a manner similar to our previous work [89], although the time at temperature is longer here and is given in Table 3.4. Periodic boundary is applied in the x and y direction. In the z direction, reflecting boundary is applied on the third Si layer of the IGF/Prism interface and on the IGF/Basal interface from the beginning to 4000K of the melt-quench. We also design a small velocity modification here in order to prevent excessively hot atoms created in the initialization of the random glassy atoms from dominating the velocity rescaling during cooling. The time step we use is 10^{-15}s.

Table 3.4 Melt-Quench Process

Melt/Quench Temperature	Conditions	Duration
300K	NVE, crystal frozen	10 ps
10,000K	NVE, crystal frozen	20 ps
9000K	x,y constant, P_z = 3 GPa, crystal frozen	100 ps
8000K	As above	100 ps
7000K	As above	100 ps
6000K	As above	100 ps
5000K	As above	100 ps
4000K	As above	100 ps
3000K	x,y constant, P_z = 3 GPa, crystal de-frozen	100 ps
2000K	NpT, p = 0.1 MPa	20 ps
1000K	As above	20 ps
300K	As above	40 ps

3.3 Results and Discussion

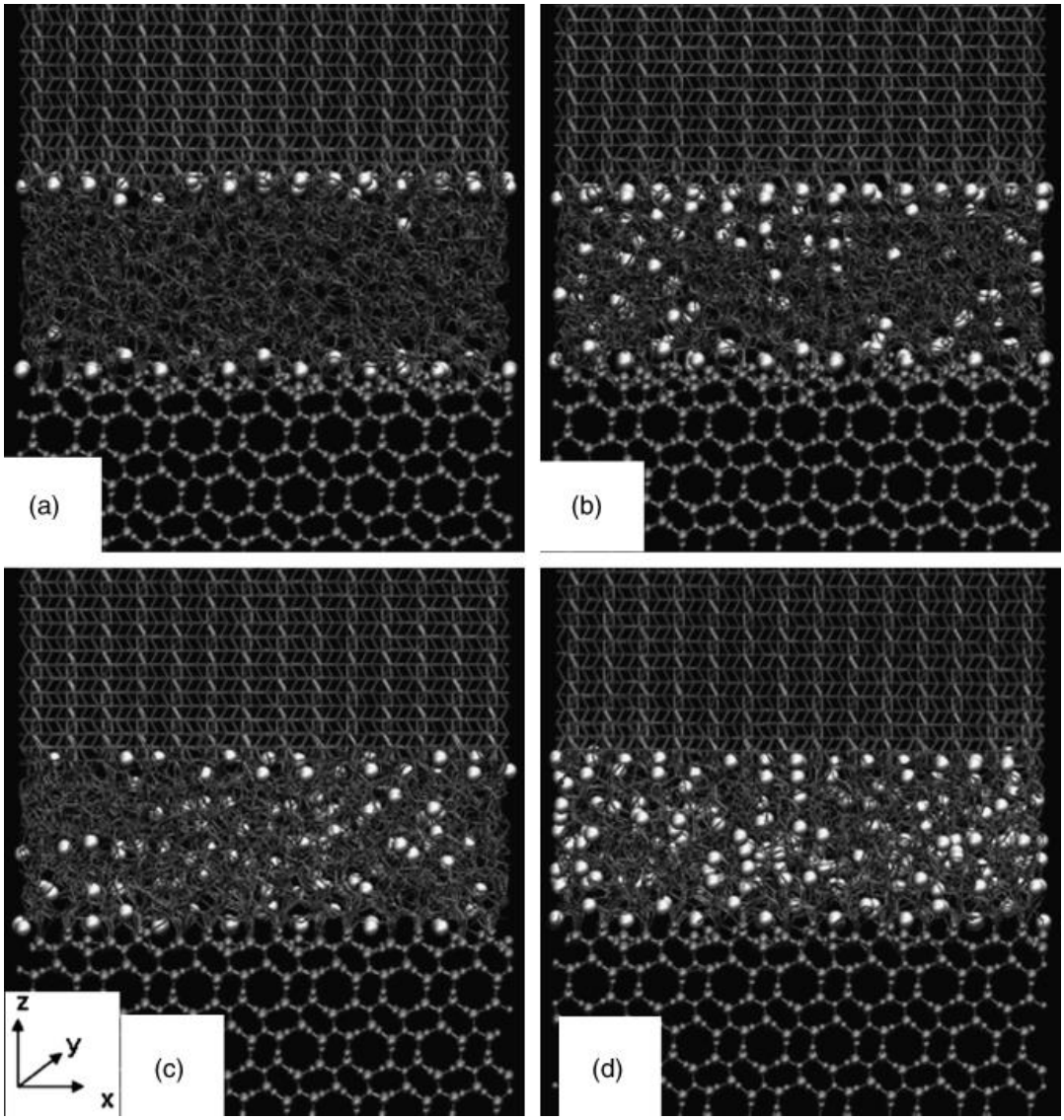

Figure 3.2 Side-view snapshots of final configuration after the melt-quench process for four compositions: (a) 0N3La, (b) 0N6La, (c) 30N3La, and (d) 30N6La in a system containing a 1.8~2 nm lanthanum silicon oxy-nitride IGF between a basal β-Si3N4 crystal on the top and a prism β-Si3N4 crystal at the bottom. All bonds are drawn within a 2.0Å cut-off distance. The large white spheres represent La ions. The smaller grey spheres represent Si ions that are in the prism oriented β-Si3N4

crystal. The smallest grey spheres represent N ions that are in the prism oriented β-Si3N4 crystal.

3.3.1 La Adsorption Sites and La Segregation

Figure 3.2 shows a side view of the final configurations for several different compositions in systems containing a lanthanum silicon oxynitride IGF between a (0001) basal-oriented silicon nitride crystal and a (10-10) prism-oriented silicon nitride crystal. Note that these snapshots in Figure 3.2 actually show the whole system thickness in the y direction (into the plane of the image). Atoms sizes here are just for easier viewing, in which the La are the large bright spots and Si and N in the prism-oriented crystal are the smaller gray spots. Bonds for Si-N and Si-O are included.

From Figure 3.2, it is clear that the La ions preferentially segregate to the crystal surfaces. This is consistent with earlier simulations of network modifying ions such as alkali and alkaline earth ions in silica IGFs that segregated to the surfaces in oxide and nitride crystals [81,92-94]. This segregation behavior is caused by the combined role of the additive in the silicate glass, which disrupts the Si-O network structure, and the availability of the interface to act as a sink for such modifying ions. Because of its large size, La ions similarly act as network modifiers and preferentially segregate out of the silica IGF.

Figure 3.2 (a) shows that the La ions on the prism surface sit at two very specific locations. This coverage changes with compositional changes, as will be discussed in more detail below. The important feature relevant to these adsorption sites is that they are present in all four images (but most clearly seen in the compositions with no N in the IGF (Figure 3.2 (a) and (b)) and are consistent with results obtained by Winkelman et al. from

their HAADF-STEM studies [37]. Figure 3.3 (b) shows an image from Winkelman et al., showing the location of the La ions at sites 1 and 2 (which are drawn by arrows in figure 3.3 (a)), also taken from Winkelman et al. Figure 3.3 (c) is a snapshot of one of our simulation results, showing that the La ions sit at two very similar positions as seen experimentally. Using the label in Figure 3.3 (a), Winkelman et al. indicated that the site 1 is 5.0 ±0.2Å in y and site 2 is 6.1±0.2Å. Our results put our sites 1 and 2 at 4.3±0.1Å and 5.7±0.2Å, respectively. While there is a slight difference, Dwyer et al showed that the HAADF-STEM images obtained from different groups for this same interface are slightly different, as discussed below with reference to Figure 3.6. Also note that the O-terminated Si3N4 open rings are observed on the prism surface in Figure 3.3 (c), indicating a strong tendency for O ions to replace N ions, which is consistent with DFT calculation from Walkosz *et al.*[77]. Nonetheless, it is clear that our relatively simple interatomic potentials reproduce the experimentally observed results very well.

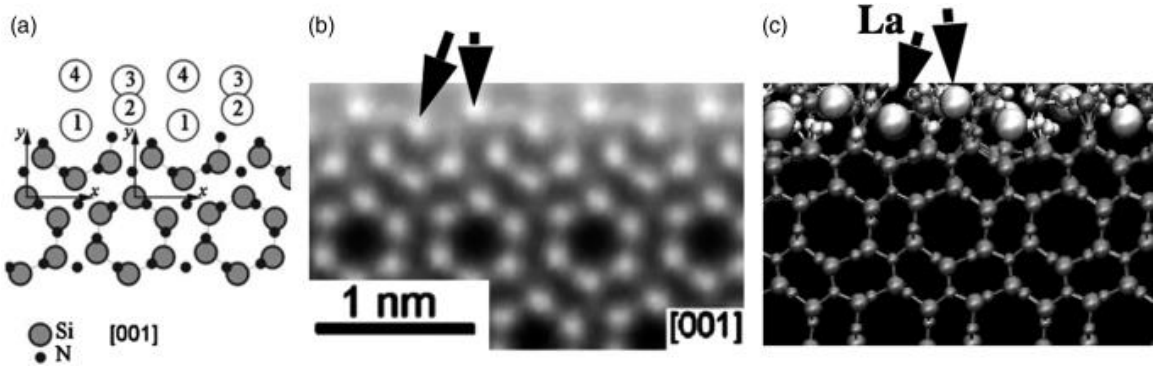

Figure 3.3 (a) Drawing of sites from Winkelman et al., (b) HAADF-STEM micrograph from Winkleman *et al.*[37], (c) Our MD simulation results of La locations at IGF/Prism interface where the Prism interface. Arrows show locations

of La ions at site 1 and 2 from both experiment and our MD simulations. The small white spheres represent O ions from the IGF

Besides showing locations of La ions on the IGF/crystal interfaces, Figure 3.2 also shows changes in La segregation with composition. 0N3La has an extremely clean La segregation picture as is shown in Figure 3.2 (a) with almost all La ions segregating into the interfaces. For Figure 3.2 (b) 0N6La, most La ions still segregate into the IGF/crystal interfaces, while some La ions are left in the glassy portion of the IGF. With N added to the IGF in Figures 3.2 (c) (30N3La) and Figure 3.2 (d) (30N6La), a significantly greater number of La ions remain in the interior IGF. The effect of adding N into the IGF is that there is a reduction of La ions segregating to the interface. This is seen in Figure 3.4, which shows the effective concentration of the La ions at each interface as a function of composition. The data in Figure 3.4 are normalized to the maximum number of sites available at each interface.

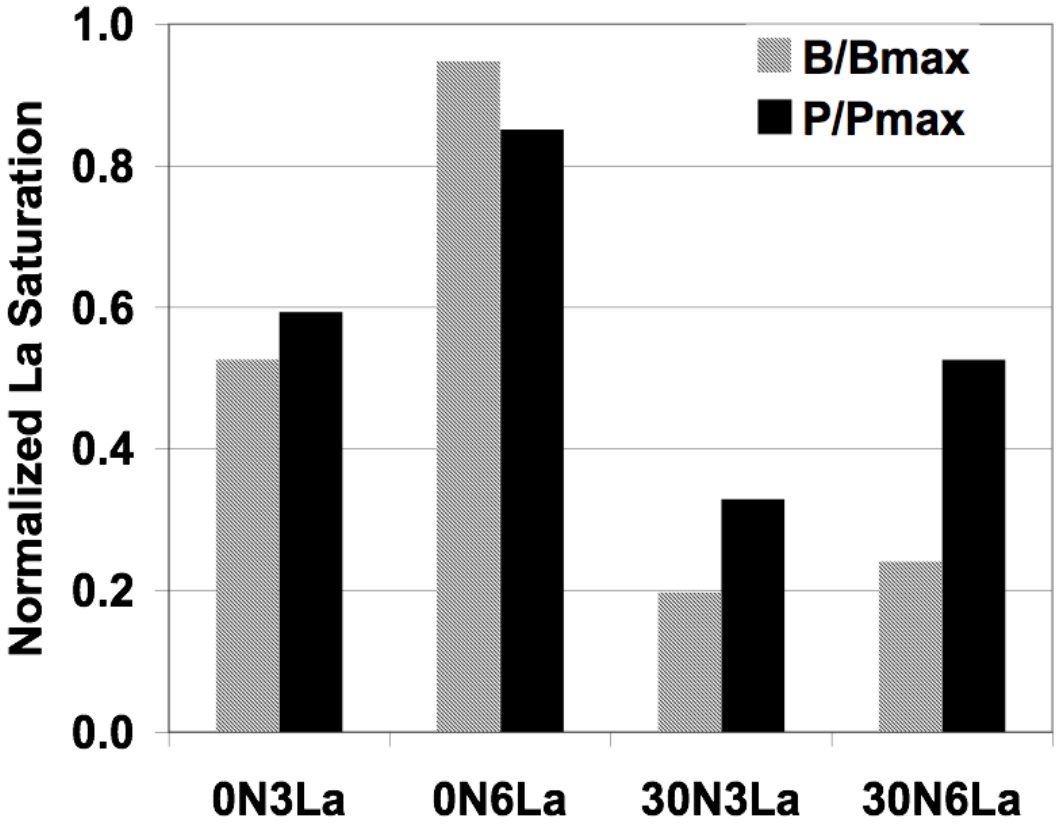

Figure 3.4 The saturation percentages of ordered La ions on the IGF/Basal and IGF/Prism interface for various compositions. B/Bmax means the actual La density divide by the La saturated density on the IGF/Basal interface. P/Pmax represents means the actual La density divide by the La saturated density including position 1 and 2 on the IGF/Prism interface.

As shown in Figure 3.4, increasing the La concentration in both the 0% nitrogen and 30% nitrogen cases causes an increase in the adsorption of La to each interface, with, in most cases, greater segregation to the prism surfaces than the basal. There is a significant decrease in segregation with increasing N content in the IGF and, importantly, much greater loss at the basal surface than the prism surface. These results are consistent

with our earlier studies of the effect of Al additions in calcium alumino-silicate IGFs on segregation of the additives to the interface, in which the Al ions need the charge compensation provided by the Ca ions to foster continued network glass formation[92,95]. Excess of either additive disrupted the silicate glass structure and imposed a driving force for segregation to the interfaces.

In the current case, the presence of N in the IGF offers sites for La that are possibly equivalent to the sites at the crystal surface. Since the experimental observations of La segregation are specific to the prism surface, we will concentrate on that interface. Figure 3.2 (a) and (c) show the loss of La ions from site 2 on the prism surface implying a difference in the binding energies of the La ions at these different sites. Conversely, figure 3.2 (a) and (b) show that increasing the concentration of La in the IGF causes an increased filling of site 2.

3.3.2 The Energy of La Ions

Figure 3.5 shows the energy of La ions at sites 1 and 2 on the prism surface and La remaining within the interior of the IGF. As inferred from the Figure 3.2, the binding energy for La at site 1 is stronger than for La at site 2 in the two cases with 0% N/(N+O) in the IGF, and the La ions in the interior of the 0N6La IGF are the most weakly bound (since no La resides in the interior of the IGF for the 0N3La system, no data exists for that region). This means that with no N, there is a strong energy driving force for La ions to move from the interior IGF to the IGF/crystal interface, sitting at site 1 on the IGF/Prism interface first, then site 2. With longer runs, it would be anticipated that the La ions remaining in the IGF in the 0N6La system would eventually migrate to the interface. Another important trend seen in Figure 3.5 is that no matter where La ions are located,

the binding energy of La ions becomes stronger when adding N. Most importantly, with N in IGF, there is a much smaller driving force for La ions to segregate into the interface. This supports Figure 3.2 and 3.4 from an energy perspective that La ions in the interior IGF do not have a strong driving force to migrate to the interfaces in the system containing N, thus resulting in fewer La at the interfaces (Figure 3.4) and increased La present in the glassy portion of the IGF (Figure 3.2 (c) and (d)).

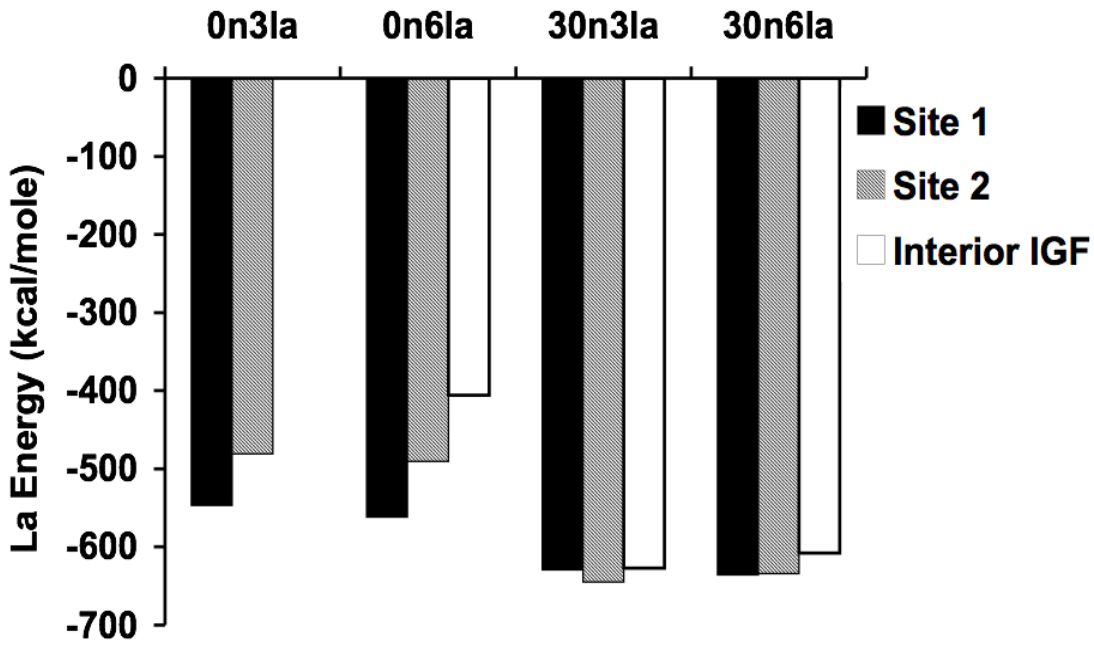

Figure 3.5 The energy of La ions at sites 1 and 2 for the prism and in the interior of the IGF for different compositions.

This effect of local composition in the IGF might offer a possible reason for the difference in the HAADF-STEM images of La locations from several very high-quality groups[75], two of which are shown in gray scale in Figure 3.6. The bright spots are indicative of the Si in the hexagonal rings in the nitride crystal, while the bright areas in

the IGF are indicative of La. Even though the experimental data come from similar samples, each local IGF may have a slightly different composition. Data from the Oxford group show La at sites 1 and 2, while the ORNL image shows slightly less ordered filling of sites 1 and 2, but with a significant La concentration with the IGF. These HAADF-STEM results would fit variations in our compositions with a lower N concentration in the Oxford IGF but a higher N concentration in the ORNL IGF.

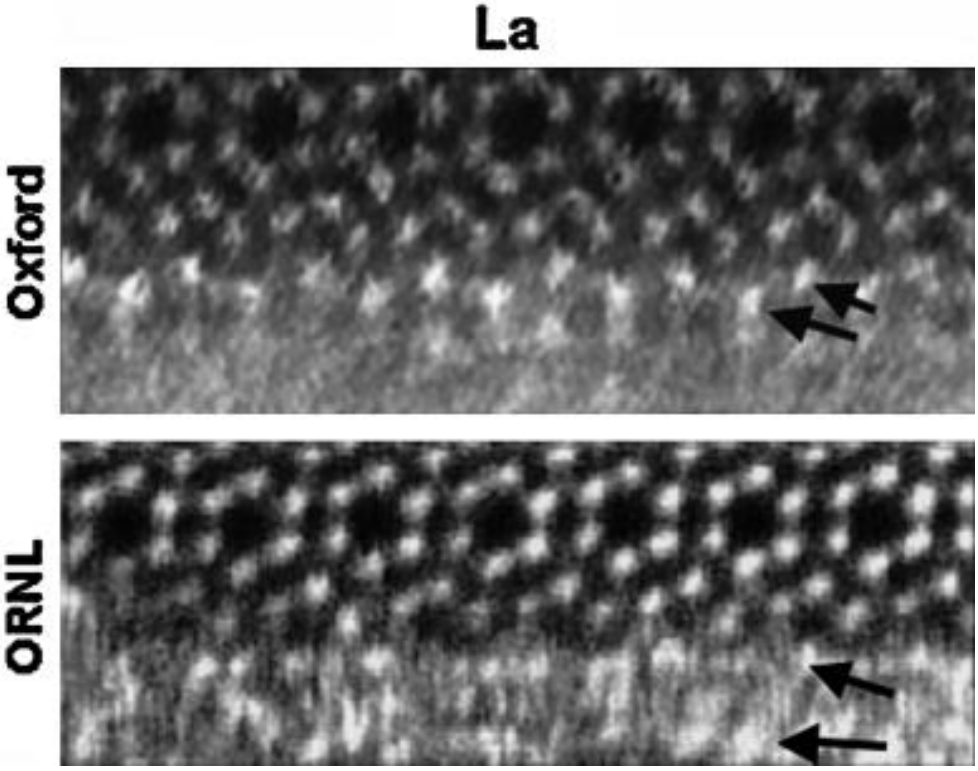

Figure 3.6 HAADF-STEM images for La ions at the nitride prism interface with the IGF showing slight differences in La locations both at the interface and within the IGF (at arrows) (modified from Dwyer et al.[75]).

3.3.3 Pair Distribution Functions for La-N

Figure 3.7 compares La-N pair distribution functions (PDFs) of La ions from site 1 to that of La ions from site 2 on the IGF/Prism interface for the four compositions. Several features are seen in the PDFs. The first peak for La(site 2)-N is shorter than that of La(site 1)-N for the two systems without N in the IGF (Figure 3.7 (a) and (b)), whereas the peaks are at similar locations for the systems containing N (Figure 3.7 (c) and (d)). (The first peak in Figure 3.7 (c) is split and shows a significant shoulder at the longer distance side of the first peak, indicating a lengthening not seen in the systems without N in the IGF.)

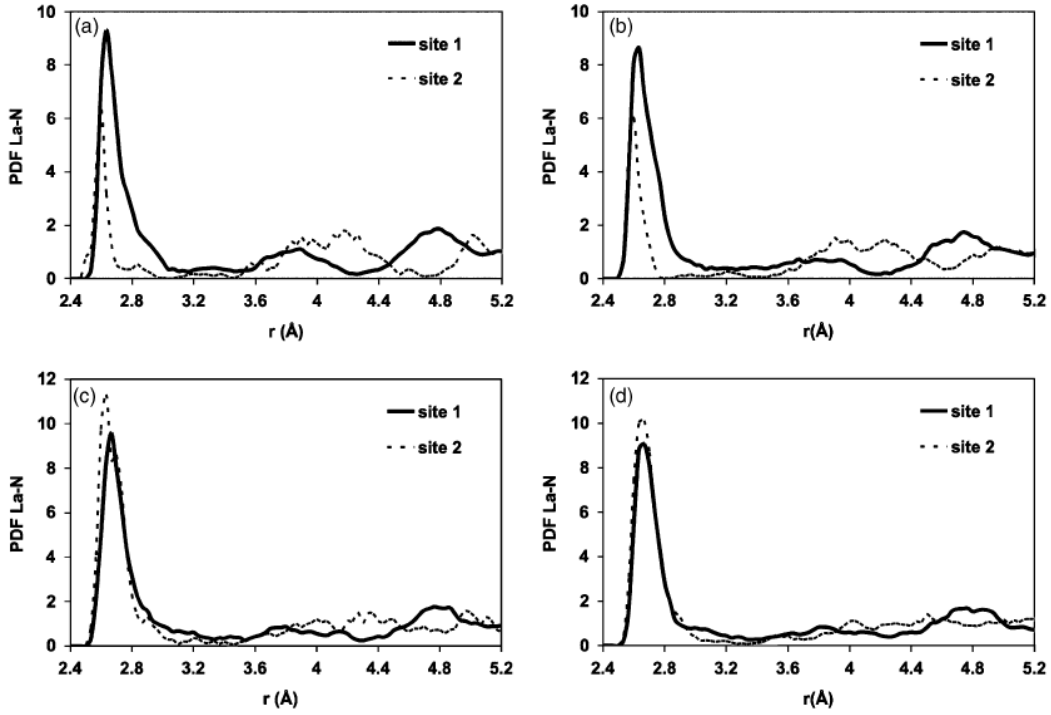

Figure 3.7 Pair distribution functions of La versus N for La ions at site 1 in comparison with La ions at site 2 on the IGF/Prism interface for (a) 0N3La, (b) 0N6La, (c) 30N3La, and (d) 30N6La.

There is also a change in the ‘medium range’ order with composition. La (site 1)-N clearly shows peaks at ~3.8Å and 4.8Å, with the 3.8Å peak decaying from Figure 3.7 (a) to (d). Without N in the IGF, these N in these La-N pairs in Figure 3.7 (a) and (b) come from the crystal and would be expected to be ordered. The addition of N into the IGF would provide additional N that are not as ordered, modifying this ‘medium-range’ order in Figure 3.7 (c) and (d). Similarly, La(site2)-N shows these longer peaks, but at slightly longer distances than in the site 1 case. This is due to the La at site 2 being farther away from the crystal, lengthening these medium range peaks from 3.8Å to 4.0Å and 4.8Å to 5.0Å. Again, with the presence of N in the IGF, this order decays in Figure 3.7 (c) and (d).

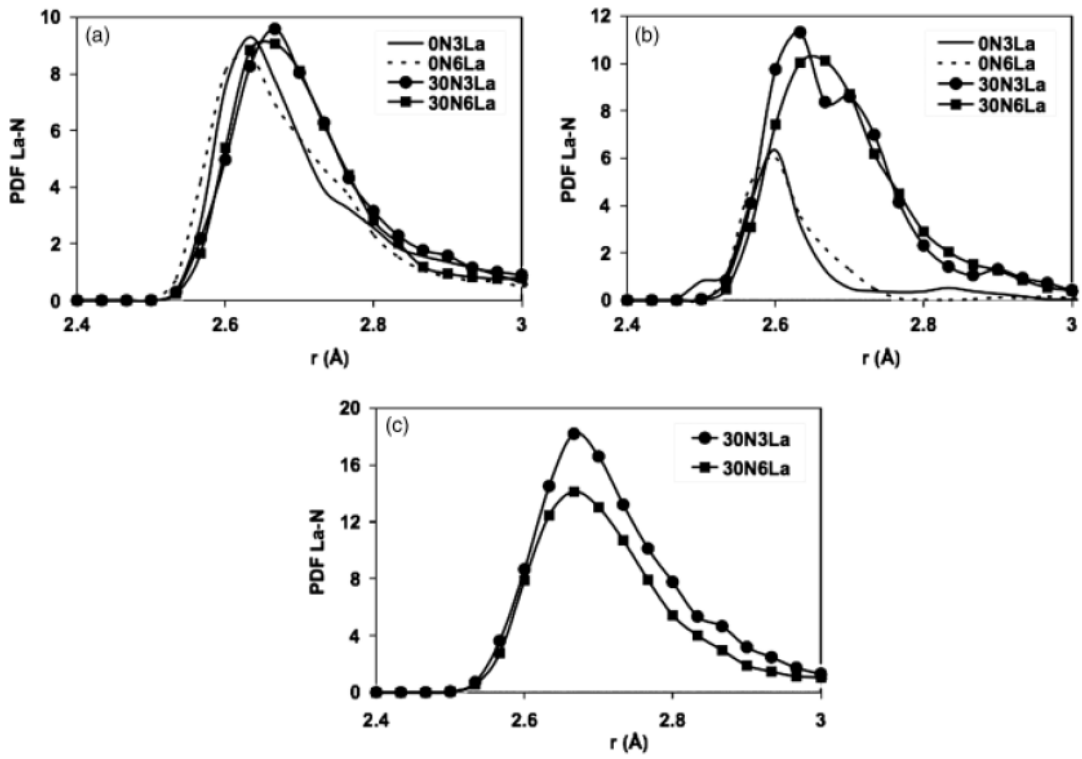

Figure 3.8 La-N PDFs of different compositions from various La locations (a) La at position 1, (b) La at position 2, (c) La in the interior IGF.

Figure 3.8 shows the La-N first peak in the PDF for La at site 1 (Figure 3.8 (a)), site 2 (Figure 3.8 (b)) and the interior of the IGF (Figure 3.8 (c)) as a function of the four compositions. For La at site 1, the La-N bond becomes longer with increasing N, while it becomes shorter with increasing La. However, for La ions from site 2 (Figure 3.8 (b)), the La-N bond again becomes longer with increasing N, but there is little change of the bond length when increasing La. Since there are not enough La ions in the interior IGF for 0% N/(N+O), Fig 3.8 (c) only shows that La-N bond length from the interior IGF for 30% N/(N+O) case. In the IGF interior, the La-N bond lengths are about the same for both 3%La and 6%La. More interestingly, we find that the La-N bond length at site 2 is

quite similar to that in the interior IGF for the 30% N/(N+O) cases by comparing Figure 3.8 (b) and (c), though the La-N bond length at site 1 is shorter than the interior IGF with no N. Nonetheless, these bond lengths, which vary from ~2.6Å to ~2.7Å, fit within the values observed by Chevire et al. for La-N bond lengths, in which they report values averaging ~2.7Å for their ternary lanthanum nitride to 2.63Å to 2.73Å for other ternary nitrides and ~2.65Å for the binary LaN[96].

3.4 Conclusions

The results of the molecular dynamics computer simulations of La ions in silicate intergranular films (IGFs) between basal and prism oriented silicon nitride crystals as a function of composition show adsorption of La ions to two sites on the prism surface consistent with HAADF-STEM results. Without nitrogen in the IGF, La segregation to each interface is similar. However, with nitrogen present in the silicate IGF (which is the more realistic experimental condition), increased La concentration causes a significant increase in the preferential adsorption at the prism surface than the basal surface. This would be consistent with the observed growth anisotropy for silicon nitride, in which adsorbed La acts to inhibit further growth along the prism surface normal. The variation in the binding energy of the La ions at the different surface sites and the interior of the IGF are consistent with the segregation behavior and the changes that occur with composition. There is also an implication of this result on the effect of La additions on strength. Changes in the local atomic structure at different locations observed in the pair distribution functions of the La-N pairs indicate shifts in bond length with composition and location.

Chapter 4 La_2O_3-doped Silicate Intergranular Films in Si_3N_4

4.1 Introduction

Intergranular films (IGFs) are amorphous nanometer-scale thin films that are observed at many grain boundaries in polycrystalline ceramics. IGFs make up only a small volume percent of the bulk ceramic, but their unique local chemistry can strongly influence the macroscopic properties of the material There have been a large number of studies to determine the structure and behavior of these IGFs[8,13,16-18,32,34-37,42,49,50,75,76,97-105] and the composition of the IGF has been shown to influence mechanical properties such as fracture toughness and interfacial debonding [8,16,31,32,49], surface and interface structure[100,106], high temperature properties[107,108], and abnormal or anisotropic grain growth [15,28,29,109].

It had previously been difficult to obtain atomistic details of the IGF by experiment because of their thin and amorphous nature, providing a complementary role for computational techniques[71,81,93,103,110,111]. Previous simulations of amorphous IGFs in oxide and nitride crystalline systems predicted the presence of density oscillations and ordering in the IGF at the IGF/crystal interface, induced by the crystal structure, extending into the IGF nearly 1nm, with adsorption of modifier cations in the silicate IGFs to specific surface sites[81,89,91-93,112-115]. Recent advances of electron microscopies (e.g. aberration-corrected high-resolution transmission electron microscopy (Cs-HRTEM), high-angle annular dark-field scanning transmission electron microscopy (HAADF-STEM), high-resolution transmission electron microscopy(HRTEM)) enable direct imaging of the IGF/crystal interfaces at the atomic level, showing the ordering at the interface predicted by the simulations[50] and segregation of specific species on the

interfaces[34-38,50,75]. Nevertheless, computer simulations provide details still not readily available in experiment, such as the energetics of specific sites at the interface or within the IGF, and the atomistic structure in the glassy portion of the IGFs.

Silicon nitride (Si_3N_4) ceramics are outstanding structural materials for high temperature applications whose microstructural and mechanical properties are sensitive to rare earth doping[22,24,59,63-66]. STEM images[35-37,75], ab-initio calculations[78,90] and MD simulations [116] have shown that rare earth ions take very ordered locations, dependant upon the RE species, along the IGF/Prism interface in Si_3N_4 ceramics.

Previous MD simulations showed preferential segregation of network modifiers (such as Na or Ca) in silicate IGFs to the interfaces in alumina and silicon nitride systems[81,91-93,113,114,117]. These simulations indicated the important roles of the modifier ion in the silicate glass as well as at the adsorption sites on the crystal surface that, in combination, drive such ions to a specific interface. Because of their potential role as modifiers in the silicate glass, RE ions show similar segregation behavior. Rather than inferring behavior of a RE ion based on other modifier species (such as Na or Ca), the current work is designed to simulate La for direct comparison to HAADF-STEM results, allowing for evaluation of the energetics and site filling properties.

4.2 Computational Procedures

4.2.1 Ion-ion Interactions

Similar to previous calculations[89,93,116], a multi-body interatomic potential, is employed in the molecular dynamics simulations. The two-body part consists of modified

Born-Mayer-Huggins (BMH) pair potential for all ion-ion interactions and an extra Lennard-Jones (LJ) pair potential for La-N interaction.

The modified BMH potential is given as

$$V_{ij}^{BMH} = A_{ij}\exp\left(\frac{-r_{ij}}{\rho_{ij}}\right) + \frac{z_i z_j e^2}{r_{ij}} erfc\left(\frac{r_{ij}}{\beta_{ij}}\right) \qquad (4.1)$$

where r_{ij} is the separation distance between ion *i* and ion *j*, z_i and z_i are full ionic charges of ion *i* and ion *j*, and in this case +3, +4, -2, -3 for La, Si, O, N, *e* is the elementary charge, and *erfc* is the complementary error function. Parameter A_{ij}, ρ_{ij} and β_{ij} for specific pair type are listed in Table 4.1.

Table 4.1 Parameters for modified BMH and LJ pair potentials

Atom pair	A_{ij} (fJ)	ρ_{ij} (pm)	β_{ij} (pm)	ε (fJ)	σ (pm)
O-O	0.0725	29	234	-	-
N-N	0.07241	29	220	-	-
Si-Si	0.1877	29	230	-	-
La-La	0.3975	45.1	230	-	-
N-O	0.1350	29	221	-	-
Si-La	0.3000	32	230	-	-
Si-O	0.2962	29	234	-	-
Si-N	0.7500	26.1	220	-	-
La-O	0.7377	31.75	270	-	-
La-N	3.9700	33.2	200	0.00395	195.6

The LJ potential has the form

$$V_{ij}^{LJ} = 4\varepsilon\left[\left(\frac{\sigma}{r_{ij}}\right)^{12} - \left(\frac{\sigma}{r_{ij}}\right)^{6}\right] \qquad (4.2)$$

where r_{ij} is the separation distance between ion *i* and ion *j*, and parameter ε and σ are given in Table 4.1.

The three-body part is given by

$$V_{jik}^{3-body} = \lambda_{jik} \exp\left(\frac{\gamma_{ij}}{r_{ij} - r_{ij}^{0}} + \frac{\gamma_{ik}}{r_{ik} - r_{ik}^{0}}\right)\Omega_{jik} \qquad (4.3)$$

for the case of $r_{ij} < r_{ij}^{0}$ and $r_{ik} < r_{ik}^{0}$. Otherwise, $V_{jik}^{3-body} = 0$. Its angular term is given in the following equation.

$$\Omega_{jik} = (\cos\theta_{jik} - \cos\theta_{jik}^{0})^{2} \qquad (4.4)$$

where θ_{jik} is the angle formed by ion *j*, ion *i* at its vertex, and ion *k*. The three-body potential is centered only on Si, O, and N ions. Parameters for the three-body potential are listed in Table 4.2.

Table 4.2 Parameters for three-body potential

Atom triplet	λ_{ij} (fJ)	γ_{ij} (pm)	r^{0}_{ij} (pm)	θ^{0}_{jik} (deg)
Si-O-Si	0.001	200	260	109.5
Si-N-Si	0.035	260	280	120
O/N-Si-O/N	0.024	280	300	109.5

4.2.2 Computational System

The three-dimensional simulation system containing the IGF between basal and prism oriented β-Si_3N_4 crystals is designed as shown in Figure 4.1. While a high index crystal orientation is usually observed bounding the IGF opposite a prism oriented crystal, the basal surface is chosen here for simplicity to apply periodic boundary conditions in x and y. A reflecting boundary is applied within each crystal in z to prevent atoms migrating into the crystals.

There are 7056 atoms in basal crystal and 7056 atoms in prism crystal, each with dimensions ~53Å×53Å×26Å. About 4800 atoms are first randomly distributed to form the glassy IGF, and are then melted and quenched by a process given in Table 4.3 to ~18 Å thick, similar to previous work[89], but with quench time orders of magnitude longer. The time step is 1fs.

Various IGF compositions (3%, 6%, 9% La and 0%, 15%, 30%, 50% N) are studied, as shown in Table 4.4, to investigate the atomistic structure of lanthanum silicon oxynitride IGFs as a function of composition.

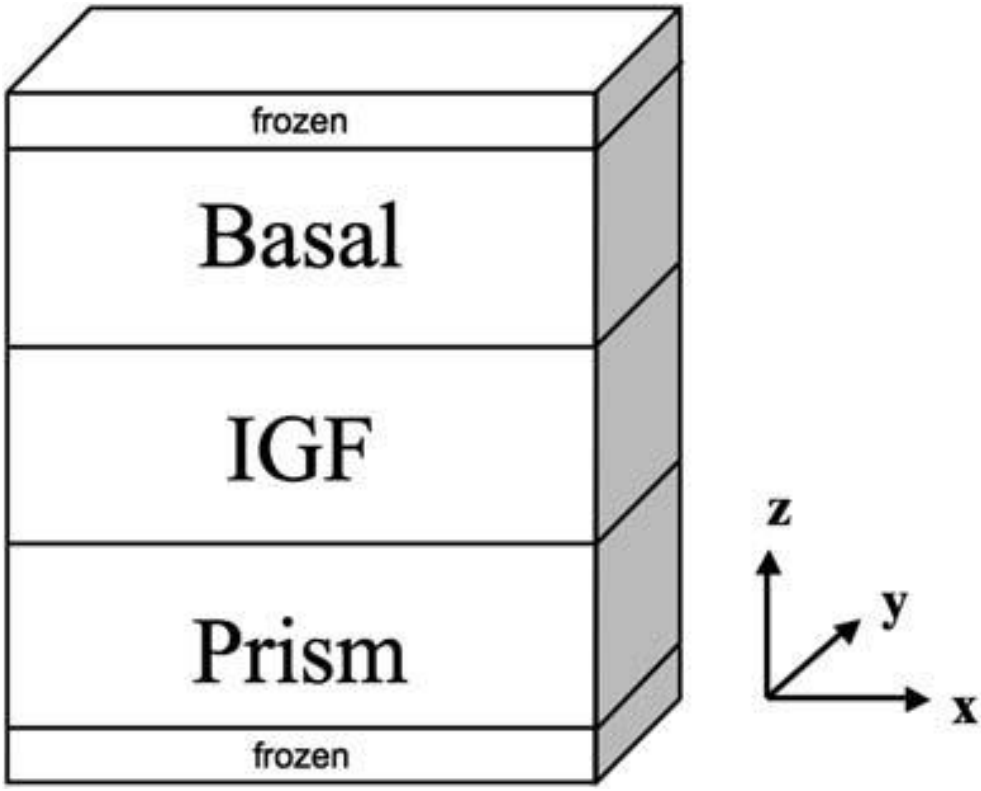

Figure 4.1 Drawing of the simulation system with IGF between basal and prism β-Si_3N_4 crystals. Here, a 3Å gap is left between the IGF and each crystal as a very initial starting configuration before the melt quench process.

Table 4.3 Melt-quench process

Melt/Quench Temperature	Conditions	Duration
300K	NVE, crystal frozen	10 ps
10,000K	NVE, crystal frozen	20 ps
9000K	x,y constant, P_z = 3 GPa, crystal frozen	1000 ps
8000K	As above	1000 ps

7000K	As above	1000 ps
6000K	As above	1000 ps
5000K	As above	1000 ps
4000K	As above	1000 ps
3000K	x,y constant, P_z = 3 GPa, crystal de-frozen	1000 ps
2000K	NpT, p = 0.1 MPa	200 ps
1000K	As above	20 ps
300K	As above	40 ps

Table 4.4 Compositions of IGFs

Sample	La	Si	O	N	Total	La/Total	N/(N+O)
0N3La	144	1481	3178	0	4803	3%	0%
15N3La	144	1558	2636	464	4802	3%	15%
30N3La	144	1632	2118	908	4802	3%	30%
50N3La	144	1726	1466	1468	4804	3%	50%
0N6La	288	1361	3154	0	4803	6%	0%
15N6La	288	1437	2616	460	4801	6%	15%
30N6La	288	1510	2102	900	4800	6%	30%
50N6La	288	1603	1454	1456	4801	6%	50%
0N9La	432	1240	3128	0	4800	9%	0%
15N9La	432	1320	2598	460	4810	9%	15%
30N9La	432	1391	2086	896	4805	9%	30%
50N9La	432	1481	1444	1444	4801	9%	50%

4.3 Results and Discussion

4.3.1 La Ordering and Adsorption Sites

Figure 4.2 clearly shows layers of La ordering on the prism interface after going through a melt state to the low temperature configuration. As is observed in our previous MD simulations[116], La adsorption at sites 1 and 2 on the IGF/Prism interface(bottom arrows) is again observed for almost all the compositions in our current MD simulations with a longer quench time. One important feature, as shown in Figure 4.2, is that La ions sitting at sites 3 and site 4 (upper arrows) are clearly observed on the IGF/Prism interface in samples 15N6La, 15N9La, 30N6La, and 30N9La, which is in excellent agreement with experimental results[37]. Because the separation distance perpendicular to the surface between sites 1 and 2 is small, these are considered in the discussion below as the 'first' ordered layer; similarly, sites 3 and 4 will be considered as the 'second' ordered layer.

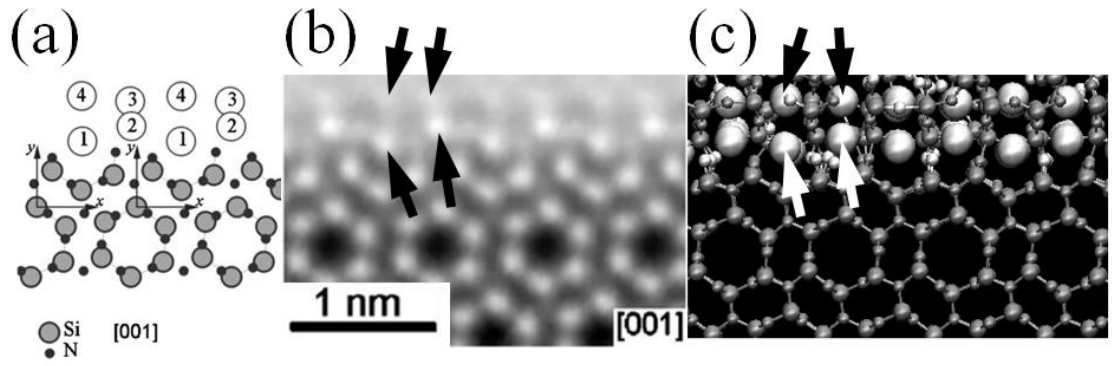

Figure 4.2 Four specific locations of La ions on the IGF/Prism interface viewed along the [001] direction. (a) Drawing of La sites from Winkelman *et al.*[37]; (b) HAADF-STEM image from Winkelman *et al.*[37]; (c) our MD simulation results. Arrows are used to point out La sites 1, 2, 3, and 4 from experiments and simulations. In (c), big white spheres represent La ions; small white spheres

represent O ions; the smallest grey spheres represent N ions; bigger grey spheres represent Si ions.

4.3.2 Compositional Effect

Figure 4.3 (a) shows that La ions fill sites 1 and 2 as a first ordered layer on the prism interface, while (b), with the absolute number of La ions doubled, clearly shows La ions fill two ordering layers as sites 1, 2, 3 and 4. A general trend here is that with increasing La content from 3%La to 6%La, more sites (La sites 1, 2, 3, 4 in Figure 4.2) on the prism interface get filled for the case of 30%N/(N+O), which has the experimental N concentration[17]. The same trend is also observed for the 15%N/(N+O) case. Figure 4.3 also shows a strong preferential segregation of La ions to both the prism and basal interfaces, similar to previous work[116]. Additionally, it should be noticed that on the prism interface, the bonds drawn near this interface at the higher La concentration in 4.3 (b) become more ordered as compared to the bonds in 4.3 (a) due to the formation of the second layer of La at sites 3 and 4.

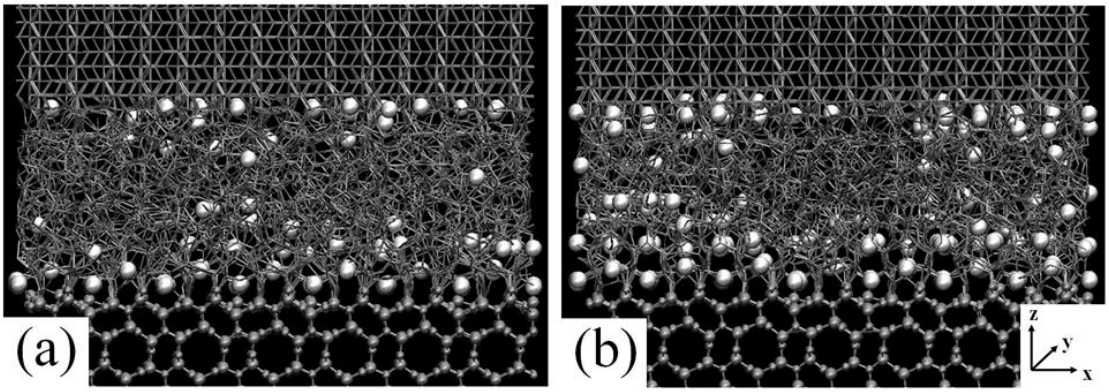

Figure 4.3 Snapshots of final configurations of our MD simulations taken from the y direction for the entire thick system (not a slice of the system), which contains a ~1.8 nm thick IGF in contact with a basal oriented silicon nitride crystal on the top and a

prism oriented silicon nitride crystal at the bottom for samples (a) 30N3La, (b) 30N6La. Here, atom types same as listed in Figure 4.2. Bonds between ions are drawn for the entire system with a cutoff distance of 2 Å.

Figure 4.4 shows two important features associated with increasing N from (a) to (d) at constant La content in these IGF compositions: (1) there are more La ions remaining in the interior of the IGF after saturation of sites on the prism surface and (2) there is a significant depletion of La ions from the basal surface. In particular, at low N content in Figure 4.4 (a) and (b), almost all the La ions segregate to the prism and basal interfaces, showing clear segregation; at higher N content, Figure 4.4 (c) shows a few La ions randomly in the glassy portion of the IGF, and (d) shows more La ions staying in the interior IGF. Importantly, Figure 4.4 (c) and (d) show the significant depletion of La ions from the basal surface with increased N concentration. This indicates that the presence of N in the IGF has a significant impact on the adsorption of La ions at the basal interface, but no such negative effect on the prism interface. In fact, as shown below, N in the IGF enhances ordering of La on sites 3 and 4 on the prism side. La at site 2 is missing in Figure 4.4 (a), which could result from not enough La ion adsorption on the prism interface and a lower energy level of site 1 compared to site 2 (the binding energies of La at the different locations will be shown below). These results suggest that there is a preferential segregation of La ions on the prism surface versus the basal interface with increasing N. This has important implications on the growth behavior of the nitride crystal along the surface normal of these different surfaces, affecting anisotropic grain growth in a manner consistent with experimental observations, as will be discussed below.

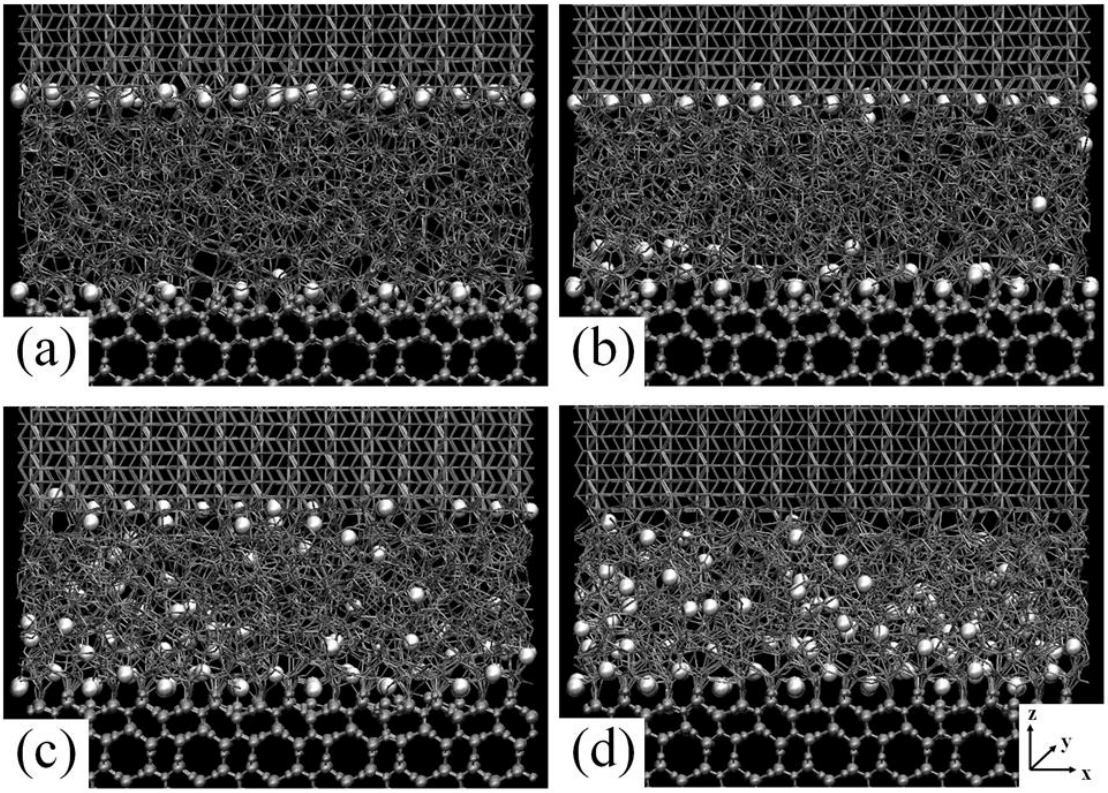

Figure 4.4 Snapshots of the final configurations of our MD simulations for samples with same La content, different N content: (a) 0N3La, (b) 15N3La, (c) 30N3La, (d) 50N3La, similar to Figure 4.3.

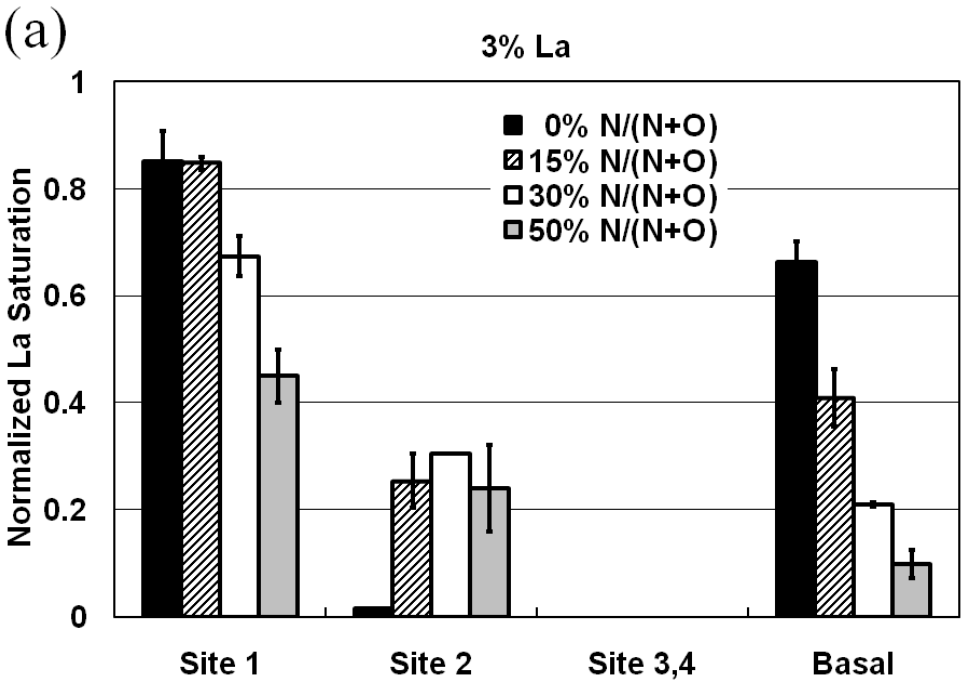
(a)
3% La
Normalized La Saturation
1
0.8
0.6
0.4
0.2
0
0% N/(N+O)
15% N/(N+O)
30% N/(N+O)
50% N/(N+O)
Site 1
Site 2
Site 3,4
Basal

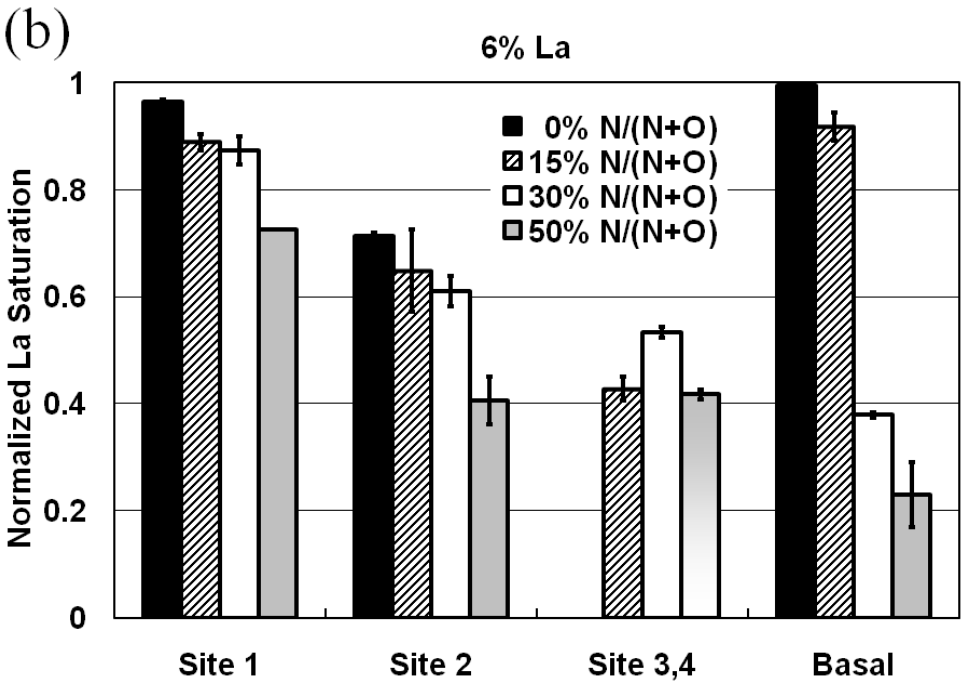
(b)
6% La
Normalized La Saturation
1
0.8
0.6
0.4
0.2
0
0% N/(N+O)
15% N/(N+O)
30% N/(N+O)
50% N/(N+O)
Site 1
Site 2
Site 3,4
Basal

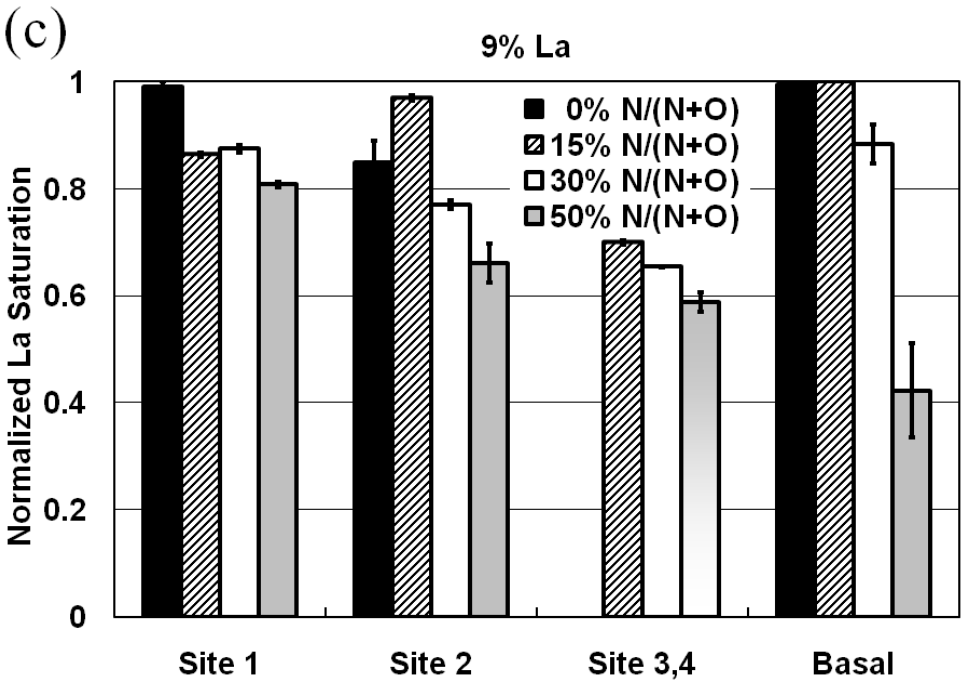

Figure 4.5 Normalized La saturation percentages of sites 1, 2, 3, 4 and basal for (a) 3% La, (b) 6% La, and (c) 9% La, data derived by using the average La density of two systems with different starting configurations divided by the maximum La density of that specific site. Error bars are drawn. Data of sites 3 and 4 for the 50%N/(N+O) cases are marked gradient gray because of the vague La ordering at sites 3 and 4.

Figure 4.5 gives numerical details about La segregation. A clear trend in (a)-(c) is that adsorption at all sites, either on prism or basal, increases with increasing La content. This also supports Figure 4.3, showing the filling of sites 3 and 4 on the prism interface with increasing La content. Another very important trend is that site filling on the interface decreases for the same La content with increasing N content, indicating a decrease in the driving force for segregation to the interface and an increasing La distribution in the interior IGF. Supportive of Figure 4.4, the decrease in adsorption at the

basal interface is much more significantly reduced with increasing N content than that on the prism interface.

4.3.3 Energy of La Ions

Figure 4.6 shows the average energy of La at specific sites on the prism surface, in the interior of the IGF, and on the basal surface. The figure shows that at the same La content the La energy becomes lower, or more negative, with increasing N content, which indicates that N ions can strongly affect the binding energy of the La ions at the different locations. One important aspect is the role of the N in the IGF on the energy of La at sites on the prism surface. While the N has a small effect on lowering the energy at the basal surface, there is a greater binding to sites at the prism surface, especially those 'outer' sites 2, 3, and 4. At those sites, the La interaction with the crystal N in the prism surface decreases with distance from the surface. The addition of N in the IGF allows these N to associate with the La at sites 2-4, lowering their energy and stabilizing them. This is clearly seen in the difference in energy of La at site 1 in comparison to La at site 2 with no N at all La contents, where site 1 is lower than site 2. Sites 1 and 2 become energetically similar as N is added. In ab-initio calculations of La at these different sites on the prism surface, Painter et al obtained binding energies for the La interacting with only 3 anion (N) near neighbors on the prism surface at a short distance caused by the directional nature of the bonding towards the crystal because of the lack of presence of the rest of the IGF[78]. As they report, the calculated perpendicular distance of the La from the surface was in the 1.6-1.8Å range, whereas HAADF-STEM put the distance at 2.4Å. If the rest of the IGF were included in such a calculation, an additional set of La-

anion bonds would occur and, as our simulations show, the distance from the surface would be more in line with experiment.

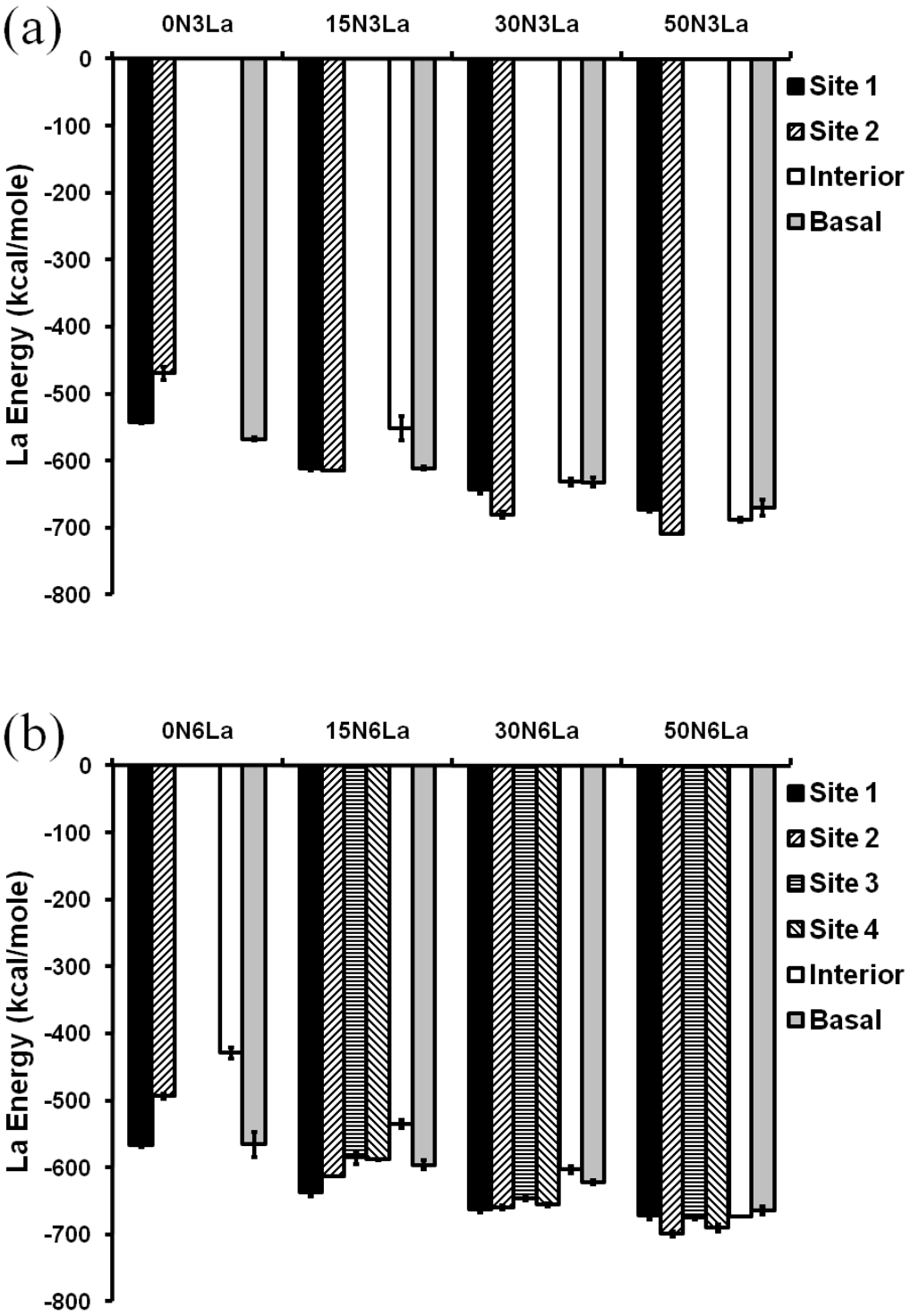

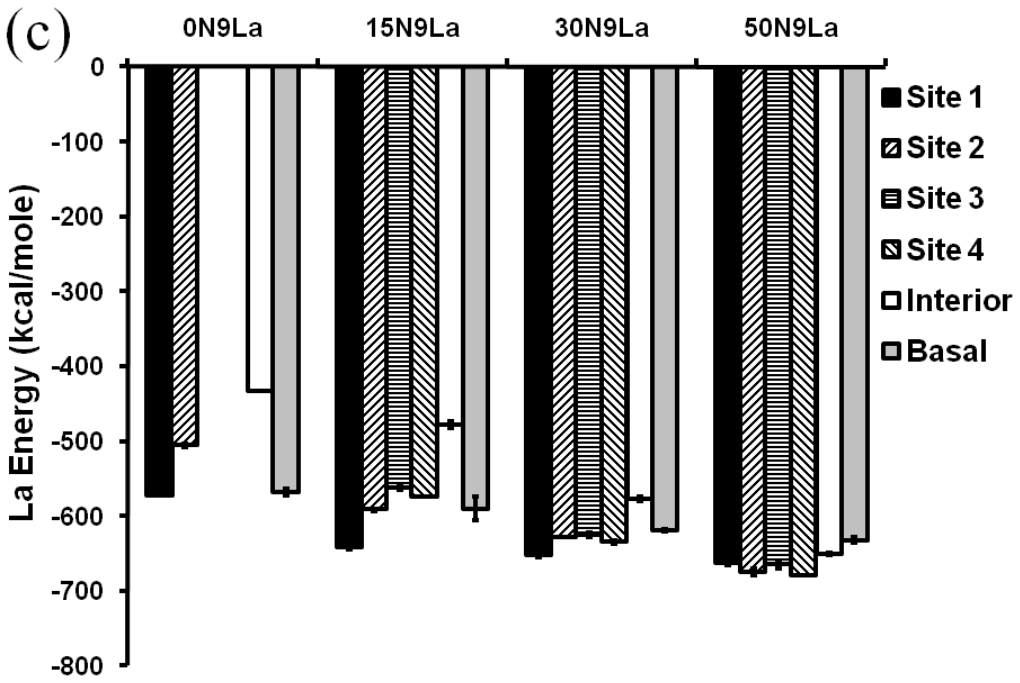

Figure 4.6 Energy of La ions at different locations, averaged by two systems with different starting configurations. Error bars are used.

The change in segregation behavior shown in Figure 4.4 is supported by data in Figure 4.6. At low N content (e.g. 0% N/(N+O) and 15% N/(N+O)), there is a significant difference in the energy of the La in the interior of the IGF in comparison to La at the crystal surfaces, providing a strong driving force for segregation to the interfaces for the interior La ions, which explains Figure 4.4 from an energy perspective. As N content increases, there is a lowering in the energy of the La in the interior of the IGF, becoming closer to the binding energy of the La at the prism interface so that at high N content (e.g. 30% N/(N+O) and 50% N/(N+O)), the energetic driving force for segregation decreases, therefore leaving La ions in the interior IGF, which is also consistent with Figure 4.4. At 50%N in the IGF, the energy of La in the IGF interior is lower than that of La at the basal surface, causing the depletion of La from the basal surface seen in Figure 4.4 (d).

4.3.4 Pair Distribution Functions and Coordination Number

Pair distribution functions (PDFs) of the cation-anion interactions provide additional information regarding structure of La ions at the different locations. The first peak of the La-O PDFs ranges from 2.4Å to 2.66Å in our simulation, which is within the range of 2.41Å to 2.75Å in the Na_2O-La_2O3-B_2O_3 system[118]. This is also in good agreement with data in the lanthanum aluminate glass, in which the La-O bond length is reported to be 2.521Å from the neutron and X-ray data[119].

The first peak of the La-N PDFs ranges from 2.56Å to 2.73Å. This is within the range of 2.45Å to 3.22Å reported by Chevire et al., in which the average La-N bond length of ~2.65Å in binary and ~2.7Å in ternary lanthanum nitride are reported[96].

Figure 4.7 shows the first peak for La-N pairs in sites 1 and 2 on the prism surface with increasing N content for the 3%La cases (a and c) and 6%La cases (b and d). At 3% La (Figure 4.7a), there is little change in the peak location with increasing N content in the IGF at sites 1 or 2 (Figure 4.7a and c), although, as shown in Figure 4.5 (a), there are few La at site 2 at 0N3%La. However, at 6% La both sites 1 and 2 are occupied (Figure 4.5 (b)) and Figure 4.7 (b) and d show the La-N peak maximum is at a shorter distance with no N in the IGF as compared to the cases with N added. The only N available to the La at site 2 at 0%N are those on the prism surface, causing the slight decrease in La-N bond length so as to increase bond strength. This strong La-N directional bonding towards the N on the surface with 0N is offset by the addition of N in the IGF, causing the slight increase in bond length.

The coordination number (CN) of O plus N ions around the La remains about 7-8 at different locations of the IGF for all compositions, with an increase in one anion being

offset by a decrease in the other anion. The CN of N around the La is less arbitrary than that for the O because of the broad nature of the La-O peak, making the CN less accurate. In the literature, La coordination to O is reported to be 7.01 from diffraction data[119] and 7.35 in Du et al's simulation[120] in lanthanum aluminate glass, and 8 or 9 in Na_2O-La_2O_3-B_2O_3 system[118] and $La_9OMg[SiO_4]_6[SiO_3(OH)]$ system[121]. La coordination to N is reported to be 7 in the ternary nitride La_2GaN_3[96]. In the simulations, the CN is derived by using the cutoff distance of 3.3Å for La-N and 3.2Å for La-O, which is the first minimum after the first peak for each. The CN of either O or N ions around La ions does not vary at different locations at the same N content but different La content (as an indicative of stable IGF). When increasing N at constant La content, the CN of O ions around La decreases, while the CN of N ions around La increases. This change in coordination allows for stabilizing the La ions at the outer surface adsorption sites 2, 3, and 4, as well as within the interior of the IGF, depending upon N content.

With increasing La content at constant N content, the simulations show an increase in N in the IGF bonded to 2 Si at the expense of N bonded to 3 Si. This is consistent with the differential binding energy scheme proposed by Painter et al using ab-initio calculations [90], although here we recognize its importance not only to the interfacial segregation, but also to La within the IGF.

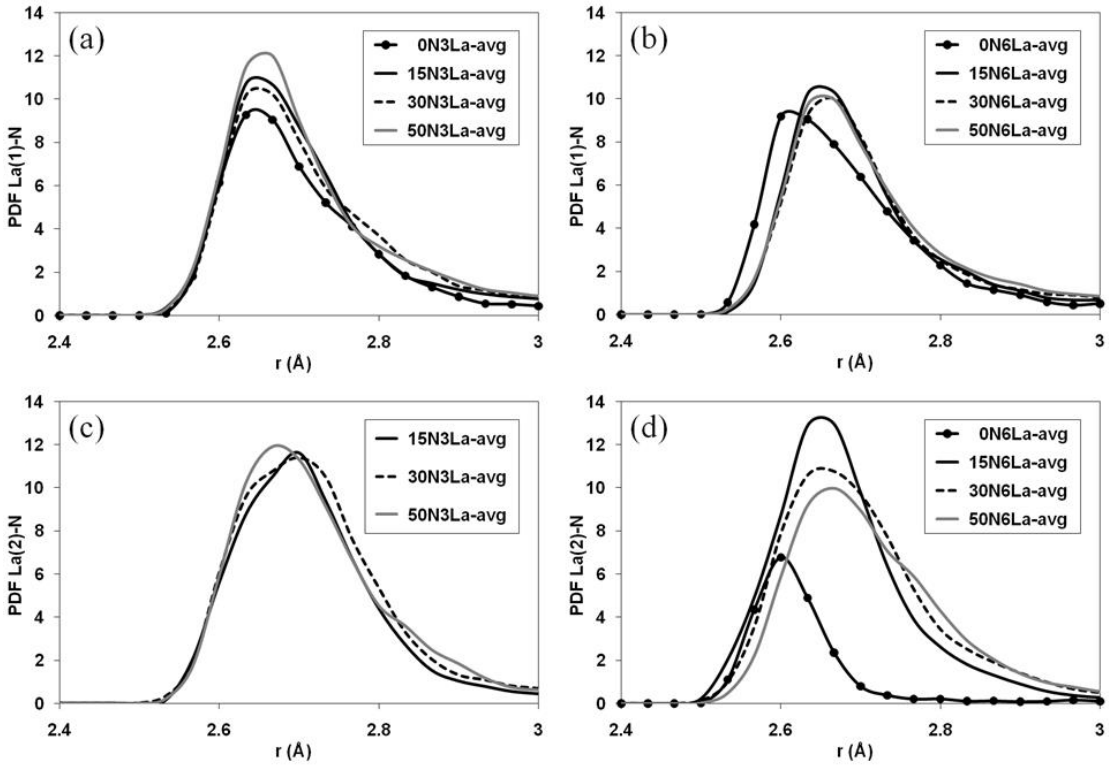

Figure 4.7 Average La-N PDFs of systems from two different starting configurations for various N contents at (a) 3%La and (b) 6%La, where the central La ions are from site 1; (c) 3%La and (d) 6%La, where the central La ions are from site 2.

4.3.5 Basal Growth and Partial Basal Growth

While the prism surface is readily 'poisoned' by the La additive, which is consistent with experiment, the basal orientation offers more complex behavior. Experimentally, growth of the basal surface outward is often compositionally compromised so that sometimes it occurs and other times pyramidal planes grow (forming a rounded cap) [24]. Complex behavior at the basal surface as a function of composition in the IGF is shown in Figure 4.8. Figure 4.8 (a) shows that the basal oriented silicon nitride crystal continues to grow one more full layer at high N, low La

content. However, it should be noted that the new grown basal layer shown in Figure 4.8 (a) is not fully silicon nitride but is rather a silicon oxy-nitride. Figure 4.8 (b) shows partial basal growth behavior at high N and high La content, where the basal surface continues to grow neatly in some region, but in some other region, as pointed out by the white ellipse, the basal growth is stopped by the amorphous IGF. Continuation of this would potentially allow for a rounded surface or growth of 'pyramidal' planes rather than growth of the flat basal planes, similar to experiment [24]. Because of the constant segregation of La to the prism surface at all compositions containing La ions, the prism surface is preferentially 'poisoned' by the additive ions, inhibiting growth along the surface normal of this orientation. Because La adsorption on the basal surface is compositionally dependent and preferentially does not occur at higher N content, anisotropic grain growth would occur, forming whiskers, as observed experimentally. This preferential segregation of network modifier ions from the IGF that inhibit growth of specific orientations in the nitride is similar to behavior observed for other network modifier ions in silicate IGFs in oxides [92,112] (although preferential segregation is to a different surface in the oxide studied) as well as to experimental results [24]. These results imply that different IGF compositions locally bounding the basal surface would create different growth patterns as a function of composition during the dynamically kinetic process of liquid phase sintering, but as long as La is available, outward growth of the prism plane is inhibited, allowing for anisotropic growth.

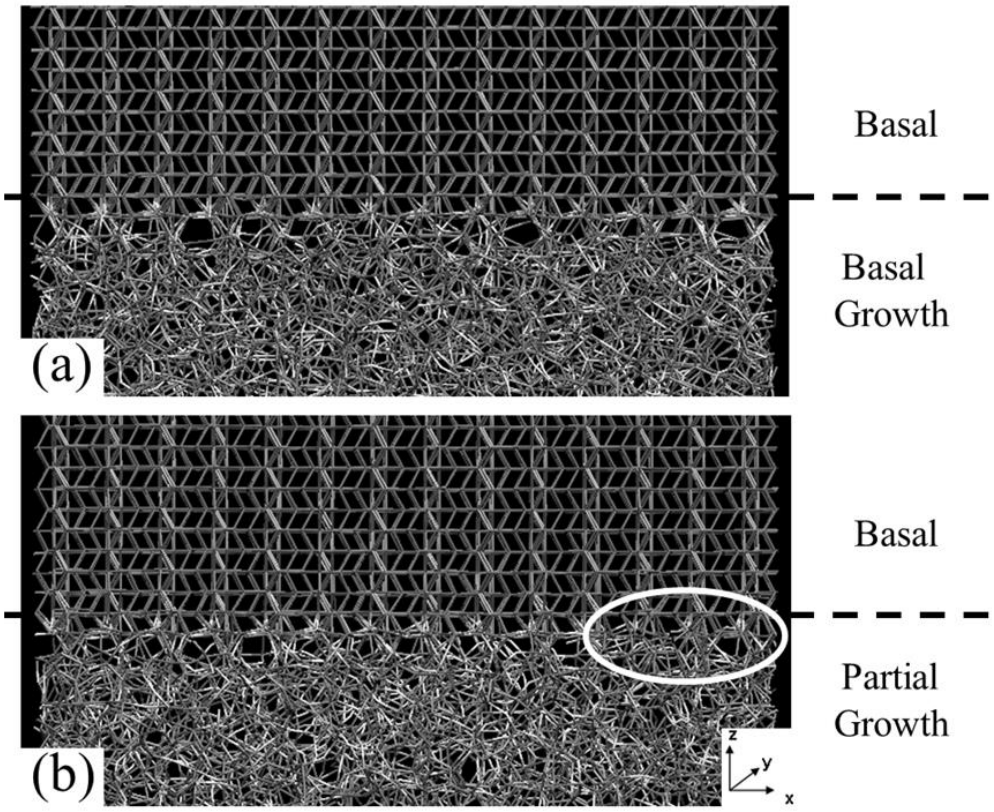

Figure 4.8 Snapshots of (a) basal growth (50N3La), and (b) partial basal growth (50N6La). Dashed lines are drawn to distinguish the original basal crystal and the new basal portion. Only bonds are drawn for better view. Bond features are similar to Figure 4.2, Figure 4.3 and Figure 4.4. A bright circle is drawn in (b) to point out the region where basal growth is disrupted.

4.4 Conclusions

The MD simulations of La silicon oxy-nitride IGFs between basal and prism oriented silicon nitride crystals show results of La adsorption consistent with HAADF-STEM results, and also show the effect of composition on this behavior that is not readily available experimentally. La adsorption at sites 1, 2, 3, 4 on the prism oriented silicon

nitride surface are observed for specific compositions in our simulations, at locations precisely consistent with HAADF-STEM results. With increasing La content, La site-filling increases on both prism (especially sites 3 and 4) and basal interfaces. Because of La's role as a network modifier in pure silica glass, IGFs with no N and low La content show complete segregation of the La to the crystal surfaces. Increasing N content in the IGF reduces this La segregation to the interfaces, allowing for more La in the interior IGF. This is consistent with the change in binding energy of the La ions in the IGF interior in comparison to that at the interfaces, reducing the driving force for segregation. Increasing N content in the IGF causes preferential La depletion from the basal surface, with no such depletion of La on the prism surface, offering a mechanism for the anisotropic grain growth observed in this system.

Chapter 5 Effect of Thickness and Composition on the Structure and Ordering in La-doped Intergranular Films between Si_3N_4 Crystals

5.1 Introduction

Many studies have been devoted to silicon nitride ceramics (Si_3N_4) because of their outstanding structural and mechanical properties for high temperature applications. The mechanical properties of silicon nitride ceramics are strongly influenced by the microstructure and the chemical compositions of the grain-boundary phase, making the study of intergranular films (IGFs) of great importantce.

Intergranular films are amorphous thin films (about 1~4nm thick) forming from impurities or sintering additives at grain boundaries in polycrystalline ceramics. IGFs occupy a small volume percentage of the bulk ceramic, have their structure and composition largely different from bulk[12-14], and play an important role in tailoring the macroscopic properties of the bulk ceramics[5,14-16,18-25,48], such as fracture toughness[8,16,31,32,49] and high temperature properties[107,108]. For instance, abnormal grain growth behavior is significantly affected by the composition and structure of the IGF[15,28,29,122]. Prior to a number of recent advances in electron microscopy[34-39], it had been difficult for experimentalists to obtain the atomistic details of the structure, composition and distribution of species in the IGF because of their thin and glassy nature, the most important contributions were made by computational simulations[71,81,93,103,110,114,123,124]. The recent advances in microscopy include aberration corrected HRTEM and high-angle annular dark-field scanning transmission electron microscopy (HAADF-STEM), which can capture images at the atomic level and provide some atomistic details of the IGF/crystal interfaces[34-39].

Validation of the simulations with available experiments is warranted for further application to other materials involving IGFs.

It has been found that rare earth (RE) ions can strongly improve the mechanical properties and grain growth behavior of Si_3N_4 ceramics[22,24,59,63-66]. Recent observations show RE ions preferentially take specific ordered locations, dependent upon the RE species, at the Si_3N_4 prism oriented surface, suggesting that RE location has a significant effect on properties[34-39,50,75,78,90,116]. However, the exact locations of the La ions on the prism surface differ slightly among the groups that have presented experimental data[75,78].

Our previous molecular dynamics (MD) simulations predicted network modifiers (Na or Ca) preferentially segregate into ordering sites at the IGF/crystal interfaces in alumina and silicon nitride systems[81,89,92-94,112-115,117]. These results implied similar segregation behavior in the case of RE ions due to their similar role as network modifiers in the silicate glass. This was subsequently observed in the HAADF-STEM studies[35-37,50] and recently verified in simulations of La in the IGF between the basal and prism oriented Si_3N_4 crystals [116,125].

In this work, we focus on the IGFs in silicon nitride sintered with La additives in a system more consistent with those observed experimentally: the prism oriented Si_3N_4 surface and an arbitrary high index Si_3N_4 surface, separated by IGFs with thickness different from those that had been previously simulated, enabling a more accurate comparison with the experimental data. Additional aims of this study are to provide atomistic details not readily available in experiments (e.g. the energetics and site filling

properties of the La ions), evaluate fracture, and gain further insights into the mechanisms controlling the La segregation behavior of the IGFs.

5.2 Computational Procedures

5.2.1 Two-body and Three-body Potentials

Amorphous intergranular films (~0.6 nm and ~1.8 nm thick) are simulated in lanthanum-silicate doped Si_3N_4 ceramics by using molecular dynamics simulations. The 0.6 nm IGF is consistent with the thickness observed in HAADF-STEM studies. A multi-body interatomic potential, consisting two-body and three-body terms, is employed similar to our previous calculations[89,93,116]. A modified Born-Mayer-Huggins (BMH) pair potential is used as the two body part for all ion-ion interactions and is given in the following equation.

$$V_{ij}^{BMH} = A_{ij}\exp\left(\frac{-r_{ij}}{\rho_{ij}}\right) + \frac{z_i z_j e^2}{r_{ij}} erfc\left(\frac{r_{ij}}{\beta_{ij}}\right) \qquad (5.1)$$

where r_{ij} is the separation distance between ion *i* and ion *j*, z_i and z_j are full ionic charges of ion *i* and ion *j*, and in this case +3, +4, -2, -3 for La, Si, O, N, *e* is the elementary charge, and *erfc* is the complementary error function. Parameters A_{ij}, ρ_{ij} and β_{ij} for specific pair type are listed in Table 5.1.

Table 5.1 Modified BMH and LJ pair potentials parameters

i-j pair	A_{ij} (fJ)	ρ_{ij} (pm)	β_{ij} (pm)	ε (fJ)	σ (pm)
O-O	0.0725	29	234	-	-
N-N	0.07241	29	220	-	-
Si-Si	0.1877	29	230	-	-
La-La	0.3975	45.1	230	-	-
N-O	0.1350	29	221	-	-
Si-La	0.3000	32	230	-	-
Si-O	0.2962	29	234	-	-
Si-N	0.7500	26.1	220	-	-
La-O	0.7377	31.75	270	-	-
La-N	3.9700	33.2	200	0.00395	195.6

Lennard-Jones (LJ) pair potential is added to this BMH potential in the two body part for La-N interaction and is given as

$$V_{ij}^{LJ} = 4\varepsilon\left[\left(\frac{\sigma}{r_{ij}}\right)^{12} - \left(\frac{\sigma}{r_{ij}}\right)^{6}\right] \qquad (5.2)$$

where r_{ij} is the separation distance between ion *i* and ion *j*. Parameters ε and σ are listed in Table 5.1.

The three-body part is given in the following equation.

$$V_{jik}^{3-body} = \lambda_{jik} \exp\left(\frac{\gamma_{ij}}{r_{ij} - r_{ij}^{0}} + \frac{\gamma_{ik}}{r_{ik} - r_{ik}^{0}}\right)\Omega_{jik} \qquad (5.3)$$

when $r_{ij} < r_{ij}^{0}$ and $r_{ik} < r_{ik}^{0}$. Otherwise, $V_{jik}^{3-body} = 0$. Its angular term is given by

$$\Omega_{jik} = (\cos\theta_{jik} - \cos\theta^0_{jik})^2 \qquad (5.4)$$

where θ_{jik} is the angle formed by ion *j*, ion *i* at its vertex, and ion *k*. The three-body potential is centered only on Si, O, and N ions. Parameters for the three-body potential are given in Table 5.2.

Table 5.2 Three-body potential parameters

j-i-k triplet	λ_{jik}(fJ)	γ_{ij}(pm)	γ_{ik}(pm)	r^0_{ij}(pm)	r^0_{ik}(pm)	θ^0_{jik}(deg)
Si/La-O-Si/La	0.001	200	200	260	260	109.5
Si-N-Si	0.035	260	260	280	280	120
O/N-Si-O/N	0.024	280	280	300	300	109.5

5.2.2 System Design and IGF Compositions

A schematic of three-dimensional system containing an IGF between a prism-oriented β-Si_3N_4 crystal and an opposing β-Si_3N_4 crystal as shown in Figure 5.1 (a). The opposing crystals include a basal-oriented crystal as well as two arbitrary differently misaligned crystals, the latter exposing two arbitrary high-index β-Si_3N_4 crystal orientations, one near $\left(614\bar{2}0\bar{1}\right)$ and another near $\left(\bar{7}10\bar{3}3\right)$. However, since the simulation results of the systems with each of these misaligned crystals are similar, we only present the results from using the near $\left(614\bar{2}0\bar{1}\right)$, which we will label as "high index" in the rest of this paper. The use of the basal-oriented crystal is included as the opposing crystal in order to compare the current results with the 0.6 nm IGF used here

with earlier work using thicker IGFs. Periodic boundary conditions are applied in all dimensions. A 0.6 nm glassy silicon nitride shell is added to the opposing β-Si_3N_4 crystal for simplicity in order to apply periodic boundary conditions in x and y (Figure 5.1 (a)), specifically for the high-index crystals where periodicity of the prism-oriented and misaligned crystal is difficult. The shell was also used for the basal crystal. This glassy nitride shell is made via a melt/quench process using only the bottom portion of Figure 5.1 (a), in which only the ions in the shell are mobile. This system was then added to the prism-oriented crystal, followed by inclusion of the IGF atoms.

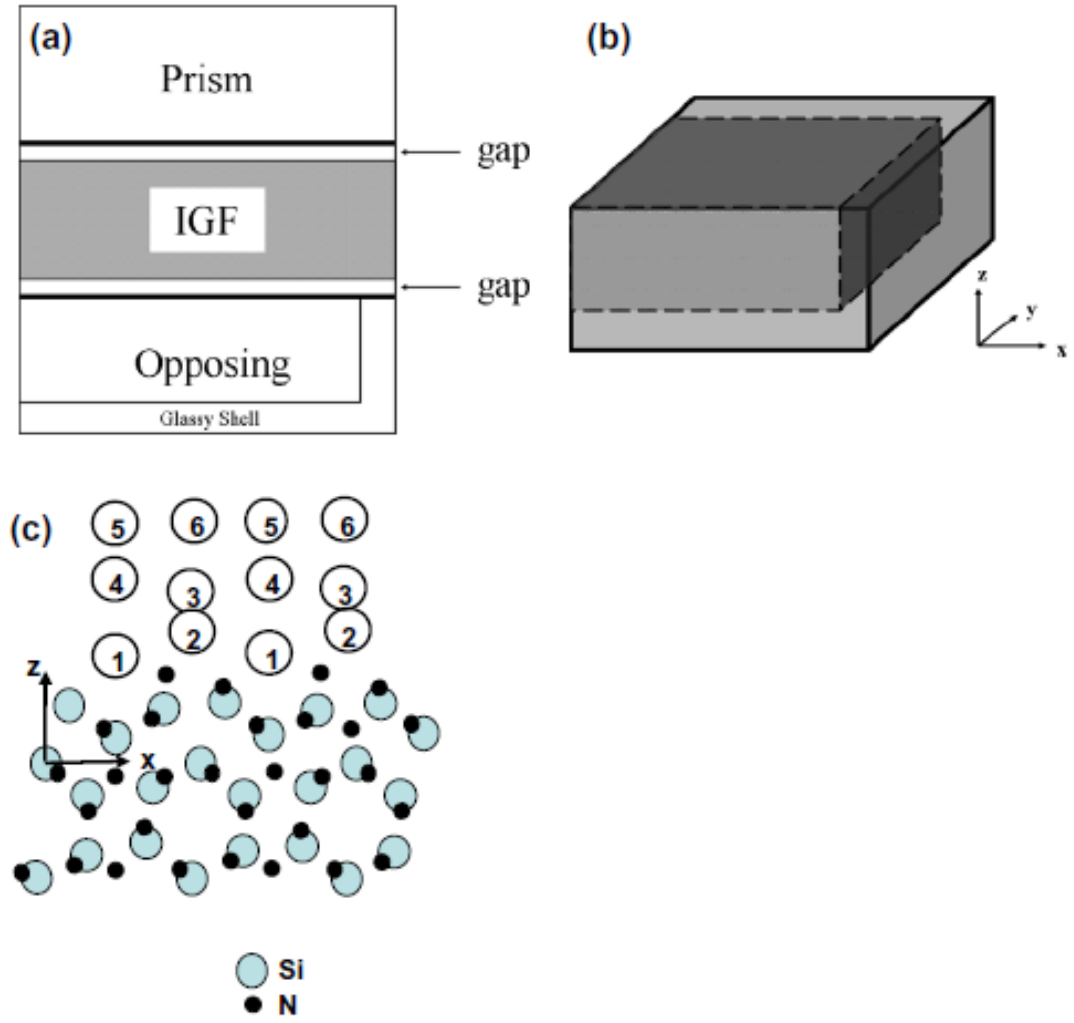

Figure 5.1 (a) Drawing of the simulation system with IGF between prism oriented and high index oriented β-Si_3N_4 crystals. Before the melt quench, a 3Å gap is left between the IGF and each crystal as a starting configuration. (b) Drawing of the high index oriented β-Si_3N_4 crystal surrounded by glassy nitride. (c) Diagram for site nomenclature of site 1, 2, 3, 4 after Winkelman et al.[37] and sites 5, 6 in this paper.

There are 4410 atoms in the prism crystal and about 4069 atoms in the opposing crystal and its shell, each with dimensions of about 53Å×52Å×16Å. Around 4800 and

1600 atoms are randomly distributed to form the ~1.8 nm and ~0.6 nm thick IGFs. A melt-and-quench process is then used to create the glassy IGF, as shown in Table 5.3. Two reflecting boundaries are applied accordingly in z at the crystal interfaces at high temperature and 2 Å away from the crystal interface into the crystals at low temperatures in order to prevent atoms from the IGF migrating into the crystals.

Table 5.3 Melt-quench process

Temperature	Conditions	Duration
300K	NVE, crystal frozen, reflecting boundary at crystal surface	10 ps
10,000K	NVE, crystal frozen, reflecting boundary at crystal surface	20 ps
9000K	x,y constant, P_z = 4 GPa, crystal frozen, reflecting boundary at crystal surface	1000 ps
8000K	As above	1000 ps
7000K	As above	1000 ps
6000K	As above	1000 ps
5000K	As above	1000 ps
4000K	As above	1000 ps
3000K	x,y constant, P_z = 4 GPa, crystal de-frozen, reflecting boundary at 2 Å below each crystal surface	1000 ps
2000K	NpT, p = 0.1 MPa, reflecting boundary at 2 Å below each crystal surface	200 ps
1000K	As above	20 ps
300K	As above	40 ps

The IGF compositions (3%, 6%, 9% La and 15%, 30% N/(N+O)) are given in Tables 5.4 and 5.5. While N contents in the 30% range within the IGF have been discussed in literature, no value for the La concentration in the IGF has been given. Although Winkelman et al. give the overall bulk compositions, there are known to be different from the values within the IGFs. The range of composition allows for the compositional variations that must locally occur due to the kinetics that occur during processing at various two-grain junctions.

The energy of the La ions as a function of z-location in the system is calculated from the total potential energy of the La ions averaged over the final 40 ps at 300K.

Table 5.4 Compositions of ~1.8 nm thick IGFs

Sample	La	Si	O	N	Total	La/Total	N/(N+O)
15N3La	144	1558	2636	464	4802	3%	15%
30N3La	144	1632	2118	908	4802	3%	30%
15N6La	288	1437	2616	460	4801	6%	15%
30N6La	288	1510	2102	900	4800	6%	30%
15N9La	432	1320	2598	460	4810	9%	15%
30N9La	432	1391	2086	896	4805	9%	30%

Table 5.5 Compositions of ~0.6 nm thick IGFs

Sample	La	Si	O	N	Total	La/Total	N/(N+O)
15N3La	48	522	882	156	1608	3%	15%
30N3La	48	546	708	304	1606	3%	30%
15N6La	96	482	874	156	1608	6%	15%
30N6La	96	503	700	300	1599	6%	30%
15N9La	144	437	862	152	1595	9%	15%
30N9La	144	460	692	296	1592	9%	30%

5.2.3 Fracture the System

Fracture behavior at 300K is evaluated by straining the system in the z dimension (perpendicular to the IGF-crystal interfaces) at a strain rate of 1×10^{-3} ps^{-1}, in which the system is uniformly strained, then allowed to relax for 100 timesteps during which the stress tensor normal to the interfaces, σ_{zz}, is calculated using

$$\sigma_{zz} = \frac{1}{V}\left(\sum_{i=1}^{N} m_i v_i^z v_i^z\right) + \sum_{i=2}^{N}\sum_{j=1}^{i-1} F_{ij}^z \bullet z_{ij} \qquad (5.5)$$

where V is the system volume, N is the number of mobile atoms, mi is the mass of atom I, v is the z-component of the velocity of atom I, F is the z-component of the force on atom I, and z is the separation distance of the z coordinates of atoms I and j(zj-zi). Reiteration of the strain and relaxation occurred until beyond fracture. The time step is 1fs.

5.2.4 La Adsorption Sites

The locations of the La ions at various adsorption sites on the prism-oriented surface will be described by the site nomenclature presented by Winkelman et al. for sites 1-4, redrawn in Figure 5.1 (c), with added sites 5 and 6 inferred from HAADF-STEM images of La ions at triple points from the same Ref. Site 5 and 6 are unlabeled by Winkelman et al., but are slightly visible in their images of the pockets, although without chemical verification. (Note, our z direction is equivalent to their y direction.) Sites 1 and 2 are separated by ~0.04 nm in z and appear as a broad peak in a density profile. Site 1 and 2 would be considered as the first and second ordered layers, while site 3 and 4 are combined as the third ordered layer and sites 5 and 6 as a possible fourth ordered layer.

Sites 1 and 2 are observed in the work by Shibata et al. (but labeled B and A, respectively, in their work) at slightly different locations than in the Winkelman et al.'s work, with somewhat different densities in comparison to the Winkelman data. As previously discussed with regard to La adsorption, differences among the different groups may be due to different instrumentation since the samples were from the same material. The work presented here will be compared to the Oxford data (Winkelman et al.) because of additional experiments there that gave the same results as shown by Winkelman et al., as discussed by Dwyer et al.

The coverage or saturation of the adsorption sites by La is determined as the number of La in a particular site divided by the number of available such sites.

5.3 Results and Discussion

5.3.1 Thickness Effect

Figure 5.2 shows that, similar to previous work[116,125], La ions preferentially segregate to the crystal surfaces in the 1.8 nm IGF between prism and basal silicon nitride crystals and that adsorption at sites 1 and 2 on the prism surface occurs for both the 1.8 and 0.6 nm IGFs, although with more site-filling in the thicker film than the thinner one due to the higher total number of La ions in a thicker film than a thinner one. La ions at sites 1, 2, 3 and 4 are observed in 15N6La, 15N9La, 30N6La (as shown in Figure 2 (a)), and 30N9La. These sites are consistent with HAADF-STEM results[37]. An interesting feature seen in Figure 5.2 is the loss of the glassy silicon nitride shell that was originally put around the opposing (basal) crystal. During the melt/quench of these shell atoms to make the glassy nitride shell, the ions attached to the opposing crystal in the x and y directions, causing growth of the basal crystal out to the periodic boundaries. (As will be seen later in Figure 5.3, which depicts the misaligned crystal, this crystal growth does not occur and the glassy nitride shell remains.)

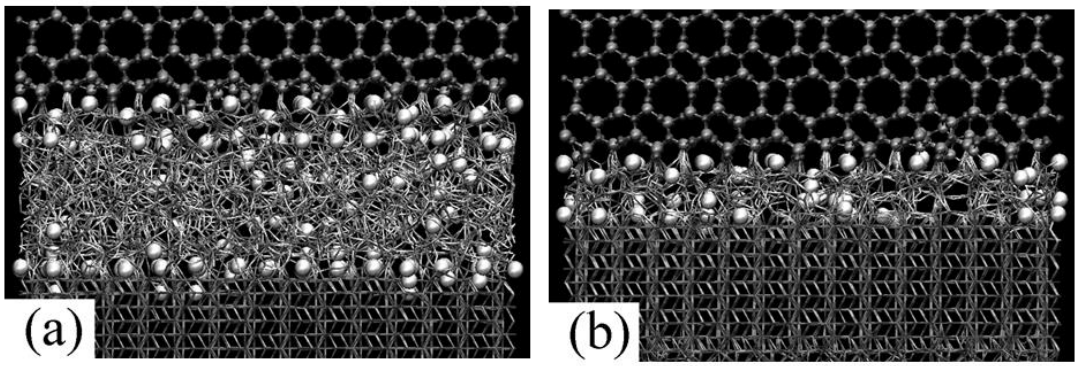

Figure 5.2 Snapshots of the final configuration of our MD simulations, which contains a 30N6La IGF (about 5.2 nm thick in y) in contact with a prism oriented

silicon nitride crystal on the top and a basal oriented silicon nitride crystal at the bottom with different thickness (a) ~1.8 nm thick, (b) ~0.6 nm thick. For clean view, only Si (big grey spheres) and N ions (small grey spheres) from the prism and La ions (big white spheres) are shown in spheres here. Bonds are drawn with cutoff distance of 2 Å.

The 1.8 nm IGF between prism and high index silicon nitride crystals in the current work (Figure 5.3) shows the same La locations on the prism surface and similar preferential segregation behavior in Figure 5.3 (a) and (c) as seen in our previous work of the 1.8 nm IGF between prism and basal crystals[116,125], indicating that the nature of the opposing crystal orientation does not affect segregation to the prism surface. La ions at site 1 and 2 are still observed for almost all the compositions in Table 5.4. La segregation at site 1, 2, 3 and 4 are again observed for the 6% La and 9% La at both 15% and 30% N/(N+O). Therefore, the presence of a highly different opposing interface does not change the site adsorption of La ions onto the prism surface in the 1.8 nm thick IGF.

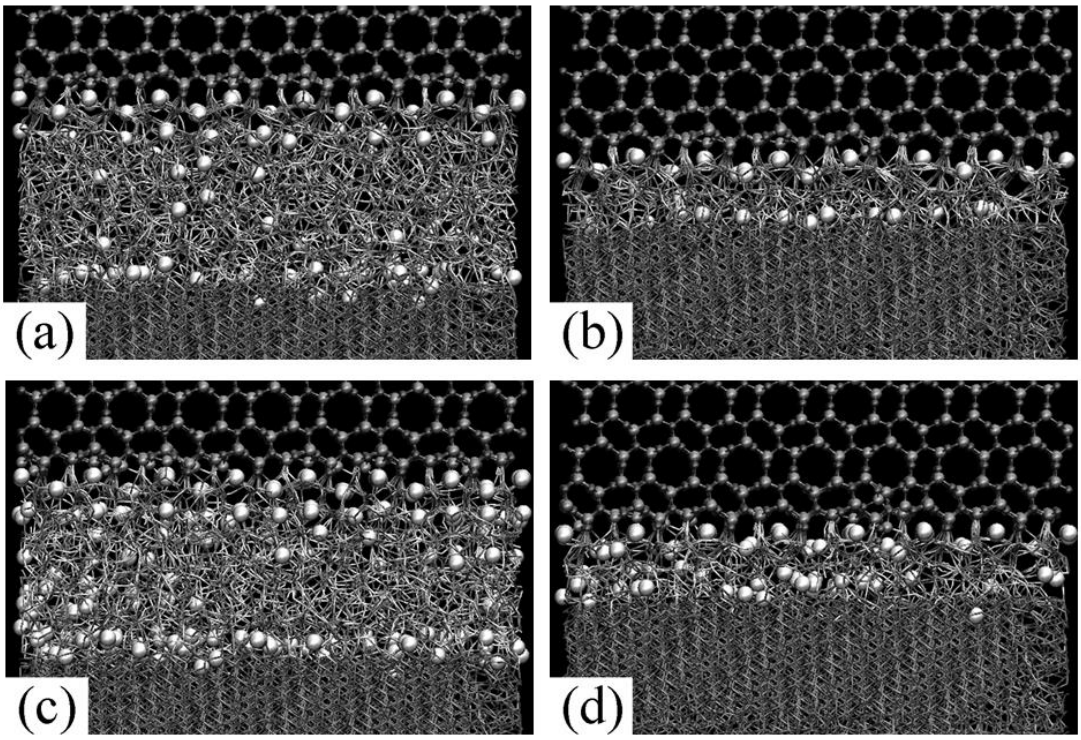

Figure 5.3 Snapshots of the final configuration of our MD simulations, containing an IGF (about 5.2 nm thick in y) between a prism and a high index [31-41] oriented silicon nitride crystal for various thicknesses and compositions (a) ~1.8 nm 30N3La, (b) ~0.6 nm 30N3La, (c) ~1.8 nm 30N6La, (d) ~0.6 nm 30N6La. Here, the drawings of the atoms and bonds are same as listed in Figure 2.

The 0.6 nm IGF inherits and loses features from the 1.8 nm IGF, as seen in Figure 5.3 (b) and (d). In the 0.6 nm IGF, La ions again prefer to segregate to both crystal surfaces, and sit at sites 1 and 2 on the prism surface for almost all the compositions in Table 5.5, as shown in Figure 5.2 (b) and Figure 5.3 (b) and (d). However, La at sites 3 and 4 are rarely seen in the 0.6 nm IGF. This could be attributed to the fact that there is the same number of La adsorption sites on the prism surface for both 1.8 nm and 0.6 nm

IGF, (same surface area in each) but far fewer La ions available in the 0.6 nm IGF versus the 1.8 nm IGF, as shown in Table 5.5 versus Table 5.4. In our previous work[116,125], the difference between 3%La (site 1, 2), 6%La (site 1, 2, 3, 4) and 9%La (site 1, 2, 3, 4, 5, 6) in the 1.8 nm IGF was obvious just by looking at the images. This simple visualization would have important implications in HAADF-STEM where the observation of different site order implies a concentration of La in the IGF. La adsorption onto sites 1, 2, 3, and 4 are clearly seen in the HAADF-STEM work by Winkelman et al (their figure 2a), but because of the thickness of their IGF sites 5 and 6 are not seen [37]. Due to the lack of La adsorption onto sites 3 and 4 in the 0.6 nm IGF, it becomes hard to distinguish the 3% La system from that of 6% La or 9% La by just looking at the images. Therefore, the separation distance between the crystal surfaces would affect this ordering and visualization.

The distances in z between site 1 and site 3 or 4 in our simulations is 0.37 ± 0.03 nm, which is similar to Winkelman *et al.'s*[37] HAADF-STEM result 0.32 ± 0.08 nm, and the distance between site 1 and site 5 or 6 is 0.58 ± 0.02 nm, making the latter sites impinge on the opposing crystal in the 0.6 nm IGF. The distance between the opposing high index crystal and its adsorption sites is 0.14 ± 0.02 nm in z. It is worthwhile mentioning that the sites 1, 2, 3 and 4 on the prism surface potentially exist in the 0.6 nm IGF, and it is the presence of the opposing crystal surface (with some sort of adsorption on its surface) that disrupts such a continuous ordering from the prism surface at ~0.6 nm IGF thickness. Due to the proximity of the opposing high index crystal, whether a basal crystal or a high-index crystal, it is impossible to see sites 5 and 6 in the 0.6 nm IGF. The locations of sites 3 and 4 overlap with the adsorption sites on the high index crystal

surface, making their presence in this thin IGF indeterminable. The overlap of ordered layers on both crystal surfaces is very important, and will be discussed in the upcoming paragraphs.

5.3.2 La Saturation Percentage

For both 1.8 nm and 0.6 nm IGFs, at constant N content, La adsorption onto surface adsorption sites increases as La content increases. Although the segregation behavior of 1.8 nm and 0.6 nm IGFs shows similarities, the segregation results have to be different because of the different number of ions available within the different thickness IGFs. Except for some sites in the 15N3La and 30N3La ~1.8 nm IGF, IGFs have most of their La adsorption sites filled more than 50% (high site saturation or coverage) as shown in Figure 5.4 (a). Figure 5.4 (b) shows that, apart from site 1, the 0.6 nm IGF has almost all its sites filled less than 50% (low site saturation). As is mentioned above, the low site saturation in the 0.6 nm IGFs can be attributed to the same number of sites available in both 1.8 nm and 0.6 nm IGFs, but different number of La ions available within the IGF. Because of the low La saturation of the interface sites, columns of sites 3 and 4 are not found in the 0.6 nm IGFs. Only a few La ions are found sitting around sites 3 or 4. More interestingly, the number of N ions in the ~1.8 nm IGF is three times more than that in the 0.6 nm IGF. Because of the differential binding energy (DBE) of La to N vs O in comparison to Si binding to those anions[90], La will segregate to the region of higher N density, such as the crystal surfaces. However, an increased number of N in the IGF allows for more La ions to remain in the interior of the IGF. Alternatively, the La ions drawn to the interface because of the high N concentration on the crystal surfaces can attract N from the IGF towards the interface to provide more La-N binding (vs. La-O),

enabling a synergistic effect that allows for more ordered layers of the La sites away from the interface. The relatively small number of N ions in the 0.6 nm IGF allow for La filling at site 1, but much lower La site filling at sites farther into the IGF, as shown in Figure 5.4 (b).

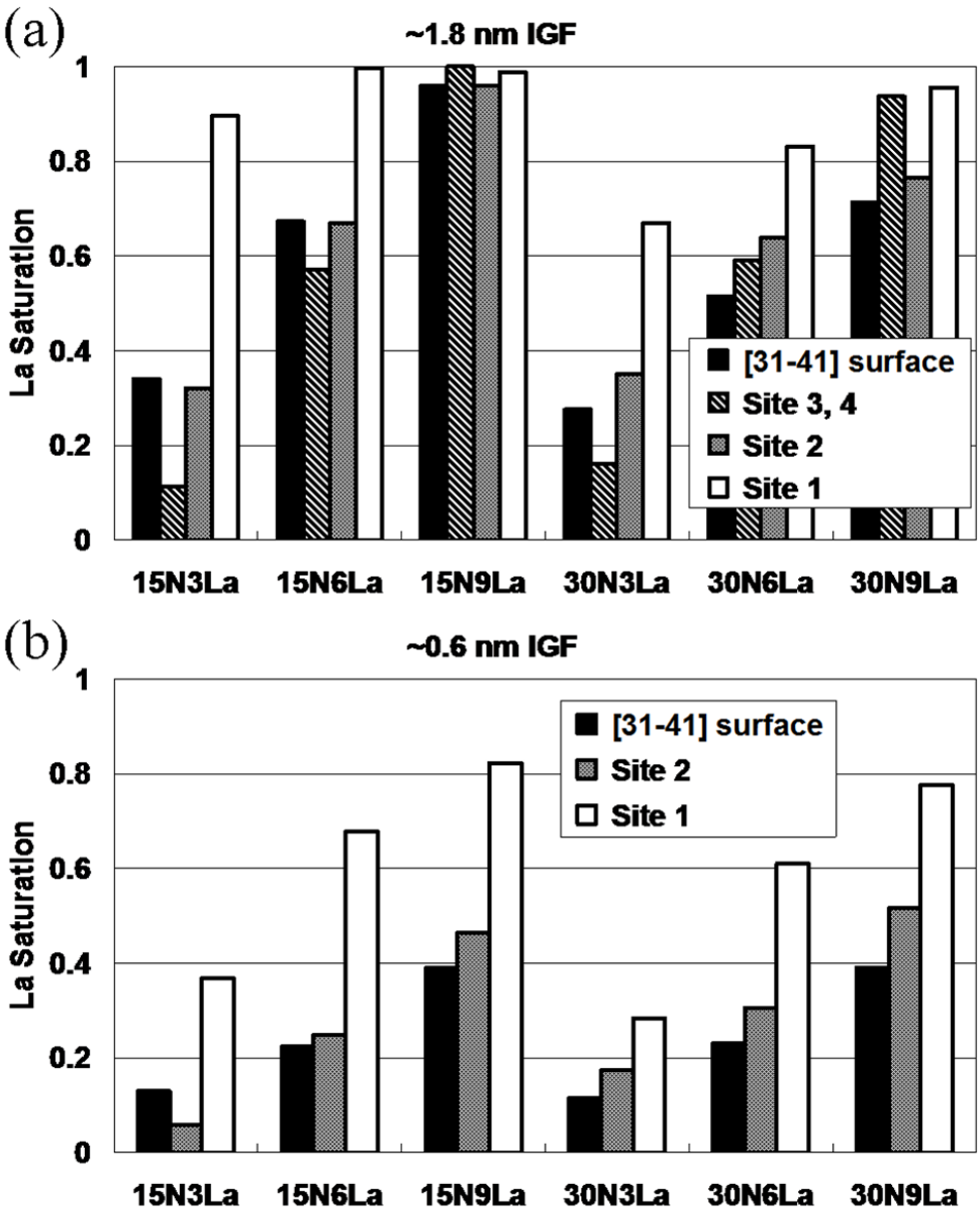

Figure 5.4 Comparison of La saturation percentage at various locations (La at site 1, 2, 3, 4 on the prism interface or on the [31-41] high index surface) for (a) ~1.8 nm

IGF and (b) ~0.6 nm IGF of various compositions. These charts are derived by using the La density at a specific site or surface for a specific composition to divide the maximum La density at that location among all the compositions.

5.3.3 Energy of La Ions According To Z

Figure 5.5 shows the potential energy of La ions according to their location in z and the corresponding La number density (the latter multiplied by 10 to fit on the same graph). The energy of La ions according to z is calculated from all interactions out to the cut-off distance. A large energy difference between La ions in the IGF interior and interfacial La ions is observed in 1.8 nm 15N6La IGF (Figure 5.5 (a)). This difference provides a driving force for La segregation to the interface (confirmed from the La density (black peaks)). There is little difference between the energy of the interior portion and that of the interfacial portion for 30% N/(N+O) in the thicker IGF (Figure 5.5 (c)), causing partial La presence in the interior IGF. The 0.6 nm IGF do not have such a big energy driving force (Figure 5.5 (b), (d)). More importantly, there is clearly weaker bonding of La ions in the 0.6 nm IGF than that of the 1.8 nm IGF, indicating less strong bonding for La at all sites in the 0.6nm IGF in comparison to the 1.8 nm IGF. (A similar weakening of the La bonding in the 0.6 nm IGF between a basal-oriented and prism-oriented system was also observed, but will not be discussed here: such an interface combination is not seen in experimental images but nonetheless shows the general effect of thickness on La bond interactions.) The implication is that the close proximity of the opposing crystal surfaces affects the number of N and La ions in the IGF which affects the energetics of the La ions in the IGF and at the surface sites. This bond-weakening implies a lower driving force for La to enter (or remain) in the very thin IGFs. An

important implication is that after La ions segregate to the crystal surface, depleting the IGF, additional La ions from the triple point would be less likely to migrate to the IGF because of the weaker cohesive energy of the La in a thin (0.6 nm) IGF vs. thicker pocket. However, competing with this is the fact that a lower N concentration in a thicker IGF shows low La binding energy (even lower than that in a thin IGF). The implication is that if a triple point has low N concentration, La ions in the triple point would readily migrate into the IGF that has more N present, regardless of the IGF thickness.

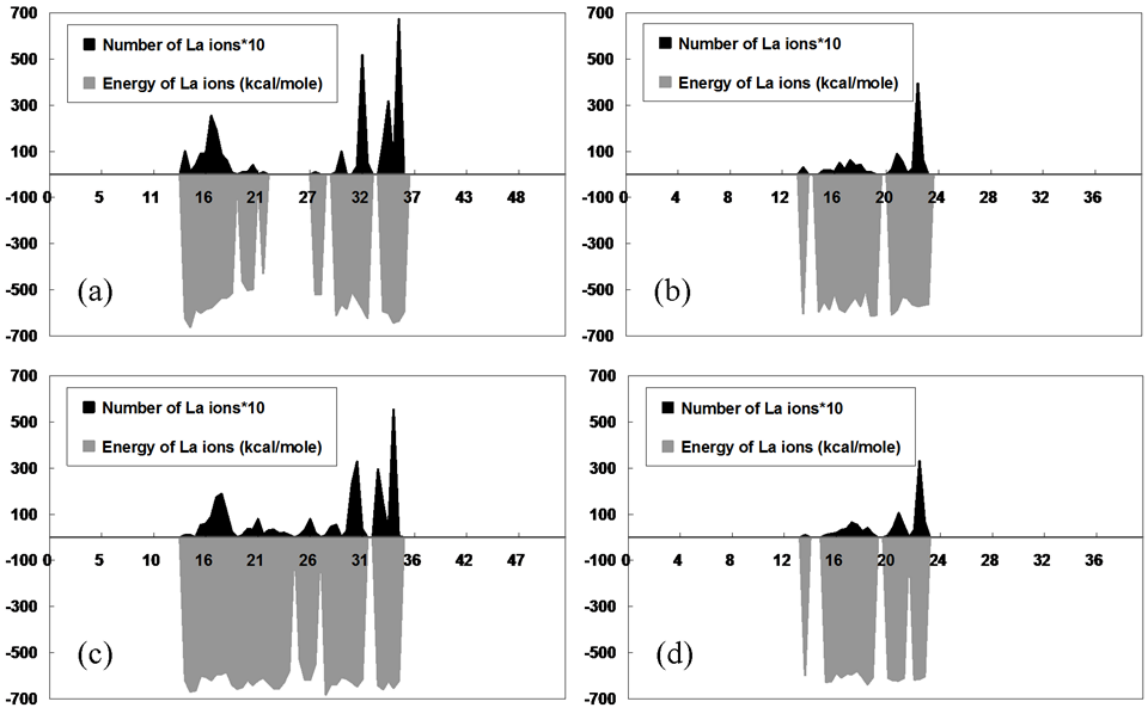

Figure 5.5 Chart of averaged number of La ions according to La locations in z (areas in black) and energy of La ions according to z (areas in grey) for (a) ~1.8 nm 15N6La, (b) ~0.6 nm 15N6La, (c) ~1.8 nm 30N6La, (d) ~0.6 nm 30N6La IGF.

5.3.4 Fracture Strength and Stress-Strain Curve

As La content is increased from 3%, to 6%, to 9%, increasing strength (highest peak on the stress-stress curve) is observed in Figure 5.6 (b, c, d). This shows that adding La dopants on improving the strength of silicon nitride ceramics. Similar to previous works[114], the strength of the material is increased greatly from about 15 GPa to about 25 GPa as N increases from 15% (about 460 N ions) to 30% (about 900 N ions) in the 1.8 nm IGF. However, in the 0.6 nm IGF, the effect of improved strength is no longer obvious due to the limited number of N ions (about 150 for 15% N/(N+O) and about 300 for 30% N/(N+O)) in the IGF.

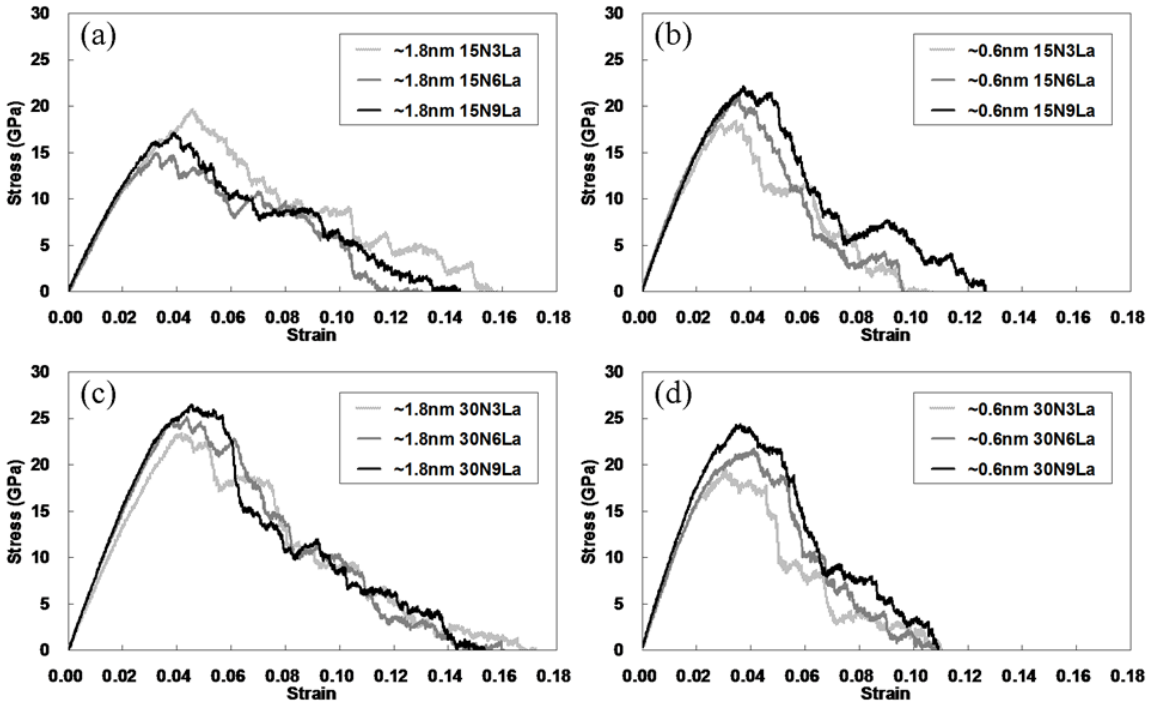

Figure 5.6 Stress-strain curves for 3% La, 6% La and 9% La in (a) ~1.8 nm IGFs at 15% N/(N+O), (b) ~0.6 nm IGFs at 15% N/(N+O), (c) ~1.8 nm IGFs at 30% N/(N+O), (d) ~0.6 nm IGFs at 30% N/(N+O) between prism and [31-41] high index silicon nitride crystals.

By comparing the strength of the 1.8 nm and 0.6 nm IGFs for the same composition, the thinner IGF is no longer stronger than the thicker IGF, but varies depending upon the concentration of N in the IGF. This is contrary to the strength enhancement in thinner (1nm) IGFs made of pure SiO_2 in comparison to 2 nm SiO_2 IGFs[126], which was attributed to the role of the six-membered rings in silica and the similar orientation of the two basal-oriented nitride crystals which imposed ordering across the interface. The latter also strongly influenced the results of the calcium silicate IGFs[95]. The data currently presented is more realistic because of the dissimilar orientations of the opposing crystal surfaces. In addition, the additive ions (N and La) and DBE of La play an important role in modifying fracture.

Figure 5.6 (a) shows higher strength of sample 15N3La compared to samples 15N6La and 15N9La, which is different from the general trend of increasing La, resulting in increased strength. Firstly, due to the stronger DBE mentioned above, as La ions segregate to the crystal surfaces, N ions in the IGF would follow these La ions to the interfaces (on the glassy IGF side of the adsorbed La ions). At constant N content (15% N/(N+O)), sample 15N6La and 15N9La contain a sufficient number of La ions to fill the multiple ordered layers on the crystal surface, which would cause most of the N ions in the IGF to segregate to the interface. However, 15N3La does not contain enough La ions to fill the first two adsorption sites. Therefore, fewer N ions segregate to the interfaces in the 15N3La, leaving more N ions in the interior of the IGF. With more N remaining in the IGF, the strength is increased. Therefore, the larger number of N ions left in sample 15N3a than in sample 15N6La and 15N9La would cause higher-strength IGFs. This is a very important point in that it indicates that RE segregation to the interface affects the

distribution of N in the IGF, which also has an effect on strength. Secondly, both the 1.8 nm and 0.6 nm IGF break at the glassy portion of the IGF as shown in Figure 5.7, not at ordered layers of sites 1, 2, 3 and 4 on the prism surface or along the high index crystal interface. This is consistent with the experimental data for intergranular fracture observed by Satet et al. of La-doped silicon nitride.

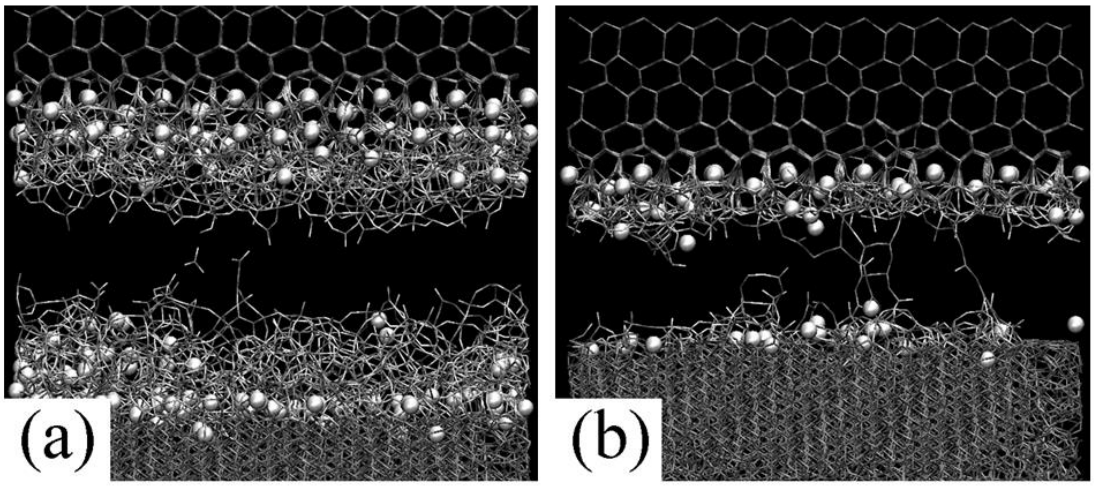

Figure 5.7 Snapshots after fracture of (a) ~1.8 nm, (b) ~0.6 nm 30N6La IGF between prism and [31-41] high index silicon nitride crystals.

The stress maxima in Figure 5.6 (a) are found to be far lower than those shown in Figure 5.6 (b, c, d). A similar trend is also observed in the systems that contained the other high-index surface (not shown here), so the behavior shown in Figure 5.6 (a) is not an anomaly. N follows La to the interface, as discussed above, thus removing N from the interior IGF. Without a sufficiently large number of N ions added to the interior IGF, too many N ions follow the La to the interface, leaving a weakened IGF where ruptures occur. Apparently, it seems that more N would stay in the 1.8 nm IGF than the 0.6 nm IGF,

because the number of N ions available in the 1.8 nm IGF is three times that in the 0.6 nm IGF at the same composition.

However, the density profiles in Figure 8 show more N in the interior of the 0.6 nm IGF (Figure 5.8 (b) and (d)) than that in interior of the 1.8 nm IGF with 15% N (a). Since the 0.6 nm IGF is so thin, the overlap of the ordering at the crystal interfaces leaves a lot of the interfacial N actually located in the interior IGF. Therefore, there is no effective depletion of N in the IGF interior.

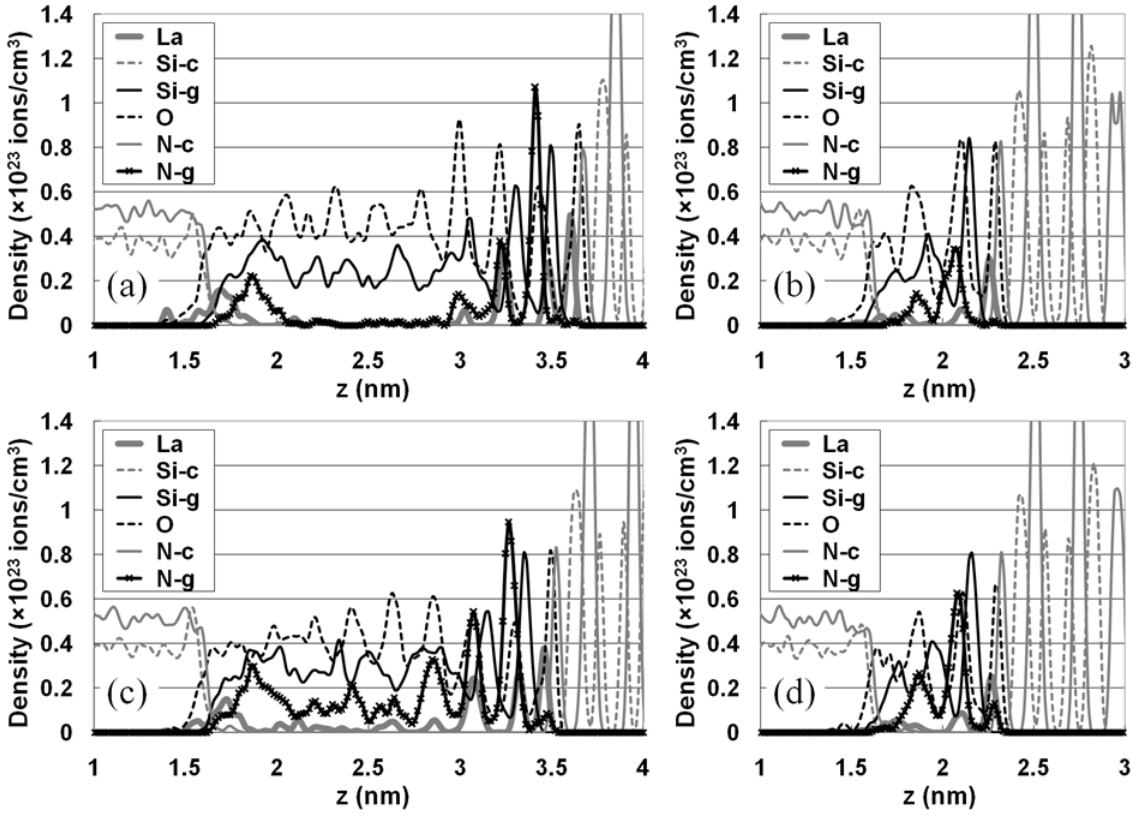

Figure 5.8 Density profiles of all species as a function of z, perpendicular to the IGF-crystal interfaces for (a) ~1.8 nm 15N6La, (b) ~0.6 nm 15N6La, (c) ~1.8 nm 30N6La, and (d) ~0.6 nm 30N6La. Only the regions near the IGF are shown. Si and N ions from the crystal are labeled Si-c and N-c, respectively; Si and N ions from the IGF are labeled Si-g and N-g, respectively.

Because La ions preferentially bind to N, they move to the N-rich prism crystal surface, filling sites in concert with the number of La available from the IGF, depleting the IGF interior of La. In addition, if there are sufficient N present in the IGF, these similarly follow the La to the interface to increase La-N coordination, which subsequently allows more La to move to these N in the interface region to create additional ordered sites moving outward from the interface. This behavior is highly dependent on the actually number of La and N in the IGF.

5.4 Conclusions

MD simulation results of La-Si-O-N intergranular films (IGFs) show La adsorption on the prism-oriented surface, precisely consistent with HAADF-STEM data by Winkelman et al. for 0.6 nm and thicker IGFs in silicon nitride. The simulations show that the type of opposing crystal, whether basal oriented of misaligned high-index oriented, does not alter the adsorption on the first two sites on the prism oriented surface, indicating the potentially ubiquitous nature of this ordering in this system. The amount of site-filling in sites 1 and 2 on the prism surface is affected by the number of La in the IGF, which is governed not only by composition, but also by IGF thickness. The extent of La ordering away from the interface is affected both by IGF thickness and by IGF composition.

The binding energies for La ions at different locations in the IGF vary as a function of composition and IGF thickness. Two effects, potentially competing, result from the evaluation of La binding energies: one is that after La segregation to the interface, additional La ions from the pocket would be less likely to migrate to a thin (0.6 nm) IGF because of the lower cohesive energy of the La there; the second is that a low N

concentration in a thick IGF results in a low La binding energy, implying that if a triple point (making it synonymous with a very thick film) has a low N concentration, La ions from the pocket are more weakly bonded and would readily migrate into the IGF that has more N present regardless of IGF thickness.

Adding La improves the strength of silicon nitride ceramics except in thicker IGFs with low N concentration (e.g. the 1.8 nm IGFs at 15% N/(N+O)). All of the 1.8 and 0.6 nm IGFs fractures in the glassy portion of the IGF, not inside the interfacially ordered crystal-like La-N/O layers. Such results imply intergranular fracture that is consistent with experimentally observed fracture.

Chapter 6 Role of oxygen on the adsorption sites of Lu and La in β-Si_3N_4

6.1 Introduction

Molecular dynamics (MD) simulations of oxides and nitrides predicted the segregation of network modifiers (alkali and alkaline earth additives) in the siliceous intergranular films (IGFs) to specific surfaces, affecting growth behavior consistent with the anisotropy seen experimentally[81,92,94,114]. In β-Si_3N_4, the modifier ions segregated to the prism surface, inhibiting growth[114] and causing anisotropic grain growth that significantly affects the mechanical properties[5,20,66,127]. Because of their larger size, rare earth (RE) ions act as network modifier ions in silicates, similar to smaller, but lower valence alkali and alkaline earth ions. At the extreme ends of RE cation sizes, La and Lu have significantly different effects on grain morphology and mechanical properties in β-Si_3N_4[20,127]. With added La, grains are highly anisotropic, enhancing fracture toughness, whereas with added Lu, grains are more uniform, although in both systems some grains showing the opposite growth behavior is observed. However, the mechanisms governing the different growth behaviors and resultant mechanical properties have eluded description from either experimental or ab-initio computational results other than the generic and unsatisfactory idea that it is due to a ‘weakened interface’[75].

Using HAADF-STEM, several groups observed the segregation of rare-earth ions to the prism-oriented β-Si_3N_4 surface of samples from the same source [35,36,128]. The adsorption sites for Lu differ from the locations for La [75]. A schematic drawing of the pristine β-Si_3N_4 prism surface is shown in figure 1. One set of data that most definitively shows the locations for RE adsorption on this surface is illustrated in Figure 1 (b) and (c)

for both Lu and La, respectively[128]. The cause for the different sites between La and Lu could not be fully explained. Ab-initio calculations reproduced the La adsorption at sites La1 and La2 as seen experimentally, but could not obtain Lu at site Lu1, only observing Lu close to site Lu1'[78].

Our MD simulations similarly reproduced the HAADF-STEM data for La at sites La1 and La2 (as well as the experimentally observed La3 and La4) [116,125]; however, initial attempts at reproducing the Lu sites Lu1 and Lu2 on a fully nitride (N in all anion surface sites) prism surface were unsuccessful until we studied the effect of oxygen on the location of Lu on the prism surface. The presence of O on N lattice sites near the surface was shown in EELS studies of an SiO_2 IGF on the prism β-Si_3N_4 surface[129] and should be expected in RE-doped IGFs[10,17]. As the simulations will show, the inclusion of O on certain lattice sites plays a significantly important role in Lu adsorption. Figure 6.1 (a) provides the nomenclature for the different surface N sites that are replaced by O on the $\left(10\bar{1}0\right)$ surface in the current work.

Here we report molecular dynamics simulations of the important effect of the location of oxygen ions on specific anion surface sites on the prism surface of β-Si_3N_4 on the adsorption sites of Lu and La ions that match HAADF-STEM results. These results can be used to explain the difference in adsorption sites between La and Lu observed in the experiments as well as provide the mechanism by which growth behavior differs as a result of these different additives.

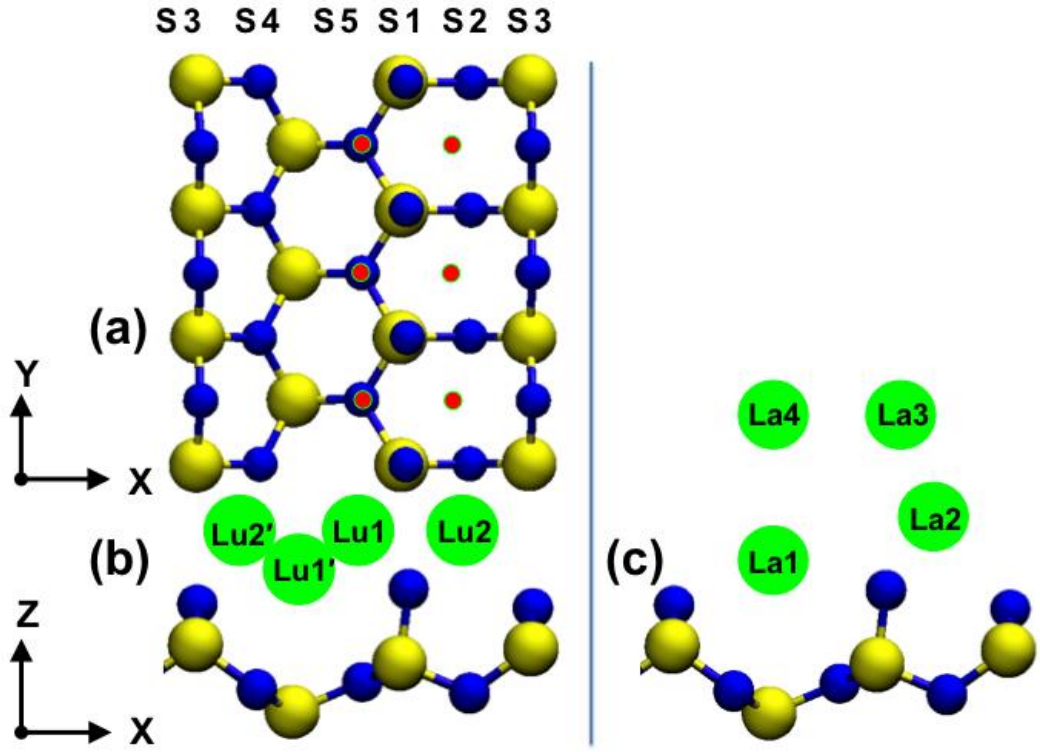

Figure 6.1 (a) Top view and (b, c) side view of the Si_3N_4 prism surface (N in blue spheres, Si in larger yellow spheres). Nitrogen sites are respectively labeled as S3, S4, S5, S1, S2, S3 along the x axis. The red dots in (a) indicate possible Lu1 and Lu2 sites. In (b) are shown Lu adsorption sites Lu1, Lu2, Lu1′ and Lu2′ (c) La adsorption sites La1, La2, La3 and La4 on the Si_3N_4 prism surface.

6.2 Computational Procedure

6.2.1 System Design with O termination

Similar to our previous approach[116,125,130], molecular dynamics computer simulations of RE-Si-O-N IGF's between a prism and an opposing high index crystal were performed. Unlike our previous research, different O replacements for N in the prism surface are made in this study for two IGF thicknesses (6Å and 18Å) and one

composition (6%RE, 30%N/N+O). In particular, this means the prism surface is designed with O at specific N lattice sites. For example, an S1 terminated surface refers to a silicon nitride prismatic surface with all the N ions at site S1 (shown in Figure 1a) replaced by O. The S1 terminated surface is also called prismatic surface with single replacement in this paper due to the fact that only one type of N surface site is replaced by O. Likewise, a surface with S1S2 termination refers to a prism surface with all the N ions at both site S1 and site S2 replaced by O. This S1S2 terminated surface is therefore called a prismatic surface with double replacement. In like manner, a prismatic surface with triple replacement would refer to a prism surface terminated by e. g. S1S2S3.

In this paper, the location of Lu and La is carefully investigated on the prism surface with different types of surface terminations. Manifestation of these surface site occupancies are given in density profiles of the rare earths as a function of distance perpendicular to the interface. Specific evaluation of the RE ions at these sites was made graphically in order to correctly label the density profiles with the occupancy of the specific sites. The energetics of adsorption sites for Lu ions were calculated for 2 conditions: one, with a fully nitride prism surface and two, for a prism surface with O replacing N at S1 sites and at a series of double replacement sites. This analysis was done with one Lu adsorbed at an Lu2 site while a second Lu ion was moved over the surface in 0.1Å increments in x and y to find the minimum energy at each location.

The final simulation box size in x, y, z is approximately 53.3 Å × 52.6 Å × 38 Å respectively, for the 6 Å IGF and 53.3 Å × 52.6 Å × 48 Å for the 18 Å IGF, with slight volume variations per sample due to the constant pressure nature of the runs. Around 1600 or 4800 atoms for the IGF are randomly distributed in the region between the prism

crystal (~4200 atoms) and high index crystal (4069 atoms). Periodic boundary conditions are applied in x and y. Two reflecting boundaries are applied accordingly in z at the crystal interface at high temperature and 2 Å away into the crystal interface at low temperatures in order to prevent atoms from the IGF migrating into the crystals.

A fast melt quench process is conducted with temperature profiles shown in Table 6.1. A lower mass of 40 amu is used for both Lu and La in the melt quench process in order to accelerate diffusion for Lu and La to enable faster sampling of appropriate sites. The z-location of the last Si layer in the Si_3N_4 prism surface is located at 21.2Å in all cases. The time step is 10^{-15} s.

Table 6.1 Melt-quench process

Temperature	Conditions	Duration
300K	NVE, crystal frozen	10 ps
10,000K	NVE, crystal frozen	20 ps
9000K	x,y constant, P_z = 4 GPa, crystal frozen	100 ps
8000K	As above	100 ps
7000K	As above	100 ps
6000K	As above	100 ps
5000K	As above	100 ps
4000K	As above	100 ps
3000K	As above	100 ps
2000K	NpT, p = 0.1 MPa, crystal de-frozen	20 ps
1000K	As above	20 ps
300K	As above	40 ps

6.2.2 Potential Development

The multi-body interatomic potential is employed, which is composed of a two-body and a three-body part. The two-body part is composed of Born-Mayer-Huggins (BMH) pair potential and either one of the two Lennard-Jones (LJ) pair potentials (12-6 or 9-6), as shown in the following equations.

$$V_{ij}^{2-body} = A_{ij} \exp\left(\frac{-r_{ij}}{\rho_{ij}}\right) + \frac{z_i z_j e^2}{r_{ij}} erfc\left(\frac{r_{ij}}{\beta_{ij}}\right) + V_{ij}^{LJ} \qquad (6.1)$$

$$V_{ij}^{LJ(12-6)} = 4\varepsilon\left[\left(\frac{\sigma}{r_{ij}}\right)^{12} - \left(\frac{\sigma}{r_{ij}}\right)^{6}\right] \qquad (6.2)$$

$$V_{ij}^{LJ(9-6)} = \frac{27}{4}\varepsilon\left[\left(\frac{\sigma}{r_{ij}}\right)^{9} - \left(\frac{\sigma}{r_{ij}}\right)^{6}\right] \qquad (6.3)$$

where r_{ij} is the separation distance between ion *i* and ion *j*, z_i and z_j are full ionic charges of ion *i* and ion *j*, and in this case +3, +4, -2, -3 for La, Si, O, N, *e* is the elementary charge, and *erfc* is the complementary error function. Parameters A_{ij}, ρ_{ij}, β_{ij}, ε, and σ for each pair type are listed in Table 6.2. The 9-6 Lennard-Jones pair potential (eq. 3) is selected for La potential set A and B and Lu potential set A, B, C, while the 12-6 Lennard-Jones pair potential (eq 2) is used for La potential set C.

In this work, three sets of two-body pair potentials (marked as RE potential set A, B, C in Table 2) were parameterized with different potential well depths (labeled bond strength in Table 2 and given in units of eV) for RE-O and RE-N based on the formation energy[131]. From the La potential set A, to B, to C, the La-O bond is stronger than, close to, and weaker than the La-N bond, respectively. For the Lu potential set A and B,

the Lu-O bond is stronger than the Lu-N bond. For the Lu potential set C, the Lu-O bond is weaker than the Lu-N bond. In all six cases, the crystalline forms of RE_2O_3 and REN were stable in constant pressure simulations. These variations on bond strengths were used to determine the implications of different values on the resultant Lu siteing on the crystal surfaces.

In this work, the La potential set C and the Lu potential set A represent the respective RE-O and RE-N bonds the best. The variations of the RE-O and RE-N bonds are provided in Table 6.2 for the following reasons. (i) A type of lanthanum-like cation with RE-O bond stronger than (or equal to) the RE-N bond could have been studied. Similarly, a lutetium-like cation with RE-O bond weaker than the RE-N bond could have been investigated. (ii) The variation on the reliability of the results could be evaluated by both weakening the Lu-O and Lu-N bonds from Lu potential set A to Lu potential set B. In other words, the question of whether the same adsorption sites will be obtained by changing the potential parameters slightly would have been addressed. It would be interesting to explore whether there exit La-related crystal structures such as LaSiO[132] or LaSiN[133] or LaSiON[134] or La4Si2O7N2[135] or Lu-related crystal structures such as Lu2SiO5 (LSO)[136-138] or Lu2Si2O7 (LPS)[139-142] or LuSiON[143].

Table 6.2 Two-body pair potential parameter sets

i-j pair	A_{ij}(fJ)	ρ_{ij}(Å)	β_{ij}(Å)	ε(fJ)	σ(Å)	LJ form	Strength (eV)
O-O	0.0725	0.29	2.34				
N-N	0.07241	0.29	2.20				
Si-Si	0.1877	0.29	2.30				

N-O	0.1350	0.29	2.21				
Si-O	0.2962	0.29	2.34				
Si-N	0.7500	0.261	2.2				
La-Si	0.3000	0.32	2.3				
La-La	0.3975	0.57	2.3				La potential set A
La-O	0.8000	0.34	2.5	0.0017	1.83	9-6	-10.74
La-N	3.3000	0.323	2.1	0.0024	1.99	9-6	-8.68
La-Si	0.3000	0.32	2.3				
La-La	0.3975	0.57	2.3				La potential set B
La-O	0.8000	0.34	2.5	0.0017	1.83	9-6	-10.74
La-N	3.5000	0.3276	2.0	0.0035	1.95	9-6	-10.87
La-Si	0.3000	0.32	2.3				
La-La	0.3975	0.451	2.3				La potential set C
La-O	0.7377	0.3175	2.7				-5.31
La-N	3.9700	0.332	2.0	0.00395	1.956	12-6	-8.19
Lu-Si	0.269	0.4795	2.3				
Lu-Lu	0.3975	0.455	2.3				Lu potential set A
Lu-O	1.57	0.293	2.33	0.002295	1.542	9-6	-10.11
Lu-N	1.95	0.2476	1.17	0.001685	1.82	9-6	-8.78
Lu-Si	0.3	0.32	2.3				
Lu-Lu	0.3975	0.29	2.3				Lu potential set B
Lu-O	6.0	0.2358	2.2	0.00236	1.419	9-6	-8.98
Lu-N	6.0	0.2369	2.2	0.000301	1.419	9-6	-6.53

Lu-Si	0.269	0.4795	2.3				
Lu-Lu	0.69	0.455	2.3				Lu potential set C
Lu-O	0.67	0.2526	1.419	0.001345	1.791	9-6	-8.88
Lu-N	1.5525	0.33	2.0	0.00292	1.78	9-6	-11.06

The three-body part is given in the following equation.

$$V_{jik}^{3-body} = \lambda_{jik} \exp\left(\frac{\gamma_{ij}}{r_{ij} - r_{ij}^0} + \frac{\gamma_{ik}}{r_{ik} - r_{ik}^0} \right) \Omega_{jik} \qquad (6.4)$$

when $r_{ij} < r_{ij}^0$ and $r_{ik} < r_{ik}^0$. Otherwise, $V_{jik}^{3-body} = 0$. Its angular term is given as

$$\Omega_{jik} = (\cos\theta_{jik} - \cos\theta_{jik}^0)^2 \qquad (6.5)$$

where θ_{jik} is the angle formed by ion *j*, ion *i* at its vertex, and ion *k*. The three-body potential is centered only on Si, O, and N ions with parameters given in Table 6.3.

Table 6.3 Three-body potential parameters

j-i-k triplet	λ_{jik}(fJ)	γ_{ij} (Å)	γ_{ik}(Å)	r^0_{ij}(Å)	r^0_{ik}(Å)	$\cos\theta^0_{jik}$
Si-O-Si / La-O-La / Lu-O-Lu	0.001	2.0	2.0	2.6	2.6	-0.3333
O-Si-O / N-Si-N	0.024	2.8	2.8	3.0	3.0	-0.3333
Si-N-Si	0.035	2.6	2.6	2.8	2.8	-0.5
La-N-La / Lu-N-Lu	0.001	2.0	2.0	2.6	2.6	-0.5

6.2.3 The Purpose of Simulation

In this paper, the La or Lu adsorption sites are investigated on various prismatic oxidized surfaces. In total, 312 samples are studied via molecular dynamics computer simulations with 26 prismatic surface terminations (including single, double and triple O replacements of N), 6 rare earth potential sets (i.e. La potential set A, B, C and Lu potential set A, B, C), and 2 film thicknesses (6 Å and 18 Å). The system was kept charge neutral by removing atoms from the bottom prism crystal plane that was far from the IGF and the reacting surfaces.

6.3 Results and Discussions

6.3.1 Density Profiles of Lu for Single Replacement

Results for the Lu adsorption site locations on the prism surface in the 18 Å IGFs are given in the RE-density profiles in Figure 6.2 for single replacement. Using Lu potential set A or B (Lu-O stronger than Lu-N), Figure 6.2 (a) and (b), respectively, show that Lu1 and Lu2 sites are not occupied with a pure nitride surface (labeled N in Figure 6.2), but are occupied when replacing N sites at S1 with O. Other single site replacements (S2-S5) show no site filling. Using Lu potential set C (Lu-O weaker than Lu-N), Figure 6.2 (c) shows that while both Lu1 and Lu2 sites are filled, there are too many Lu at site Lu1’ or Lu2’ compared to the intensities inferred from the HAADF-STEM results.

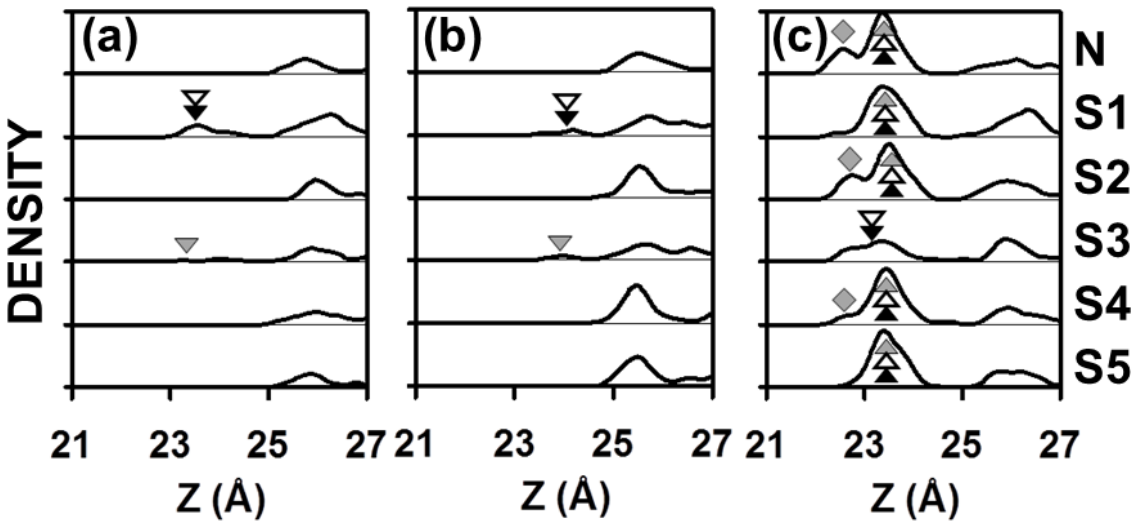

Figure 6.2 Density Profiles of Lu from a 18 Å IGF along the z axis on various prismatic surfaces with one site terminated by O, simulated by (a) Lu potential set A; (b) Lu potential set B; (c) Lu potential set C. S1 means all the S1 sites on the prismatic surface are terminated by O. N means all sites are terminated by N. Here, the empty triangle represents Lu1 site; dark triangle represents Lu2 site; gray diamond represents Lu1' site; gray triangle represents Lu2' site. Last Si layer in prism surface is at 20.6Å.

6.3.2 Density Profiles of Lu for Double Replacement

However, results are mixed with double site replacements. In Figure 6.3 (a) and (b), all double O replacement sites containing the S1 show that Lu sits almost exclusively at the correct sites Lu1 and Lu2 for both potential sets A and B. All other combinations of double replacement sites fail to show Lu at Lu1 and Lu2. Potential set C again shows excessive adsorption at most double O replacement sites, occupying both acceptable sites as well as sites not seen in the HAADF-STEM work. As will be discussed below,

replacing three N sites simultaneously leads to only the S1-related combinations giving correct Lu1 and Lu2 sites for potential sets A and B, and no acceptable sites for potential set C.

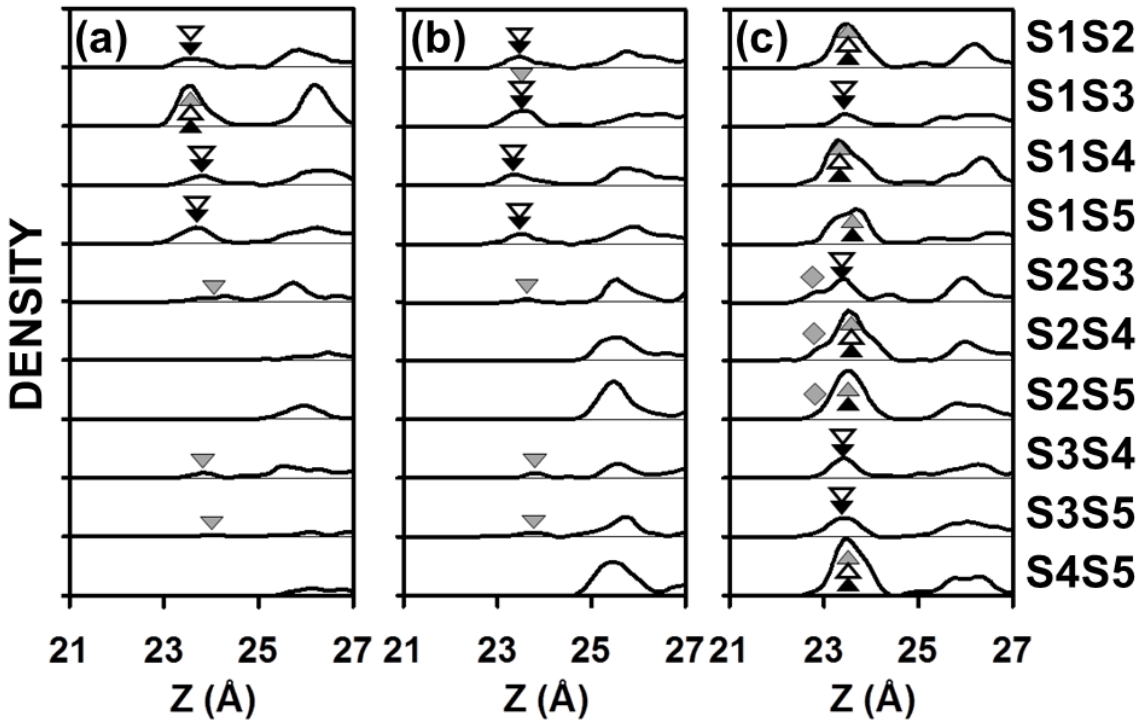

Figure 6.3 Density Profiles of Lu from a 18 Å IGF along the z axis on various prismatic surfaces with two sites terminated by O, simulated by (a) Lu potential set A; (b) Lu potential set B; (c) Lu potential set C. Markers same as in figure 2.

6.3.3 Energy Map and Adsorption Energies of Lu ion

A justification for the different adsorption behavior can be determined using data for site energetics. The red dots in Figure 6.1 (a) indicate possible adsorption sites Lu1 and Lu2 from the top view. However, previous HAADF-STEM data [37] showed that sites Lu1 and Lu2 are staggered in that they do not have the same y location. The

implication is that if one site is filled, the adjacent site with the same y dimension cannot be filled. This is observed in the simulations, but since the density profile in z does not delineate this difference, a plot of the interaction energy of Lu over the surface in the presence of a pre-adsorbed Lu was calculated.

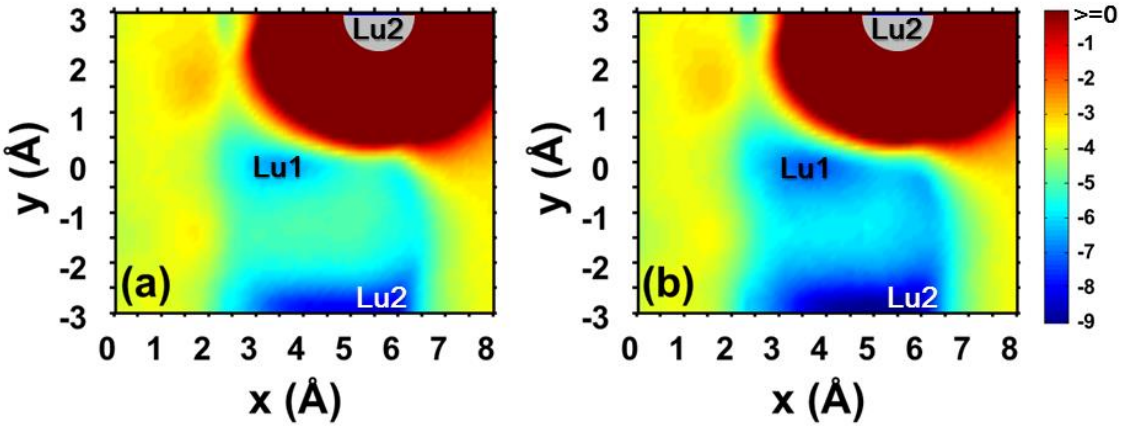

Figure 6.4 Energy map for Lu on the (a) pure N prism surface and (b) O at the S1 sites. Grey hemisphere at (5.5, 3) is one Lu at site Lu2 that is kept frozen, while a second Lu samples the rest of the adjacent surface sites. Site Lu1 is at (3.5, 0) and a second Lu2 site at (5.5, -3). Color bar gives Lu energy in eV. See text for further details.

The energy distribution for Lu adsorption onto the N-terminated prism surface versus the S1 O-terminated is shown in Figure 6.4. (Additional results for double replacement surfaces gave results similar to the S1 figure shown here.) The surface atoms and one Lu at the Lu2 site given in grey in the figure are kept frozen while a second Lu samples the surface.

As shown in Figure 6.4, the second Lu samples a repulsive region surrounding the pre-adsorbed Lu at the Lu2 site (all energies greater than zero were set to zero so that the color bar could be more clear). This repulsive region prevents the second Lu from adsorbing at the Lu1 site at the same y dimension as the occupied Lu2 site (see red dots in Figure 6.1 (a)).

The next possible Lu adsorption site would be displaced in y to the second row of red dots in figure 1a. Figure 6.4 (a) shows a well only near (3.5, 0), which is a Lu1 site, indicating both the staggered nature of the siteing and also the lack of another Lu2 site along the same y location (x, 0). The next site would be near (5.5, -3), which is the next available Lu2 site. This lower y-location adsorption site is broader in x because it encompasses both Lu2 and Lu1, but our data shows Lu2 is a deeper well than Lu1, although the color scheme does not show this difference sufficiently well.

However, the adsorption energies at these different sites are given in Table 4. A Lu sampling this ~(x, -3) location would naturally fall into the Lu2 site rather than the Lu1 site because our simulations show that there is essentially no barrier between the sites. These results also show that the adsorption energies at sites on the N-terminated prism surface are clearly weaker than on the O-terminated surface for the S1 and S1-related double replacement sites.

Table 6.4 Adsorption energies of Lu ion at Lu1 and Lu2 sites on differently terminated prism surfaces. (Site locations are approximate, but coincide with Figure 6.4.)

Site Location	Lu1 ~(3.5, 0)	Lu2 ~(5.5, -3)
Surface	Energy (eV)	Energy (eV)
Pure N	-6.5763	-8.3644
S1	-7.2506	-9.0565
S1S2	-6.9504	-9.1226
S1S3	-6.9236	-9.3944
S1S4	-6.9481	-9.0297
S1S5	-7.0798	-9.0673

Therefore, the data show that the adsorption sites are staggered, consistent with HAADF-STEM [37]. A Lu at Lu2 prevents another Lu at the Lu1 site along the same y dimension. However, since these data come from single Lu ions sampling the prism surfaces in vacuum, the specific energies are not exactly the same as sampling a surface in the presence of the IGF. However, the data do show the staggered nature of the adsorption sites as well as a difference between the nitride surface and an oxidized one.

6.3.4 Density Profiles of Lu in 6 Å IGF

Considering such results and the data in Figures 6.2 and 6.3, it is clear that the presence of O in single replacement sites other than S1 is not sufficient for the correct Lu adsorption and O in S1 allows for an improvement in adsorption. With multiple surface N site replacements in conjunction with S1 (i.e. double and triple replacement), Lu siteing

in Lu1 and Lu2 increases. The implication is that the experimental HAADF-STEM results can be reproduced when O replaces N at specific surface sites (S1-related), especially with multiple replacements. Most importantly, the presence of O at various anion sites significantly affects the peak intensities of Lu adsorption on the prism surface.

In the thinner 6 Å IGFs, very similar adsorption sites for Lu are observed for the 26 kinds of various surface terminations. Stronger Lu segregation peaks on the prismatic surface was observed in the density profiles, indicating more Lu ions adsorbing on the prism surface in the 6 Å IGF as compared to the 18 Å IGF. Figure 6.5 shows the density profiles of the Lu segregation and its adsorption sites on the various prismatic surfaces with single replacement in 6 Å IGF. Although the 6 Å IGF and the 18 Å IGF both have the same IGF composition (6% Lu, 30% N/(N+O)), it is worthwhile to mention that the 6 Å IGFs only contain 96 Lu ions (i.e. the absolute number of 96 Lu ions in about 1600 ions of the IGF), less than the 288 Lu ions in the 18 Å IGF. Given this fact and the constant surface area for the prism surface used in both IGF thicknesses, the stronger Lu peaks on the prismatic surface in the 6 Å IGFs actually indicate that a higher ratio of the total number of Lu ions segregate to the prism surface. The weak Lu peaks in the 18 Å IGFs suggest a stronger preference for the Lu ions to stay in the glassy portion of the IGF (i.e. interior IGF), not the crystal surface. Based on that, the strong Lu peaks in the 6 Å IGFs should be attributed to the proximity of the two opposing matrix, which may cause two factors affecting Lu: one, the thin IGF largely reduces the glassy region of the IGF. As a result, the Lu ions barely find enough glassy regions in the interior of the IGF, but have to be packed to the crystal surface; and two, the Lu prefers to form crystalline clusters and the thin IGF inhibits such crystal formation.

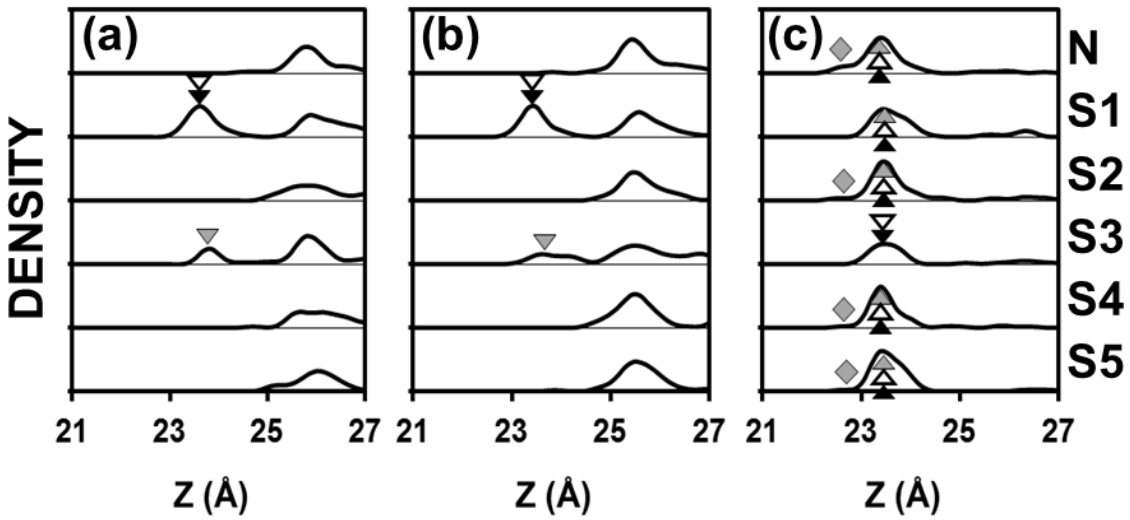

Figure 6.5 Density Profiles of Lu from a 6Å IGF along the z axis on various prismatic surfaces with one site terminated by O, simulated by (a) Lu potential set A; (b) Lu potential set B; (c) Lu potential set C.

6.3.5 Density Profiles of La

Our previous simulations of La adsorption on fully nitride prism surfaces matched the HAADF-STEM results[116,125,130]. However, given the observed importance of O in surface lattice sites in the Lu case and the likely presence of such replacement O in surfaces exposed to IGFs containing other rare-earths, would similar O replacements on the nitride surface of the La-doped IGFs affect the location of La adsorption?

To test this concern, the La interfacial segregation behavior was investigated in the same manner on the same 26 kinds of prismatic surface terminations for three different La potential sets. The density profiles on the pure N surface and from additional simulations of La adsorption with O replacements at the various surface sites are given in Figure 6.6. Results show that La ions sit at the appropriate sites La1 and La2 (empty and

dark triangles, respectively), for most conditions for potential sets A and B, but clearly show the least affected and most consistent results with potential set C.

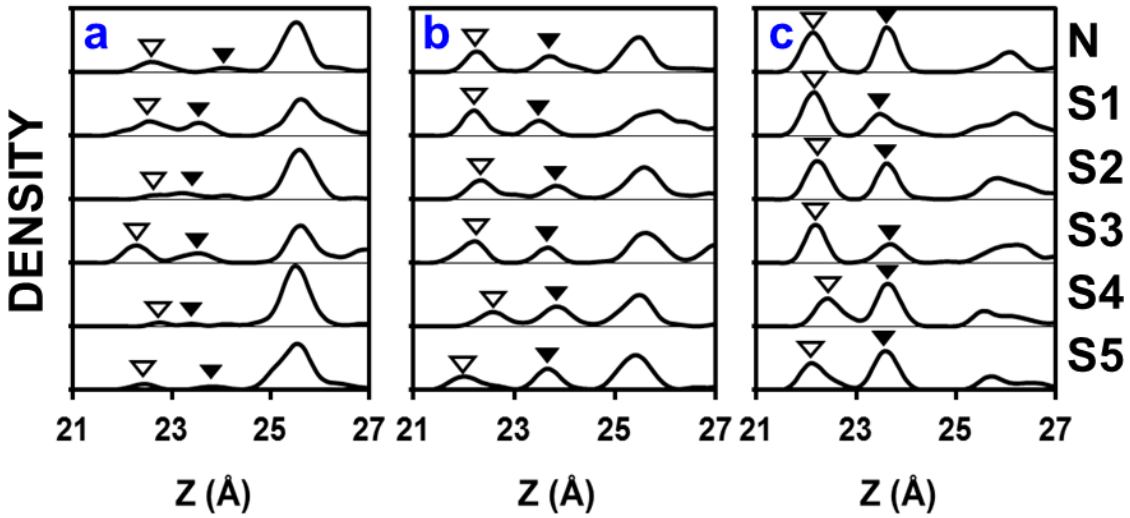

Figure 6.6 Density Profiles of La from an 18Å IGF along the z axis on various prismatic surfaces with one site terminated by O, simulated by (a) La potential set A; (b) La potential set B; (c) La potential set C. Open triangles are site La1, dark triangles are site La2.

In the Lu case, the oxidized prismatic surface is playing an important role in facilitating the correct Lu adsorption sites Lu1 and Lu2. In the La case, the oxygen terminated prismatic surface in general does not greatly affect the locations of the two La adsorption sites La1 and La2 on different kinds of prismatic surfaces. For potential set C, the height of the La1 site is elevated on the S4 terminated prismatic surface, suggesting the effect of oxygen on slight movement of the location of the La adsorption sites. Besides that, single O replacement has little effect on La adsorption sites. Viewing the difference in the peak intensities in Figure 6.6 (c), we can conclude that the oxygen on

the S1 or the S3 prismatic surface could decrease the La2 peak intensity and the oxygen on the S4 or the S5 prismatic surface could decrease the La1 peak intensity. Although Figure 6.1 shows that the La1 site is surrounded by the S3, S4, S5 and S1 sites, it is the lower (in z direction) S4 and S5 sites that affect the La1 occupancy on the prismatic surface. The La2 site is surrounded by the S1, S2 and S3 sites; however, it is the higher S1 and S3 sites that affect the La2 occupancy.

The above ideas can also be used to explain the density profiles in Figure 6.7 for La adsorption sites on the double replacement prismatic surfaces. A slight shifting of the La1 site is observed on the S4-related terminated prismatic surfaces for the double replacement. There is a decrease of the La1 peak intensities in the S4-related and S5-related prismatic surfaces, while there is a reduction of the La2 peak intensity on the S1-related and S3-related prismatic surfaces. However, the effect of O at different surface sites does not have a significant effect on La adsorption, especially for potential set C.

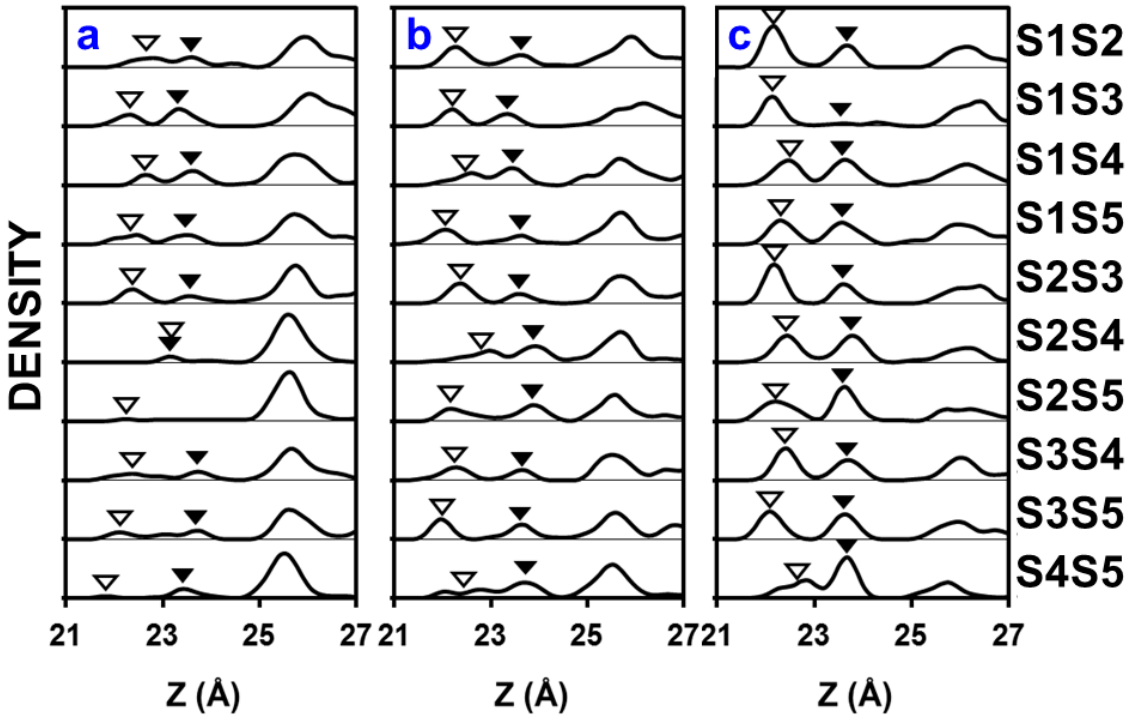

Figure 6.7 Density Profiles of La from an 18Å IGF along the z axis on various prismatic surfaces with two sites terminated by O, simulated by (a) La potential set A; (b) La potential set B; (c) La potential set C.

6.3.6 Density Profiles of Triple Replacement

Replacing three N sites has a greater effect on Lu adsorption in comparison to La adsorption, as shown in Figure 6.8 for the two best potential sets (Lu potential set A and La potential set C). Previous work showed the importance of the composition of the IGF on La adsorption onto the fully nitrided prism surface[116,130]. The current work shows that adsorption can also be affected by the type of anions on the prism surface.

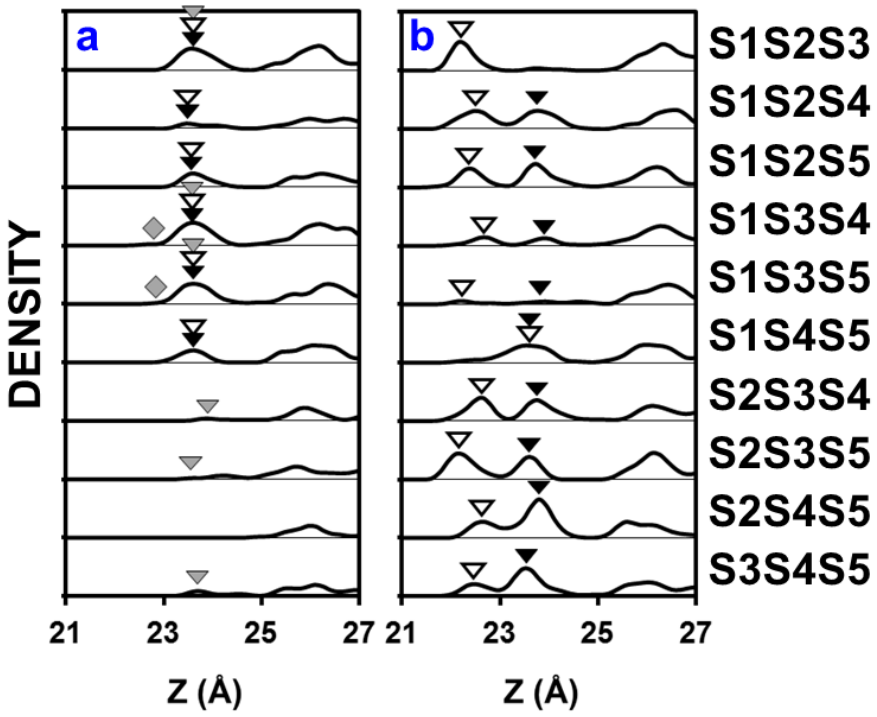

Figure 6.8 Density Profiles of RE ions from an 18Å IGF on various triple replacement surfaces for (a) Lu potential set A, (b) La potential set C.

Knowing the consequences that the oxidation at certain SX site or SX-related site brings about could, conversely, help interpret the experimental La intensity or help explain the experimental differences.

In comparison to the Lu data, the La adsorption sites are relatively unaffected by the presence of O in surface sites, whereas Lu adsorption sites are much less tolerant to the vagaries of anion replacement. In addition, the La peak intensities at sites La1 and La2 are higher than the intensities at the correct sites for Lu, indicating a greater propensity for adsorption in the La case than the Lu case.

A major implication that results from the data presented here is that the adsorption of Lu ions is significantly affected by the presence of O on anion sites on the prism

surface, whereas La ions are considerably less affected. These results provide an atomistic justification for the different morphologies resulting from the experimental data that shows predominantly uniform grain growth in the Lu-doped IGFs systems versus the highly anisotropic grain growth for the La-doped IGFs systems[21,24,127]. The presence of oxygen in the IGF allows for O adsorption in the crystal anion surface sites and O is observed at various sites on the prism β-Si_3N_4 surface[129]. However, while O on specific sites on the prism surface would allow Lu adsorption, inhibiting growth and allowing for some anisotropy, the simulations show that this requires a very specific set of circumstances, so its affect is limited and more grains would grow uniformly rather than anisotropically. However, our results would also explain the presence of some anisotropic grains in the Lu-doped IGF systems, where sufficiently large amount of the appropriate O replacement for N occurs, allowing for stronger Lu adsorption and subsequent Lu poisoning of the prism surface.

In addition, the concentration of Lu on the surface sites is significantly less than La, indicating the reduced presence of Lu on the prism surface, allowing for less poisoning and more uniform grain growth. The current work of replacing all specific N sites (all S1 or all S1S3, etc.) with O is a limiting case. Since not all sites over the whole surface might be exchanged, the beneficial effect of O on certain sites for Lu adsorption would be lessened, reducing Lu-poisoning of the surface. This scenario would allow for growth outward of the prism plane from the nitride region (with no Lu poisoning) and lateral growth of the step towards any portions of the surface that had been poisoned by Lu. An interesting question concerns whether the growing prism plane will stop at the Lu sites, or expel the Lu and continue growth. La does not show this significant dependence

on O content in the prism surface and therefore more regularly shows anisotropic grain growth as the adsorbed La ions poison the prism surface.

6.4 Conclusions

The role of oxygen in the anion sites in β-Si_3N_4 prism surface on Lu and La adsorption from the intergranular film is investigated via molecular dynamics computer simulation. Three sets of parameters in the two-body portion of the multi-body potential are developed for Lu and La, among which the Lu potential set A and the La potential set C appears to the best. With the pure nitrogen terminated prism surface, no Lu adsorption onto the surface is observed. Without the poisoning of the surface afforded by the rare earth segregating from the IGF, uniform grain growth can occur. However, with O replacing N at specific combinations of anion surface lattice sites, the simulations match the experimental coordinates of the adsorbed Lu ions at the Lu1 and Lu2 sites observed in HAADF-STEM. The implication is that the HAADF-STEM results involved oxygen at surface anion sites, which is also consistent with EELS studies. Given the important role of O in the prism surface on Lu adsorption, analysis of the role of O on La adsorption showed that the location of La ions on the prismatic surface does not vary greatly for different kinds of O surface terminations in comparison to the full nitride surface; however, surface oxidation does has an effect on reducing the La surface occupancy. Therefore, oxidation plays a more significant role in the adsorption behavior of Lu than it does for La. In addition, while the energetics of Lu adsorption onto the differently terminated prism surfaces shows differences, the presence of the IGF plays a significant role in the actual adsorption behavior, as seen in the density profiles obtained in the presence of the IGFs.

The results finally provide a justification for the experimentally observed difference in grain growth behavior in the Lu-doped IGFs versus the La-doped IGFs. Here, we show that with a fully nitride surface, Lu does not adsorb onto the prism surface whereas La does. As such, La readily poisons the prism surface, inhibiting uniform grain growth, allowing for the anisotropic growth seen experimentally and in our previous simulations. In the Lu case, without adsorption, uniform growth is possible. However, HAADF-STEM shows Lu at surface sites on the prism surface and EELS shows the presence of O in surface anion sites. The simulations show that the presence of O at certain surface lattice sites plays a major role in the adsorption of Lu ions onto those sites, enabling poisoning and possible anisotropic grain growth. However, because of the very specific nature of the conditions for adsorption (oxygen locations) the simulations show that such poisoning is very limited (the density of Lu sites on the surface is far less than that for La). In contrast, for La, the presence of O at the prism surface sites has little effect on La adsorption, thus enabling more consistent poisoning of the prism surface, inhibiting outward growth of these planes, allowing for the more anisotropic grain growth seen experimentally.

Chapter 7 Different dopant effects of Lu and La in β-Si3N4

7.1 Introduction

Silicon nitride ceramics (Si3N4) are promising high temperature structural ceramics used as engine and turbines parts due to their outstanding mechanical properties at elevated temperatures[45,59,144]. β-Si_3N_4 ceramics can be regarded as whisker-reinforced structural ceramics as their rod-like grains can act as self-reinforcements to toughen the material. However, efforts still need to be made to ensure the high fracture resistance by tailoring the mechanical properties through microstructure optimization[50].

Many Si3N4 are fabricated through liquid phase sintering. Sintering additives such as rare earths and Group III elements can be added to obtain a fully dense form. Intergranular glassy films (IGFs) are formed at the grain boundaries from the densification additives. Lanthanide oxide sintering additives have shown a great influence on the grain aspect ratio and grain size distribution[24]. The dopant atoms can largely control the anisotropic grain growth, thus forming the whisker-like grain morphology[21,22,66]. The anisotropic grain morphology is found to be quite sensitive to the dopant elements[145]; however, the mechanisms are still not fully understood. Therefore, it is important to understand the dopant effects in order to design the high performance ceramics of the next generation at the atomistic level[48,65].

The silicon nitride basal growth along the c-axis is controlled by diffusion and is relatively fast. The prism growth alone the a-axis is controlled by dopant species and is relatively slow. The different speed of grain growth on the basal and prism surface could therefore result in the anisotropic grains or high aspect ratio grains. Many studies have focused on such dopant effect on interfacial reaction rate limited growth

behavior[127,146-150]. Previous molecular dynamics simulations in our group[116,125,130] had predicted different adsorption sites of La and Lu on the prism surface, which is consistent with the scanning transmission electron microscopy images from three research groups[35-38,75]. However, the mechanism of the different role of La and Lu on the silicon nitride grain morphology is still not fully understood. In this paper, we aim to obtain the atomistic details not readily available by experiments, collect dynamic data with corresponding to time, and gain further insights into the mechanisms controlling the RE segregation behavior and grain growth behavior.

7.2 Computational Procedures

7.2.1 Simulation System

The computational system is composed of a prism oriented crystal, a high index oriented crystal, and a grain boundary phase in between. The system dimension is about 98.98 Å in length in the x dimension, 52.42 Å in width in the y dimension, and initially around 77 Å in thickness in the z dimension. There are 13104 atoms in the prism crystal and 7734 atoms in the high index crystal. Around 21273 atoms are first randomly inserted to the grain boundary region. After the system was treated by a melted and quenched process as shown in Table 7.1, a grain boundary phase is obtained. In this paper, two kinds of quenched processes are applied: one quenched until 6000K (Duration 6), the other quenched until 7000K (Duration 7). Here, we focus on the last quenched temperature of the melt-quenched process, namely, the 10 ns duration at 6000K or 7000K. Various glass compositions (0.2%, 0.5%, 1% Lu or La, 70%, 90% N) are studied to

investigate atomistic moving of the Lu or La ions and the silicon nitride crystal growth behavior as a function of composition.

Table 7.1 Melt-quench process

Temperature	Conditions	Duration 6	Duration 7
300K	NVE, crystal frozen	10 ps	10 ps
10,000K	NVE, crystal frozen	20 ps	20 ps
9000K	x,y constant, P_z = 4 GPa, crystal frozen	100 ps	100 ps
8000K	As above	100 ps	100 ps
7000K	As above	1000 ps	10 ns
6000K	As above	10 ns	

Table 7.2 Two-body pair potential parameter sets

i-j pair	A_{ij}(fJ)	ρ_{ij}(Å)	β_{ij}(Å)	ε(fJ)	σ(Å)	Strength (eV)
O-O	0.0725	0.29	2.34			
N-N	0.07241	0.29	2.20			
Si-Si	0.1877	0.29	2.30			
N-O	0.1350	0.29	2.21			
Si-O	0.2962	0.29	2.34			
Si-N	0.7500	0.261	2.2			
La-Si	0.3000	0.32	2.3			
La-La	0.3975	0.57	2.3			La potential set A
La-O	0.8000	0.34	2.5	0.0017	1.83	-10.74
La-N	3.3000	0.323	2.1	0.0024	1.99	-8.68
Lu-Si	0.269	0.4795	2.3			
Lu-Lu	0.3975	0.455	2.3			Lu potential set A
Lu-O	1.57	0.293	2.33	0.002295	1.542	-10.11
Lu-N	1.95	0.2476	1.17	0.001685	1.82	-8.78

7.2.2 Interatomic Potential

Multi-body interatomic potential is employed as a two-body and a three-body part. The two-body part is composed of Born-Mayer-Huggins (BMH) pair potential and the 9-6 Lennard-Jones (LJ) pair potentials, as shown in the following equations.

$$V_{ij}^{2-body} = A_{ij} \exp\left(\frac{-r_{ij}}{\rho_{ij}}\right) + \frac{z_i z_j e^2}{r_{ij}} erfc\left(\frac{r_{ij}}{\beta_{ij}}\right) + V_{ij}^{LJ} \qquad (7.1)$$

$$V_{ij}^{LJ(9-6)} = \frac{27}{4}\varepsilon\left[\left(\frac{\sigma}{r_{ij}}\right)^9 - \left(\frac{\sigma}{r_{ij}}\right)^6\right] \qquad (7.2)$$

where r_{ij} is the separation distance between ion *i* and ion *j*, z_i and z_j are full ionic charges of ion *i* and ion *j*, and in this case +3, +4, -2, -3 for Lu or La, Si, O, N, *e* is the elementary charge, and *erfc* is the complementary error function. Parameters A_{ij}, ρ_{ij}, β_{ij}, ε, and σ for each pair type are listed in Table 7.2.

The three-body part is given in the following equation.

$$V_{jik}^{3-body} = \lambda_{jik} \exp\left(\frac{\gamma_{ij}}{r_{ij} - r_{ij}^0} + \frac{\gamma_{ik}}{r_{ik} - r_{ik}^0}\right)\Omega_{jik} \qquad (7.3)$$

when $r_{ij} < r_{ij}^0$ and $r_{ik} < r_{ik}^0$. Otherwise, $V_{jik}^{3-body} = 0$. Its angular term is given as

$$\Omega_{jik} = (\cos\theta_{jik} - \cos\theta_{jik}^0)^2 \qquad (7.4)$$

where θ_{jik} is the angle formed by ion *j*, ion *i* at its vertex, and ion *k*. The three-body potential is centered only on Si, O, and N ions with parameters given in Table 7.3.

In this paper, similar RE-O and RE-N values are used for Lu and La in Table 7.2. Both have RE-O stronger than RE-N. This will potentially cause La ions with bigger ion size to have more and stronger bonding with the neighboring atoms at long distance than

Lu. This potentially suggests the pinning effect of La on the prism surface. The weaker bonding of Lu with its neighboring atoms will cause weak interfacial bonding of Lu ions with prism surface. Therefore, the size difference of Lu and La could be the potential reason for their different dopant effects.

Table 7.3 Three-body potential parameters

j-i-k trip let	λ_{jik}(fJ)	γ_{ij} (Å)	γ_{ik}(Å)	r^0_{ij}(Å)	r^0_{ik}(Å)	$\cos\theta^0_{jik}$
Si-O-Si / La-O-La / Lu-O-Lu	0.001	2.0	2.0	2.6	2.6	-0.3333
O-Si-O / N-Si-N	0.024	2.8	2.8	3.0	3.0	-0.3333
Si-N-Si	0.035	2.6	2.6	2.8	2.8	-0.5
La-N-La / Lu-N-Lu	0.001	2.0	2.0	2.6	2.6	-0.5

7.3 Results and Discussion

7.3.1 Role of Lu and La on grain growth

In this paper, we show observations of the different roles of Lu and La on the grain growth and morphology. The diametrical growth on the prism surface is found to be limited and controlled by the dopant type. Figure 7.1 shows that silicon nitride prism surface clearly grows two full layers outward in the Lu2O3-doped system. Some Lu clusters are formed, but this does not inhibit crystal growth. Figure 7.1 (b) shows that some Lu ions, which are originally on the prism surface, are moved away during the grain growth. While in Figure 7.2, in the La2O3-doped system, only several parts of the silicon nitride prism grow a half-layer. The La-doped prism grain grows much less than the Lu-doped prism grain. Although the very bottom La ions move up a layer from (a) to (b), there still exists a strong coverage of La ions on the prism surface. The La ions do not cluster, but the thick coverage can act as pinning points on the prism surface. This largely

suppresses the diametrical growth on prism surface during the 10 ns duration. It is very hard to move La ions away from the prism surface, because they can stay stably at the adsorption sites on the prism surface. The silicon nitride crystal will need to go across the pinning points in order to continue to grow.

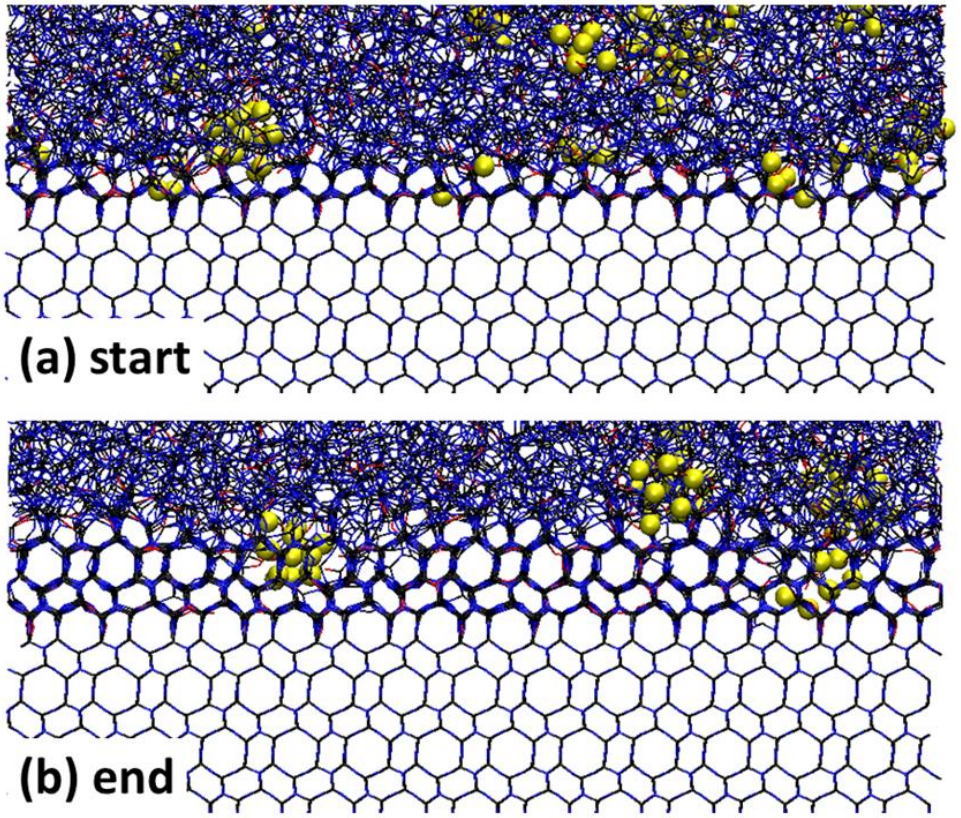

Figure 7.1 Growth behavior on the silicon nitride prism surface for Lu_2O_3-doped glassy phase with 90% N/(N+O) and 1% Lu at 7000K for a duration of 10 nm (a) start, (b) end.

A temperature effect on the silicon nitride prism growth is observed. It is found that prism grain grow at 7000K for 90%N/(N+O) but does not grow at 6000K. Prism grain does not grow at 7000K for 70%N/(N+O), but do grow at 6000K. It seems that a proper temperature is needed for grain growth according to the nitrogen concentration.

This is confirmed for both the 70%N/(N+O) and 90%N/(N+O) samples with 0.2% Lu, 0.5% Lu and 1% Lu content. Considering the above two conditions, it is quite possible that, for a general system, grain growth could first occur at 7000K for IGFs with 90%N/(N+O). When the concentration of the rest glassy portion is then reduced to 70%N/(N+O), grain growth will stop at 7000K, but continue at a lower temperature of 6000K.

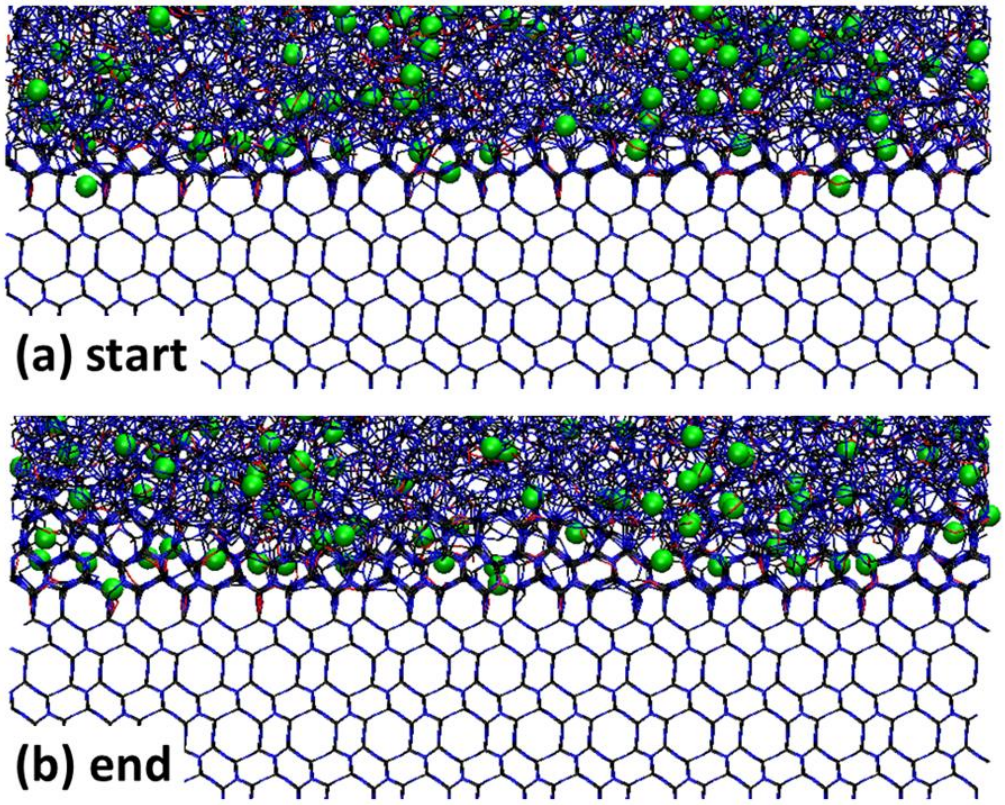

Figure 7.2 Snapshot of the growth behavior on the silicon nitride prism surface for glassy phase doped by La_2O_3 with 90% N/(N+O) and 1% La at 7000K for a duration of 10 nm (a) start, (b) end.

7.3.2 Lu being moved away from prism surface

In Figure 7.3, density profiles show clear orderings of certain species as Si, N, and O between two dashed lines and also near the region on the right. The grain growth

behavior of silicon nitride prism crystal is shown by the increment of ordering layers of Si, N, and O species in the density profiles. Different from the dopant effect of La ions, Lu ions do not serve as pinning points, but could be easily moved away from prism surface as the silicon nitride crystal grows. This is shown in Figure 7.3 as Lu ions being kicked out from the prism surface between the dashed lines from the density profiles. In other words, the Lu peaks between the dashed lines in Figure 7.3 (a) are kicked out from the prism surface in Figure 7.3 (b). There is no strong coverage of Lu on the prism surface, but only some Lu clusters. And these Lu clusters do not stuck on the prism surface, but could be easily moved away. This indicates the essential different roles between Lu and La dopants. Lu2O3 additions could potentially promote surface growth as they do not pin the grain growth, while La2O3 additions strongly hinder the grain growth.

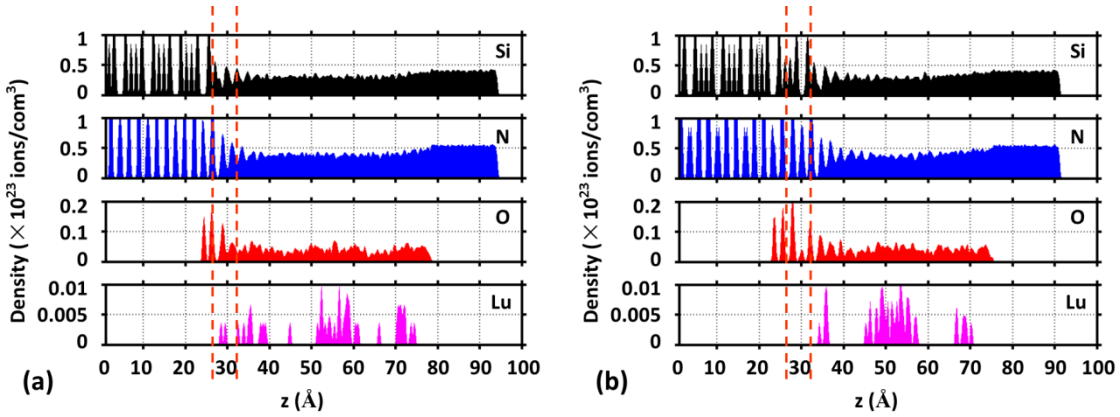

Figure 7.3 Density profiles of species of Si, N, O, and Lu as a function of z location and time f(z,t) for sample of 90% N/(N+O) and 0.2% Lu at 7000K during a 10 ns duration period at (a) start, (b) end. Two dashed lines are marked at same locations for (a) and (b) near 30Å in z.

7.3.3 Energy Evolvement of Lu ions

There is a strong tendency that Lu ions would form clusters. System with high Lu concentration could potentially form larger Lu clusters as long as sufficient diffusion time is allowed. This could be correlated to the “Lu rich region” observed experimentally[151]. Figure 7.4 shows the evolving energies and locations of Lu ions with corresponding to time for the sample of 90% N/(N+O) and 0.2% Lu. Specifically, Lu ions exist as isolated atoms in the system as shown in Figure 7.4 (a). As can be seen, the isolated Lu ions have relatively high energies as shown by red dots. The isolated Lu ions could form small clusters as shown in Figure 7.4 (b). The small clusters have lower energies as orange and green dots. These small clusters can merge and form bigger clusters with lower energies as more blue dots are observed in Figure 7.4 (c) and (d). The energies of the small clusters are greatly reduced as they become relatively bigger clusters. It is worthwhile to mention that the cluster form phenomenon cannot be reversible. In other words, this means that it is very hard to separate a big cluster into several small ones because this process is energetically unfavorable.

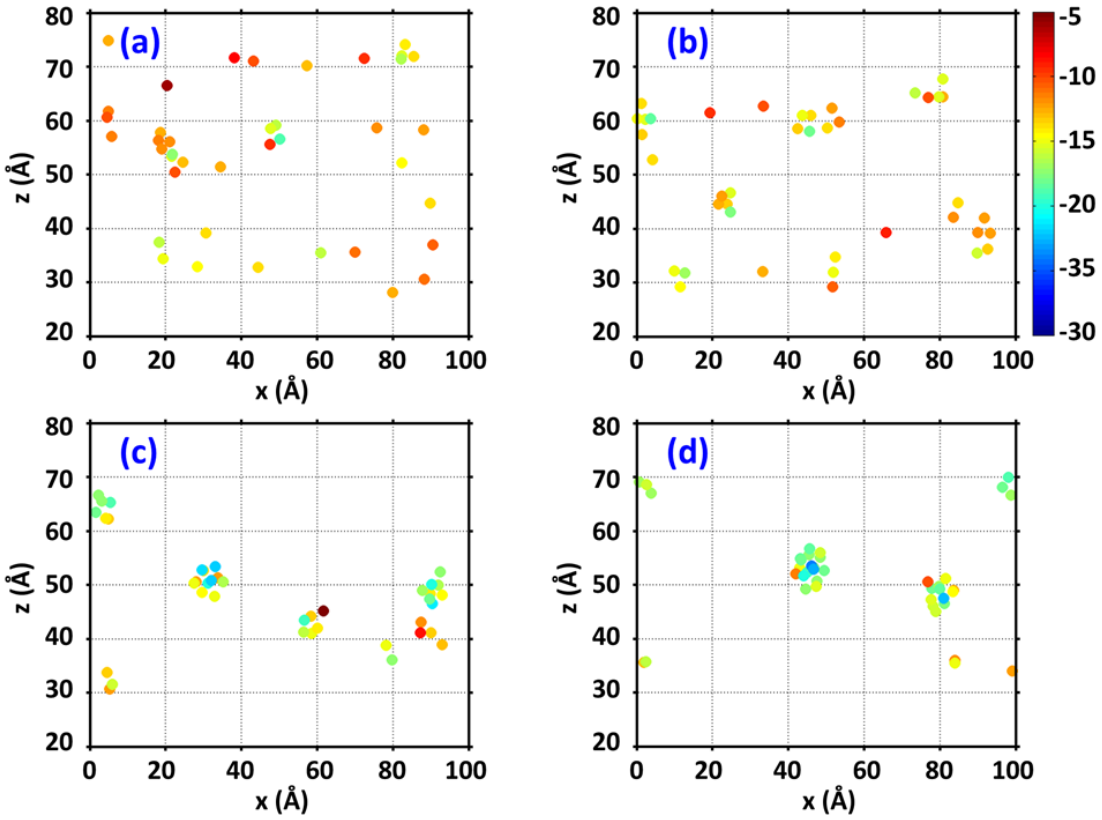

Figure 7.4 The evolution of Lu ions for 90% N/(N+O) and 0.2% Lu sample at (a) start, (b) 2 ns, (3) 5 ns, (4) 10 ns. Locations of the Lu ions are projected on the xoz plane. Energies of the Lu ions are marked by colors.

Energies and locations of Lu ions for sample of 70% N/(N+O) and 0.2% Lu are shown in Figure 7.5. The more oxygen, the smaller the clusters would be. This fit the idea that small clusters are seen at the interface of the 6Å films with HAADF-STEM. The thin films potentially have more oxygen than a large film, because the nitrogen ions attach to the grown silicon nitride prism crystal, leaving more oxygen ions in the remaining and thin film.

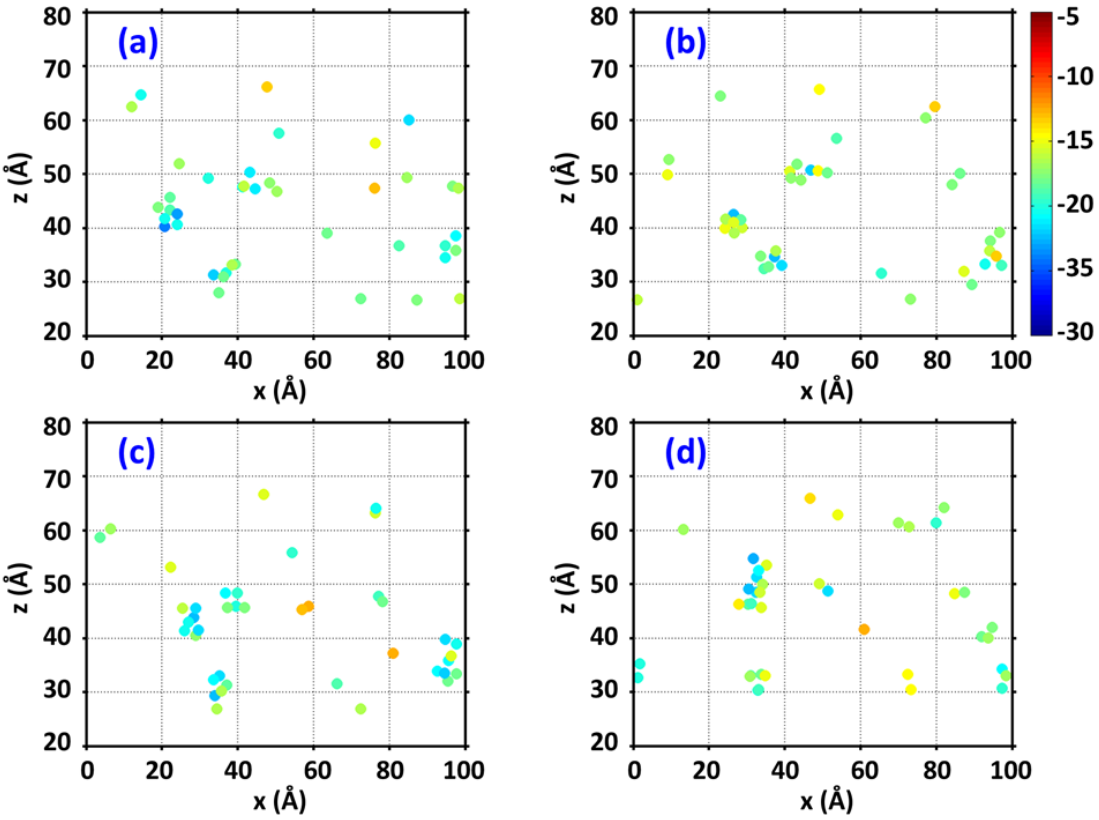

Figure 7.5 The evolution of Lu ions for 70% N/(N+O) and 0.2% Lu sample at (a) start, (b) 2 ns, (3) 5 ns, (4) 10 ns. Locations of the Lu ions are projected on the xoz plane. Energies of the Lu ions are marked by colors.

In summary, the different sizes of Lu and La are most likely the reason that affects the different diametric growth behavior of silicon nitride. Lu ions tend to cluster; therefore, the Lu coverage on the prism surface is not strong. The La coverage is thick on the prism surface. The strong bonding of La ions with their neighboring atoms suggests the pinning effect on the prism surface. The weak bonding of Lu ions with less and weaker neighboring atoms indicates an easier moving of Lu ions on the prism surface.

Chapter 8 Summary

Molecular dynamics computer simulations are used to investigate the locations and energies of La or Lu ions in silicate intergranular films (IGFs) between prism and basal or high index oriented silicon nitride crystals. The atomistic structure of La or Lu doped silicon oxynitride intergranular films are investigated as a function of composition and IGF thickness. Results of the simulations show La adsorption at the four sites on the prism oriented nitride surface that are the same as those observed with HAADF-STEM.

La ions preferentially segregate to the interfaces with no nitrogen in the IGF, but stay both on the interface and in the interior IGF with nitrogen present in the IGF. With no nitrogen in the IGF, the binding energies of La at these two sites differ. With nitrogen, the binding energies are less different between the two surface sites and the interior of the IGF, indicating a decreased driving force for segregation. Given the variation in the experimental HAADF-STEM results, the simulations indicate that a variation in the local composition would cause some IGFs to show segregation of all La to the interface, leaving little La within the glassy IGF, while other IGFs may show more La remaining in the glassy IGF.

In addition, the simulations also show the effect of composition on this behavior, in which La segregation to at least the two closest surface sites on the prism surface is observed at all compositions, whereas La segregation to the basal interface is significantly affected by composition. With increasing La content, La site-filling increases on both prism and basal interfaces. Because of La's role as a network modifier in pure silica glass, IGFs with no N and low La content show complete segregation of the La to the crystal surfaces. Increasing N content in the IGF reduces this La segregation to

the interfaces, allowing for more La in the interior IGF. This is consistent with the change in binding energy of the La ions in the IGF interior in comparison to that at the interfaces, reducing the driving force for segregation. Because the additive rare earth 'poisons' the surface to which it adsorbs from further growth, the change in segregation is important in the development of microstructure in the ceramic. Importantly, increasing N content in the IGF causes preferential La depletion from the basal surface, with no such significant depletion of La on the prism surface, providing a mechanism for the anisotropic grain growth observed in this system.

Our results showed ordered La adsorption onto the prism-terminated surface is not affected by the orientation of the opposing crystal, although the extent of the ordering away from the interface is affected by IGF thickness. La adsorption at ordered sites 1 and 2 on the prism surface occurred for almost all of the compositions in both ~1.8 nm and ~0.6 nm thick IGFs and at sites farther from the prism interface in the thicker IGF, similar to adsorption in triple points. Saturation of available sites is affected by the thickness of the IGF, which governs the number of La ions (and N ions) in the IGF, with lower site filling in the thinner IGF. There are clear energy differences for La in the interior of the IGF vs. the interface based on composition and IGF thickness, with the thicker IGF showing greater variation in driving forces for segregation or La incorporation into the IGF. Fracture is affected by both composition and thickness and occurs in the glassy IGF and not in the ordered interfacial regions, consistent with experimentally observed intergranular fracture for La-doped silicon nitride. Segregation of La to the interface affects N distribution within the interior of the IGF, which affects strength.

We study the important role of oxygen replacing nitrogen at surface sites in the prismatic surface of β-Si_3N_4 on the adsorption of rare earth ions from the intergranular film. Our simulations successfully obtain the correct Lu sites Lu1 and Lu2 on the prismatic surface with O replacement at specific combinations of N surface sites. Results match the experimental HAADF-STEM data. Unlike the Lu results, surface oxidation does not have a large effect on La adsorption sites on the prismatic surface, but does have an influence on the La surface occupancy. The simulation results provide the mechanisms for both the experimental variances observed for the adsorption sites of these two rare-earth additives in the intergranular films and, more importantly, explain the different grain growth behavior seen experimentally.

The different roles of Lu and La on the growth behavior of silicon nitride prism crystal are investigated. Strong La coverage on the prism surface is observed, indicating La ions served as pinning point and suppress the prism growth. Lu clusters being kicked out from the prism surface is observed, showing that Lu ions can move easily moved away from prism surface. A proper temperature range is suggested as grain grows at a certain N content.

References

[1] Clarke, D. R. Grain boundaries in polycrystalline ceramics. *Ann. Rev. Mater. Sci.* **17**, 57-74 (1987).

[2] Pezzotti, G. Mechanical spectroscopy methods for the quantitative analysis of intergranular glass viscosity in polycrystalline ceramics. *J of Non-Cryst. Sol.* **321**, 37-51 (2003).

[3] Mazurin, O. V., Streltsina, M. V. & Shvaiko-Shvaikovskaya, T. P. *Handbook of Glass Data Part A; Silica glass and binary silicate glasses*. (Elsevier, 1983).

[4] Kolar, D. in *Sintering of Advanced Ceramics* Vol. 7 *Ceramic Transactions* (ed J. E. Blendell C. A. Handwerker) (Am. Ceram. Soc., 1990).

[5] Becher, P. F., Painter, G. S., Sun, E. Y., Hsueh, C. H. & Lance, M. J. The importance of amorphous intergranular films in self-reinforced Si3N4 ceramics. *Acta Mater.* **48**, 4493-4499 (2000).

[6] Falk, L. K. L. Microstructural Development During Liquid Phase Sintering of Silicon Carbide Ceramics. *J. Eur. Ceram. Soc.* **17**, 983 (1997).

[7] Subramaniam, A., koch, C. T. & Cannon, R. M. Intergranular glassy films: an overview. *Mater. Sci. Eng. A* **422**, 3-18 (2006).

[8] Becher, P. in *Workshop on Interfaces in Silicon-Based Ceramics.*

[9] Bruley, J., Tanaka, I., Kleebe, H.-J. & Rühle, M. Chemistry of Grain Boundaries in Calcia Doped Silicon Nitride Studied by Spatially Resolved Electron Energy-Loss Spectroscopy. *Analy. Chemica Acta* **297**, 97-108 (1994).

[10] Kleebe, H.-J. Structure and Chemistry of Interfaces in Si3N4 Ceramics Studied by Transmission Electron Microscopy. *J. Ceram. Soc. Japan* **105**, 453-475 (1997).

[11] Pezzotti, G. *et al.* Chemistry and inherent viscosity of glasses segregated at grain boundaries of silicon nitride and silicon carbide ceramics. *Journal of Non-Crystalline Solids* **271**, 79-87 (2000).

[12] Kaplan, W. D., Mullejans, H. & Ruhle, M. Ca Segregation to Basal Surface in a-Alumina. *J. Am. Ceram. Soc.* **78**, 2841-2844 (1995).

[13] Gu, H., Pan, X., Cannon, R. M. & Rühle, M. Dopant Distribution in Grain-Boundary Films in Calcia-Doped Silicon Nitride Ceramics. *J. Am. Ceram. Soc.* **81**, 3125-3135 (1998).

[14] Gu, H., Cannon, R. M., Tanaka, I. & Ruhle, M. Calcia partition in phase-separated intergranular glass and interfaces in doped silicon nitride produced by hot pressing. *Matl. Sci. Eng. A* **422**, 51-65 (2006).

[15] Bae, S. I. & Baik, S. Determination of Critical Concentrations of Silica and/or Calcia for Abnormal Grain Growth in Alumina. *J. Am. Ceram. Soc.* **76**, 1065-1067 (1993).

[16] Becher, P. F. *et al.* Debonding of Interfaces Between Beta-Silicon Nitride Whiskers and Si-Al-Y Oxynitride Glasses. *Acta. Mater.* **44**, 3881-3893 (1996).

[17] Gu, H., Cannon, R. M. & Rühle, M. Composition and chemical width of ultra-thin amorphous films at grain boundaries in silicon nitride. *J. Mater. Res.* **13**, 376-387 (1998).

[18] Tanaka, I. *et al.* Calcium Concentration Dependence of the Intergranular Film Thickness in Silicon Nitride. *J. Am. Ceram. Soc.* **77**, 911-914 (1994).

[19] MacLaren, I., Cannon, R. M., Gulgun, M. A. & Ruhle, M. Abnormal grain growth in alumina: synergistic effects of yttria and silica. *J. Am. Ceram. Soc.* **86**, 650-659 (2003).

[20] Satet, R. L. & Hoffmann, M. J. Impact of the intergranular film properties on microstructure and mechanical behaviour of silicon nitride. *Key Eng. Mat.* **265-268**, 775-780 (2004).

[21] Satet, R. L. & Hoffmann, M. J. Influence of the rare-earth element on the mechanical properties of RE-Mg bearing silicon nitride. *J. Am. Ceram. Soc.* **88**, 2485-2490 (2005).

[22] Becher, P. F. *et al.* Influence of additives on anisotropic grain growth in silicon nitride ceramics. *Matl. Sci. Eng. A* **422**, 85-91 (2006).

[23] Baram, M. & Kaplan, W. D. Intergranular films at Au-sapphire interfaces. *J. Mater. Sci.* **41**, 7775-7784 (2006).

[24] Satet, R. L., Hoffmann, M. J. & Cannon, R. M. Experimental evidence of the impact of rare-earth elements on particle growth and mechanical behaviour of silicon nitride. *Mat. Sci. Eng. A* **422**, 66-76 (2006).

[25] Luo, J. Stabilization of nanoscale quasi-liquid interfacial films in inorganic materials: a review and critical assessment. *Crit. Rev. Sol. St. Matls. Sci.* **32**, 67-109 (2007).

[26] Joonchul Jung, S. B. Abnormal Grain Growth of Alumina: CaO Effect. *J. Am. Ceram. Soc.* **86**, 644-649 (2003).

[27] Echeberria, J., Castro, F. & Riley, F. L. Grain Growth in Liquid-Sintered Alumina. *Mat. Sci. Forum* **113 / 115**, 579-584 (1993).

[28] Bae, S. I. & Baik, S. Abnormal Grain Growth of Alumina. *J. Am. Ceram. Soc.* **80**, 1149-1156 (1997).

[29] Bae, S. I. & Baik, S. Sintering and grain growth of ultrapure alumina. *J. Mat. Sci.* **28**, 4197-4204 (1993).

[30] Jung, J. & Baik, S. Abnormal grain growth of alumina: CaO effect. *J. Am. Ceram. Soc.* **86**, 644-649 (2003).

[31] Hoffmann, M. J. in *Tailoring of Mechanical Properties of Si3N4 Ceramics* (ed M. J. Hoffmann and G. Petzow) 59-72 (Kluwer Academic Publ., Netherlands, 1994).

[32] Sun, E. Y. *et al.* Debonding behavior between beta-Si3N4 whiskers and oxynitride glasses with or without an epitaxial beta-SiAlON interfacial layer. *Acta Mater.* **47**, 2777-2785 (1999).

[33] Tanaka, I., Igashira, K., Okamoto, T. & Niihara, K. High temperature fracture mechanism of low-Ca doped silicon nitride. *J. Am. Ceram. Soc.* **78**, 673-679 (1995).

[34] McBride, W. & Cockayne, D. J. H. The structure of nanovolumes of amorphous materials. *J. of Non-Cryst. Sol.* **318**, 233-238 (2003).

[35] Shibata, N. *et al.* Observation of rare-earth segregation in silicon nitride ceramics at subnanometer dimensions. *Nature* **428**, 730-733 (2004).

[36] Ziegler, A. *et al.* Interface Structure and Atomic Bonding Characteristics in Silicon Nitride Ceramics. *Science* **306**, 1768-1770 (2004).

[37] Winkelman, G. B. *et al.* Three-dimensional organization of rare-earth atoms at grain boundaries in silicon nitride. *Appl. Phys. Lett.* **87**, 061911-061911-061913 (2005).

[38] Winkelman, G. B. *et al.* The crystal/glass interface in doped Si3N4. *Mater. Sci. and Eng. A* **422**, 77-84 (2006).

[39] Ziegler, A. *et al.* Atomic-resolution observations of semicrystalline intergranular thin films in silicon nitride. *Appl. Phys. Lett.* **88**, 041919 (2006).

[40] Dillon, S. J. & Harmer, M. P. Multiple grain boundary transitions in cramics: A case study of alumina. *Acta Mater.* **55**, 5247-5254 (2007).

[41] Cinibulk, M. K., Kleebe, H.-J. & Rühle, M. Quantitative Comparison of TEM Techniques for Determining Amorphous Intergranular Film Thickness. *J. Am. Ceram. Soc.* **76**, 426-432 (1993).

[42] Ziegler, A., Kisielowski, C., Hoffmann, M. J. & Ritchie, R. O. Atomic resolution transmission electron microscopy of the intergranular structure of a Y2O3-containing silicon nitride ceramic. *J. Am. Ceram. Soc.* **86**, 1777-1785 (2003).

[43] Clarke, D. On the Equilibrium Thickness of Intergranular Glass Phases in Ceramic Materials. *J. Am. Ceram. Soc.* **70**, 15-22 (1987).

[44] Clarke, D. R., Shaw, T. M., Philipse, A. P. & Horn, R. G. Possible Electrical Double-Layer Contribution to the Equilibrium Thickness of Intergranular Glass Films in Polycrystalline Ceramics. *J. Am. Ceram. Soc.* **76**, 1201-1204 (1993).

[45] Riley, F. L. Silicon Nitride and Related Materials. *J. Am. Ceram. Soc.* **83**, 245-265 (2000).

[46] Tajima, Y. Development of high-performance silicon nitride ceramics and their applications. *Mater. Res. Soc. Symp. proc.* **287**, 189-196 (1993).

[47] Pezzotti, G., Kleebe, H. J. & Nishida, T. Growth isotherms of liquid-phase sintered silicon nitride. *J. Am. Ceram. Soc., Jpn.* **105**, 638-640 (1997).

[48] Hoffmann, M. J., Gu, H. & Cannon, R. M. Influence of the interfacial properties on the microstructural development and properties of silicon nitride ceramics. *Mater. Res. Soc. Symp. Proc.* **586**, 65-74 (2000).

[49] Becher, P. F., Painter, G. S., Sun, E. Y., Hsueh, C. H. & Lance, M. J. The importance of amorphous intergranular films in self-reinforced beta-Si3N4 ceramics. *J. Am. Ceram. Soc.* **48**, 4493-4499 (2000).

[50] Doblinger, M. *et al.* Structural and compositional comparison of Si3N4 ceramics with different fracture modes. *Acta Mater.* **54**, 1949-1956 (2006).

[51] Bouchaud, E. Scaling properties of cracks. *J. Phys. Cond. Matter* **9**, 4319-4344 (1997).

[52] Daguier, P., Nghiem, B., Bouchaud, E. & Creuzet, F. Pinning and Depinning of Crack fronts in Heterogeneous Materials. *Phy. Rev. Lett.* **78**, 1062-1065 (1997).

[53] Cédarié, F., Prades, S. & Bonamy, D. Glass Breaks like Metal, but at the Nanometer Scale. *Phy. Rev. Lett.* **90**, 075504-075501-075504 (2003).

[54] Rountree, C. L. *et al.* Atomistic aspects of crack propagation in brittle materials: multimillion atom molecular dynamics simulations. *Ann. Rev. Mater. Res.* **32** (2002).

[55] Sun, E. Y., Becher, P. F. & Plucknett, K. P. Microstructural design of silicon nitride with improved fracture toughness: II, Effects of yittria and alumina additives. *J. Am. Ceram. Soc.* **81**, 2831-2840 (1998).

[56] Zenotchkine, M., Shuba, R. & Chen, I. W. Liquid-Phase Growth of Small Crystals for Seeding α-SiAlON Ceramics. *Journal of the American Ceramic Society* **87**, 1040-1046 (2004).

[57] Zenotchkine, M., Shuba, R. & Chen, I. W. Effect of Seeding on the Microstructure and Mechanical Properties of α-SiAlON: III, Comparison of Modifying Cations. *Journal of the American Ceramic Society* **86**, 1168-1175 (2003).

[58] Cinibulk, M. K., Thomas, G. & Johnson, S. M. Strength and Creep Behavior of Rare-Earth Disilicate–Silicon Nitride Ceramics. *Journal of the American Ceramic Society* **75**, 2050-2055 (1992).

[59] Wiederhorn, S. M. & Ferber, M. K. Silicon nitride for gas turbines. *Curr. Opin. Solid State Mater. Sci.* **5**, 311-316 (2001).

[60] Becher, P. F. *et al.* Microstructural Design of Silicon Nitride with Improved Fracture Toughness: I, Effects of Grain Shape and Size. *Journal of the American Ceramic Society* **81**, 2821-2830 (1998).

[61] Evans, A. G. Perspective on the development of high-toughness ceramics. *J. Am. Ceram. Soc.* **73**, 187-206 (1990).

[62] Kleebe, H. J., Pezzotti, G. & Ziegler, G. Microstructure and fracture toughness of Si3N4 ceramics: combined roles of grain morphology and secondary phase chemistry. *J. Am. Ceram. Soc.* **82**, 1857-1867 (1999).

[63] Wereszczak, A. A. *et al.* Asymmetric Tensile and Compressive Creep Deformation of Hot-isostatically-pressed Y2O3-Doped-Si3N4. *J. Eur. Ceram. Soc.* **19**, 227-237 (1999).

[64] Painter, G. S., Becher, P. F., Kleebe, H.-J. & Pezzotti, G. First-principles study of the effects of halogen dopants on the properties of intergranular films in silicon nitride ceramics. *Phys. Rev. B* **65**, 064113-064111-064111 (2002).

[65] Kitayama, M., Hirao, K. & Kanzaki, S. Effect of Rare Earth Oxide Additives on the Phase Transformation Rates of Si3N4. *J. Am. Ceram. Soc.* **89**, 2612-2618 (2006).

[66] Becher, P. F., Painter, G. S., Shibata, N., Waters, S. B. & Lin, H. Effects of Rare-Earth (RE) Intergranular Adsorption on the Phase Transformation, Microstructure Evolution, and Mechanical Properties in Silicon Nitride with RE2O3+MgO Additives: RE-La, Gd, and Lu. *J. Am. Ceram. Soc.* **91**, 2328-2336 (2008).

[67] Samaddar, B. N., Kingery, W. D. & Cooper, A. R. Dissolution in Ceramic Systems: I, Molecular Diffusion, Natural Convection, and Forced Convection Studies of Sapphire Dissolution in Calcium Aluminum Silicate. *J. Am. Ceram. Soc.* **47**, 37-43 (1964).

[68] Samaddar, B. N., D., K. W. & Cooper, A. R. Dissolution in Ceramic Systems: II, Dissolution of Alumina, Mullite, Anorthite, and Silica in a Calcium-Aluminum-Silicate Slag. *J. Am. Ceram. Soc.* **47**, 249-254 (1964).

[69] Oishi, Y., Cooper, A. R. & Kingery, W. D. Dissolution in Ceramic Systems: III, Boundary Layer Concentration Gradients. *J. Am. Ceram. Soc.* **48**, 88-95 (1965).

[70] Wang, C. M. & Mitomo, M. Atomic structural environment of Y in the residual glass phase of silicon nitride and alpha-sialon. *Acta Mater.* **50**, 3151-3158 (2002).

[71] Pezzotti, G. & Painter, G. S. Mechanisms of dopant induced changes in intergranular SiO2 viscosity in polycrystalline silicon nitride. *J. Am. Ceram. Soc.* **85**, 91-96 (2002).

[72] Kleebe, H.-J., Hoffmann, M. J. & Rühle, M. Influence of Second Phase Chemistry on Grain Boundary Film Thickness in Silicon Nitride. *Z. Metallkd* **83**, 610-617 (1992).

[73] Cinibulk, M. K., Kleebe, H.-K. & Rühle, M. Amorphous intergranular films in silicon nitride ceramics quenched from high temperatures. *J. Am. Ceram. Soc.* **76**, 2801-2808 (1993).

[74] Averill, F. W. & Painter, G. S. Symmetrized partial-wave method for density-functional cluster calculations. *Physical Review B* **50**, 7262-7267 (1994).

[75] Dwyer, C. *et al.* Interfacial structure in silicon nitride sintered with lanthanide oxide. *J. Mater. Sci.* **41**, 4405-4412 (2006).

[76] Ziegler, A., McNancy, J. M., Hoffmann, M. J. & Ritchie, R. O. On the effect of local grain-boundary chemistry on the macroscopic properties of a high purity Y2O3-Al2O3-containing silicon nitride ceramic: role of oxygen. *J. Am. Ceram. Soc.* **88**, 1900-1908 (2005).

[77] Walkosz, W., Idrobo, J. C., Klie, R. F. & Ogut, S. Reconstructions and nonstoichiometry of oxygenated β-Si_3N_4 (10-10) surfaces. *Phys. Rev. B* **78** (2008).

[78] Painter, G. S. *et al.* First-principles study of rare earth adsorption at beta-Si3N4 interfaces. *Phys. Rev. B* **78**, 214206 (2008).

[79] Rulis, P. *et al.* Electronic structure and bonding of intergranular glassy films (IGF) in polycrystalline Si3N4: Ab-initio studies and classical MD simulations. *Phys.Rev. B* **71**, 235317-235311-235310 (2005).

[80] Ching, W. Y., Rulis, P., Ouyang, L. & Misra, A. Ab initio tensile experiment on a model of an intergranular glassy film in β-Si_3N_4 with prismatic surfaces. *Appl. Phys. Lett.* **94**, 051907 (2009).

[81] Blonski, S. & Garofalini, S. H. Atomistic Structure of Calcium Silicate Intergranular Films in Alumina Studied by Molecular Dynamics Simulations. *J. Am. Ceram. Soc.* **80**, 1997-2004 (1997).

[82] Frenkel, D. & Smit, B. *Understanding Molecular Simulation: from Algorithms to Applications*. (Academic Press, 2002).

[83] Rapaport, D. C. *The art of molecular dynamic simulations*. 2nd edn, (Cambridge University Press, 2004).

[84] Allen, M. P. & Tildesley, D. J. *Computer Simulation of Liquids*. 1st Edition edn, (Oxford University Press, 1987).

[85] Alder, B. J. & Wainwright, T. E. Studies in Molecular Dynamics I. General method. *J. Chem. Phys.* **31**, 459-466 (1959).

[86] Rahman, A. Correlations in the Motion of Atoms in Liquid Argon. *Phys. Rev.* **136**, 405-409 (1964).

[87] Verlet, L. Computer "Experiments" on Classical Fluids. I. Theromdynamical Properties of Lennard-Jones Molecules. *Phys. Rev.* **159**, 98-159 (1967).

[88] Feuston, B. P. & Garofalini, S. H. Empirical Three-Body Potential for Vitreous Silica. *J. Chem. Phys.* **89**, 5818-5824 (1988).

[89] Su, X. & Garofalini, S. H. Atomistic structure of calcium silicate intergranular films between prism and basal planes in silicon nitride: a molecular dynamics study. *J. Mat. Res.* **19**, 752-758 (2004).

[90] Painter, G. S., Becher, P. F., Shelton, W. A., Satet, R. L. & Hoffmann, M. J. First-principles study of rare-earth effects on grain growth and microstructure in beta-Si3N4 ceramics. *Phys. Rev. B* **70**, 144108-144101-144104 (2004).

[91] Garofalini, S. H. & Zhang, S. in *Mat. Res. Soc. Symp. Proc.* Vol. 751 (eds K. B. Alexander *et al.*) 191-200 (Matls. Res. Soc., Pittsburgh, PA., 2003).

[92] Zhang, S. & Garofalini, S. H. Molecular dynamics simulations of the effect of the composition of calcium alumino-silicate intergranular films on alumina grain growth. *J. Phys. Chem. B* **110**, 2233-2240 (2006).

[93] Garofalini, S. H. & Luo, W. Molecular dynamics simulations of calcium silicate intergranular films between silicon nitride crystals. *J. Am. Ceram. Soc.* **86**, 1741-1752 (2003).

[94] Litton, D. A. & Garofalini, S. H. Atomistic Structure of Sodium and Calcium Silicate Intergranular Films in Alumina by Molecular Dynamics. *J. Mat. Res.* **14**, 1418-1429 (1999).

[95] Garofalini, S. H. & Zhang, S. Molecular dynamics simulations of the effect of the composition of the intergranular film on fracture in Si3N4. *J. Am. Ceram. Soc.* **93**, 235-240 (2010).

[96] Chevire, F. & DiSalvo, F. J. A new ternary nitride La2GaN3: Synthesis and crystal structure. *J. Alloys Comp.* **457**, 372-375 (2008).

[97] Pan, X. *et al.* Grain-Boundary Microstructure and Chemistry of a Hot Isostatically Pressed High-Purity Silicon Nitride. *J. Am. Ceram. Soc.* **79**, 2313-2320 (1996).

[98] Kleebe, H.-J., Cinibulk, M. K., Cannon, R. M. & Rühle, M. Statistical Analysis of the Intergranular Film Thickness in Silicon Nitride Ceramics. *J. Am. Ceram. Soc.* **76**, 1969-1977 (1993).

[99] Wang, C.-M., Pan, X., Hoffmann, M. J., Cannon, R. M. & Ruhle, M. Grain boundary films in rare-earth-based silicon nitride. *J. Am. Ceram. Soc.* **79**, 788-792 (1996).

[100] Ramamurthy, S., Schmalzried, H. & Carter, C. B. Interaction of silicate liquid with a sapphire surface. *Phil. Mag. A* **80**, 2651-2674 (2000).

[101] Carter, C. B. & Rasmussen, Y. K. Growth of spinel particles on alumina thin films--II. Morphology and crystallography of the interface. *Acta Met.* **42**, 2741 (1994).

[102] Simpson, Y. K. & Carter, C. B. Faceting Behavior of Alumina in the Presence of a Glass. *J. Am. Ceram. Soc.* **73**, 2391-2398 (1990).

[103] Painter, G. S., Becher, P. F. & Sun, E. Y. Bond energetics at intergranular interfaces in alumina-doped silicon nitride. *J. Am. Ceram. Soc.* **85**, 65-67 (2002).

[104] Koch, C. T. & Garofalini, S. H. Determining the radial pair-distribution function within intergranular amorphous films by numerical nanodiffraction. *Ultramic.* **106**, 383-388 (2006).

[105] Ziegler, A., Cinibulk, M. K., Kisielowski, C. & Ritchie, R. O. Atomic-scale observation of the grain boundary structure of Yb-doped and heat-treated silicon nitride ceramics. *Appl. Phys. Lett.* **91**, 141906 (2007).

[106] Mallamaci, M. P. & Carter, C. B. Faceting of the interface between Al2O3 and anorthite glass. *Acta Mater.* **46**, 2895-2907 (1998).

[107] Pezzotti, G., Ota, K. & Kleebe, H.-J. Viscous Slip along Grain Boundaries in Chlorine-Doped Silicon Nitride. *J. Am. Ceram. Soc.* **80**, 2341-2348 (1997).

[108] Wakai, F., Nagano, T. & Iga, T. Hardening in Creep of Alumina by Zirconium Segregation at the Grain Boundary. *J. Am. Ceram. Soc.* **80**, 2361-2366 (1997).

[109] Song, S. & Coble, R. L. Origin and Growth Kinetics of Platelike Abnormal Grains in Liquid-Phase-Sintered Alumina. *J. Am. Ceram. Soc.* **73**, 2077-2085 (1990).

[110] Yoshiya, M., Tatsumi, K., Tanaka, I. & Adachi, H. Theoretical study on the chemistry of intergranular glassy film in Si3N4-SiO2 ceramics. *J. Am. Ceram. Soc.* **85**, 109-112 (2002).

[111] Ching, W.-Y., Mo, S.-D. & Chen, Y. Calculation of XANES/ELNES spectra of all edges in Si3N4 and Si2N2O. *J. Am. Ceram. Soc.* **85**, 11-15 (2002).

[112] Garofalini, S. H. & Zhang, S. The effect of the composition of the intergranular film in alumina on preferential adsorption and growth. *J. Mater. Sci.* **41**, 5053-5060 (2006).

[113] Litton, D. A. & Garofalini, S. H. Molecular Dynamics Simulations of Calcium Alumino-Silicate Intergranular Films on (0001) Alumina Faces. *J. Am. Ceram. Soc.* **83**, 2273-2281 (2000).

[114] Su, X. & Garofalini, S. H. Role of Nitrogen on the Atomistic Structure of the Intergranular Film in Silicon Nitride: A Molecular Dynamics Study. *J. Mat. Res.* **19**, 3679-3687 (2004).

[115] Zhang, S. & Garofalini, S. H. Molecular dynamic computer simulations of the interface structure of calcium-alumino-silicate intergranular films between combined basal and prism planes of a-Al2O3. *J. Am. Ceram. Soc.* **88**, 202-209 (2005).

[116] Jiang, Y. & Garofalini, S. H. Molecular dynamics simulations of the locations of La ions in La-Si-O-N intergranular films in silicon nitride. *J. Am. Ceram. Soc.* **93**, 3886-3892 (2010).

[117] Zhang, S. & Garofalini, S. H. Molecular dynamics computer simulations of diffusion in calcium-alumino-silicate intergranular films between crystals of alpha-Al2O3. *J. Am. Ceram. Soc.* **88**, 3162-3169 (2005).

[118] Gravereau, P. *et al.* Na3La9O3(BO3)8, a new oxyborate in the ternary system Na2O-La2O3-B2O3: preparation and crystal structure. *Solid State Sci.* **4**, 993-998 (2002).

[119] Weber, R., Benmore, C. J., Siewenie, J., Urquidi, J. & Key, T. S. Structure and bonding in single- and two-phase alumina-based glasses. *Phys. Chem. Chem. Phys.* **6**, 2480-2483 (2004).

[120] Du, J. & Corrales, R. Understanding lanthanum aluminate glass structure by correlating molecular dynamics simulaiton results with neutron and X-ray scattering data. *J. Non-Cryst. Solids* **353**, 210-214 (2007).

[121] Lipp, C. & Schleid, T. Hydrogenoxosiliates of the lanthanides II. La9OMg[SiO4]6[SiO3(OH)] with cerite-like structure. *J. Alloys Compds.* **451**, 657-661 (2008).

[122] Song, H. & Coble, R. Morphology of Platelike Abnormal Grains in Liquid-Phase-Sintered Alumina. *J. Am. Ceram. Soc.* **73**, 2086-2090 (1990).
[123] Yoshiya, M., Tanaka, I. & Adachi, H. Energetical role of modeled intergranular glassy film in Si3N4-SiO2 ceramics. *Acta mater.* **48**, 4641-4645 (2000).
[124] Hudson, T. S., Nguyen-Mahn, D., van Duin, A. C. T. & Sutton, A. P. Grand canonical Monte Carlo simulations of intergranular glassy films in beta silicon nitride. *Mater. Sci. and Eng. A* **422**, 123-135 (2006).
[125] Jiang, Y. & Garofalini, S. H. Molecular dynamics simulations of La2O3-doped silicate intergranular films in Si3N4. *J. Mater. Chem.* **20**, 10359-10365 (2010).
[126] Zhang, S. & Garofalini, S. H. Effect of thickness of the intergranular film on fracture in Si3N4. *J. Am. Ceram. Soc.* **92**, 147-151 (2009).
[127] Satet, R. L. & Hoffmann, M. J. Grain growth anisotropy of beta-silicon nitride in rare-earth doped oxynitride glasses. *J. Eur. Ceram. Soc.* **24**, 3437-3445 (2004).
[128] Winkelman, G. B. *et al.* Arrangement of rare-earth elements at prismatic grain boundaries in silicon nitride. *Philisophical Magazine Letters* **84**, 755-762 (2004).
[129] Walkosz, W. *et al.* Crystal-induced effects at crystal/amorphous interfaces: The case of Si_3N_4/SiO_2. *Phys. Rev. B* **82** (2010).
[130] Jiang, Y. & Garofalini, S. H. Effect of thickness and composition on the structure and ordering in La-doped intergranular films between Si3N4 crystals. *Acta Mater.* **59**, 5368-5377 (2011).
[131] Mulokozi, A. M. An alloying theory of transition metals with p-block elements V: The heats of formation of stoichiometric rare earth nitrides. *Journal of the Less Common Metals* **80**, 235-240 (1981).
[132] Iwata, T. *et al.* Lanthanum- and Oxygen-Deficient Crystal Structures of Oxide–Ion Conducting Apatite-Type Silicates. *Journal of the American Ceramic Society* **91**, 3714-3720 (2008).
[133] Inoue, Z., Mitomo, M. & Ii, N. A crystallographic study of a new compound of lanthanum silicon nitride, LaSi3N5. *J Mater Sci* **15**, 2915-2920 (1980).
[134] Hu, L. *et al.* Luminescence of Ce 3 + in lanthanum silicon oxynitride. *Chinese Physics B* **19**, 127807 (2010).
[135] Takahashi, J. *et al.* Crystal Structure of La4Si2O7N2 Analyzed by the Rietveld Method Using the Time-of-Flight Neutron Powder Diffraction Data. *Chemistry of Materials* **15**, 1099-1104 (2003).
[136] Bo, L. *et al.* First-principles study of oxygen vacancies in Lu 2 SiO 5. *Journal of Physics: Condensed Matter* **19**, 436215 (2007).
[137] Chiriu, D. *et al.* Structural characterization of Lu_{1.8}Y_{0.2}SiO_{5} crystals. *Physical Review B* **76**, 054112 (2007).
[138] Gustafsson, T., Klintenberg, M., Derenzo, S., Weber, M. & Thomas, J. Lu2SiO5 by single-crystal X-ray and neutron diffraction. *Acta Crystallographica Section C: Crystal Structure Communications* **57**, 668-669 (2001).
[139] Pidol, L. *et al.* EPR study of Ce3+ ions in lutetium silicate scintillators Lu2Si2O7 and Lu2SiO5. *Journal of Physics and Chemistry of Solids* **67**, 643-650 (2006).
[140] Bretheau-Raynal, F., Lance, M. & Charpin, P. Crystal data for Lu2Si2O7. *Journal of Applied Crystallography* **14**, 349-350 (1981).
[141] Pidol, L. *et al.* Scintillation properties of Lu 2 Si 2 O 7 :Ce 3+ , a fast and efficient scintillator crystal. *Journal of Physics: Condensed Matter* **15**, 2091 (2003).

[142] Fleet, M. E. & Liu, X. A new rare earth disilicate (REE2Si2O7; REE= Dy, Tm, Lu; type-L): Evidence for non-quenchable 10 GPa polymorph with silicon in fivefold trigonal bipyramidal coordination? *American Mineralogist* **89**, 396-404 (2004).

[143] Takahashi, J. *et al.* Crystal Structure of Lu4Si2O7N2 Analyzed by the Rietveld Method Using the Time-of-Flight Neutron Powder Diffraction Pattern. *Journal of the American Ceramic Society* **85**, 2072-2077 (2002).

[144] Hampshire, S. Silicon nitride ceramics–review of structure, processing and properties. *Journal of Achievements in Materials and Manufacturing Engineering* **24**, 43-50 (2007).

[145] Shibata, N. *et al.* Rare-earth adsorption at intergranular interfaces in silicon nitride ceramics: Subnanometer observations and theory. *Phys. Rev. B* **72**, 140101 (2005).

[146] Kitayama, M., Hirao, K., Toriyama, M. & Kanzaki, S. Modeling and simulation of grain growth in Si3N4. III. Tip shape evolution. *Acta Mater.* **48**, 4635-4640 (2000).

[147] Kitayama, M., Hirao, K., Toriyama, M. & Kanzaki, S. Modeling and simulation of grain growth in Si3N4—II. The α–β transformation. *Acta materialia* **46**, 6551-6557 (1998).

[148] Kitayama, M., Hirao, K., Toriyama, M. & Kanzaki, S. Experimental Evidence for the Anisotropic Ostwald Ripening of β-Silicon Nitride. *Journal of the American Ceramic Society* **82**, 2931-2933 (1999).

[149] Lee, D.-D., Kang, S.-J. L. & Yoon, D. N. Mechanism of Grain Growth and α-β′ Transformation During Liquid-Phase Sintering of β′-Sialon. *Journal of the American Ceramic Society* **71**, 803-806 (1988).

[150] Krämer, M., Wittmüss, D., Küppers, H., Hoffman, M. J. & Petzow, G. Relations between crystal structure and growth morphology of β-Si3N4. *Journal of Crystal Growth* **140**, 157-166 (1994).

[151] Becher, P. F. *et al.* Observations on the Influence of Secondary Me Oxide Additives (Me=Si, Al, Mg) on the Microstructural Evolution and Mechanical Behavior of Silicon Nitride Ceramics Containing RE2O3 (RE=La, Gd, Lu). *J. Am. Ceram. Soc.* **93**, 570-580 (2010).